NANOSTRUCTURED MIXED TRANSITION METAL SPINEL OXIDE AS EFFICIENT ELECTROCATALYSTS

SREENA R.THEKKOOT

A THESIS SUBMITTED TO THE FACULTY OF GRADUATE STUDIES IN PARTIAL FULFILLMENT OF THE REQUIREMENT FOR THE DEGREE OF MASTER OF SCIENCE

GRADUATE PROGRAM IN CHEMISTRY

YORK UNIVERSITY

TORONTO, ONTARIO

FEBRUARY 2015

Abstract

For my M.Sc. research, I have prepared $Cu_xCo_{3-x}O_4$ films with various compositions with x values ranging from 0 to 1, in order to optimize their electrocatalytic properties for the oxygen evolution reaction. The prepared materials were characterized by X-ray diffraction (XRD), scanning electron microscopy (SEM), energy dispersive spectroscopy (EDX), and cyclic voltammetry (CV).

Two methods have been chosen for the preparation of the $Cu_xCo_{3-x}O_4$ films, namely the thermal decomposition and co-precipitation methods.

The SEM analysis shows that the prepared electrodes were very porous and the EDX analysis proved that there is a good correlation between stoichiometric and EDX-derived copper to cobalt ratios. The formation of spinel structure was confirmed by XRD analysis. XRD analysis also allowed the lattice parameter of the material to be determined as a function of the composition. The increase of the lattice parameter with increase of Cu content, further supported the incorporation of Cu in the spinel structure. Cyclic voltammetric experiments were carried out on the electrodes prepared by thermal decomposition method. The $Cu_{0.75}Co_{2.25}O_4$ showed the lowest overpotential for the oxygen evolution reaction in 1M KOH electrolyte. Also the electrodes prepared by thermal decomposition method were found to be active for the electroreduction of hydrogen peroxide when a 3M NaOH solution containing 0.6M hydrogen peroxide solution was used. However, at a given potential Co_3O_4 has achieved higher current density compared to copper substituted cobalt spinel, hence Cu addition did not result in enhanced catalytic activity under these conditions.

Acknowledgements

First of all, I would like to express my deepest gratitude to the Almighty God, for his blessings on me and providing me the opportunity to pursue this program.

I am so grateful to my supervisor Dr. Sylvie Morin for her continuous motivation and guidance that made it possible to complete this project successfully. I sincerely appreciate her time and help.

I would like to thank my committee members Dr. William Pietro and Dr. Valeria Tsoukanova for their suggestions and insightful comments.

I greatly appreciate Dr. Srebri Petrov for performing X-ray diffraction measurements and data analysis and Karen Rethoret for providing assistance and training for SEM and EDX analysis. I would like to thank Dr. Morin's group member for their help and support.

I would like to dedicate this work and give special thanks to my parents, husband and beloved children.

Table of Contents

Abstract……..... *ii*

Acknowledgement…….……iii

Table of Contents…….…… iv

List of tables …….……...vii

List of figures …….. ix

List of Acronyms…….....xi

List of Symbols……..…….……..……xii

Chapter 1- Introduction…….……...1

1.1. Nanostructured $Cu_xCo_{3-x}O_4$ as Electrocatalysts……..…….……....1

1.2. Our research…….....3

1.3. Structure of the thesis……4

Chapter 2 - Theory and background……..…….5

2.1. Literature review……...5

2.2 Cobalt spinel structure and properties……....7

2.3. Scanning electron microscopy (SEM)……..9

2.3.1. Principle of Scanning electron microscopy……..9

2.3.2. Instrumentation……..……..10

2.4. Energy dispersive spectrometry (EDS)…….…..12

2.4.1. Principle of Energy dispersion spectrometry……...12

2.4.2. Instrumentation……....13

2.5. X-ray diffraction (XRD)……14

2.5.1. Principle of X-ray diffraction……..14

2.5.2. Instrumentation……16

2.6. Cyclic voltammetry…….....18

2.6.1. Principle of cyclic voltammetry…….....18

2.6.2.Roughness factor……..19

2.6.3. Instrumentation……20

Chapter 3 - Experimental Techniques……..…….22

3.1. Preparation of $Cu_xCo_{3-x}O_4$……22

3.1.1. Thermal decomposition method……..22

3.1.2. Co-precipitation method……..23

3.2. Characterization methods……23

Chapter 4 - Results and discussion…….25

4.1. Film morphology – scanning electron microscopy……25

4.2. Film composition - energy dispersion spectrometry…….……..36

4.3. Film structure - x-ray diffraction…….……...49

4.4. Surface Area characterization and Electrocatalytic behavior-cyclic voltammetry.....59

4.4.1. Roughness factor (R_F)…….....59

4.4.2. Oxygen evolution reaction at $Cu_xCo_{3-x}O_4$ electrodes……..69

4.4.3. Electroreduction of hydrogen peroxide……...76

Chapter 5 - Conclusions and Future work……..80

5.1. Conclusions……..80

5.2. Future work……..83

References……84

Appendix ……90

A.1. EDX Error Analysis…….90

A.2. Error in the concentration of the solution used for the preparation of $Cu_xCo_{3-x}O_4$ films……..95

A.3. X-ray diffraction error analysis……100

A.4. Roughness factor - error calculation…….101

A.5. Calibration of potentiostat……102

References…….105

List of Tables

Table 4.1: Stoichiometric and EDX Copper – cobalt ratio of the $Cu_xCo_{3-x}O_4$ electrode prepared by co-precipitation and thermal decomposition methods…….....48

Table 4.2: Stoichiometric and EDX copper – cobalt ratio of the $Cu_xCo_{3-x}O_4$ electrodes prepared by thermal decomposition method…….48

Table 4.3: The lattice parameter of $Cu_xCo_{3-x}O_4$ electrode prepared by thermal decomposition method……..……...56

Table 4.4: Percent of CuO detected in the $Cu_xCo_{3-x}O_4$ electrode prepared by co- precipitation and thermal decomposition methods...…….....…….58

Table 4.5: Roughness factor of $Cu_xCo_{3-x}O_4$ prepared by thermal decomposition method……..……..68

Table 4.6: The redox potential of $Cu_xCo_{3-x}O_4$ prepared by thermal decomposition method……..……..73

Table 4.7: The onset potential and overpotential of $Cu_xCo_{3-x}O_4$ electrodes prepared by thermal decomposition method.……..……75

Table 4.8: The onset potential and the maximum current density obtained during the electroreduction of $Cu_xCo_{3-x}O_4$…….78

Table A1: The EDX measurement at different spots of a $CuCo_2O_4$ electrode prepared by thermal decomposition method……...92

Table A2: The EDX measurement at different spots of a $Cu_{0.5}Co_{2.5}O_4$ electrode prepared by co-precipitation method……..94

Table A3: The error associated with stock solutions used for the co-precipitation method……..95

Table A4: The error associated with the final solution used for co-precipitation method……..96

Table A5: The error associated with stock solution, used for Thermal decomposition method…….97

Table A6: The error associated with the final solution used for thermal decomposition method…….99

Table A7: The error in the percentage of CuO present in the samples, prepared by co-precipitation method and thermal decomposition method…….100

Table A8**:** Resistance and capacitance values measured by the potentiostat compared to the theoretical values given for the electric circuit. ……..103

List of figures

Fig. 2.1: Schematic diagram of spinel crystal structure……..…….8

Fig. 2.2: Schematic drawing of the structure of scanning electron microscope (SEM).....11

Fig. 2.3: Scanning electron microscope (SEM = FEI, QUANTA 3D PEG)…….…11

Fig. 2.4: X-ray emission spectrum.……..……...……..13

Fig. 2.5: Schematic representation of energy dispersive spectroscopy…….……....14

Fig. 2.6: Bragg reflection from a set of crystal plane……..……..16

Fig. 2.7: Geometric arrangement of X-ray diffractometer….....……...17

Fig. 2.8: Bruker AXS D2 Phaser diffractometer……..…….17

Fig. 2.9: A typical cyclic voltammogram…….....……..21

Fig. 4.1: SEM micrographs of $Cu_xCo_{3-x}O_4$ prepared by co-precipitation method……...26-30

Fig. 4.2: SEM micrographs of Cu-Co oxide prepared by thermal decomposition method…..31-36

Fig. 4.3: EDX spectra of $Cu_xCo_{3-x}O_4$ prepared by co-precipitation method……...38-42

Fig. 4.4: EDX spectra of $Cu_xCo_{3-x}O_4$ prepared by thermal decomposition method……....43-47

Fig. 4.5: XRD patterns of a) Co_3O_4 b) $Cu_{0.5}Co_{2.5}O_4$ prepared by Co-precipitation method…51-52

Fig. 4.6: XRD patterns of $Cu_xCo_{3-x}O_4$ prepared by thermal decomposition method……..53-55

Fig. 4.7: Graphical representation of $(Cu/Co)_{EDX}$ ratio in $Cu_xCo_{3-x}O_4$ as a function of lattice parameter……57

Fig. 4.8: Cyclic voltammograms in the potential region -0.10mV to 10mV (SCE) in 1M KOH (a). Co_3O_4, (b) $Cu_{0.25}Co_{2.75}O_4$, (c) $Cu_{0.5}Co_{2.5}O_4$, (d) $Cu_{0.75}Co_{2.25}O_4$, (e) $CuCo_2O_4$……..…...60-62

Fig. 4.9: Plot of double layer charging current density vs. scan rate (a). Co_3O_4, (b) $Cu_{0.25}Co_{2.75}O_4$, (c) $Cu_{0.5}Co_{2.5}O_4$, (d) $Cu_{0.75}Co_{2.25}O_4$, (e) $CuCo_2O_4$……63-67

Fig.4.10: Cyclic voltammograms of $Cu_xCo_{3-x}O_4$ (SCE) (a) Co_3O_4, (b) $Cu_{0.25}Co_{2.75}O_4$, (c) $Cu_{0.5}Co_{2.5}O_4$, (d) $Cu_{0.75}Co_{2.25}O_4$, (e) $CuCo_2O_4$ thin films in 1M KOH at a scan rate of 50mVs^{-1} prepared by thermal decomposition method……..…..71-73

Fig. 4.11: Cyclic voltammograms of $Cu_xCo_{3-x}O_4$ per unit real surface area of electrode surface……..……..76

Fig. 4.12: a) Cyclic voltammogram of electroreduction of H_2O_2 using $Cu_xCo_{3-x}O_4$ films prepared by thermal decomposition method b) cyclic voltammogram of $Cu_{0.75}Co_{2.25}O_4$……...……78-79

Figure A1: Reference circuit box used to calibrate the potentiostat……....103

Figure A2: Nyquist plots of reference circuit with (a) one capacitor and (b) two capacitors…..104

List of Acronyms

OER	Oxygen evolution reaction
SEM	Scanning electron microscopy
EDX	Energy dispersive X-ray spectroscopy
XRD	X-ray diffraction
CV	Cyclic voltammetry
DSA	Dimensionally stable anode
FTO	Fluorine doped tin oxide
SCE	Saturated calomel electrode
pzc	Potential of zero charge

List of Symbols

d_{hkl}	Spacing between the atomic planes
λ	Wavelength
j_{cap}	Capacitive charging current density
A_g	Geometrical surface area
A	Real surface area
Q	Electrical charge
E	Electrode potential
V	Scan rate
R_F	Roughness factor
E_p^c	Peak cathodic potential
Ep^a	Peak anodic potential
Ip^c	Peak cathodic current
I_p^a	Peak anodic current

Chapter 1 – Introduction

1.1. Nanostructured $Cu_xCo_{3-x}O_4$ as Electrocatalyst

With the constant increase in energy demand in our modern world, greater, cleaner and more reliable energy sources are needed. Today, most of our needs are met by the consumption of fossil fuel such as coal, natural gas and petroleum. The overuse of natural resources such as petroleum and coal has caused significant adverse environmental effects. The depletion of fossil fuels and its adverse effect on the environment stimulates the search for renewable sources of energy. However, nonconventional energy sources like solar, wind, waves, geothermal and thermonuclear energy cannot contribute significantly to the world's current energy needs in their current form, due to factors such as cost, state-of-the-art and availability. Thus, the current energy crisis presents major challenges and alternative sources of energy should be sought to ensure sustainable development while reducing our energy consumption.

Electrochemical technology is cleaner and can offer environmental protection through nonpolluting energy sources. Oxygen evolution reaction (OER) has great importance in electrosynthesis, electrowinning, energy conversion and energy storage devices.

$$O_2 + 2H_2O + 4\,e^- \rightleftharpoons 4OH^- \qquad (1.1)\ [1]$$

However OER is highly irreversible in aqueous electrolytes and causes substantial energy loss in the electrochemical cell. While hydrogen is viewed by many as the energy carrier of the future and can be produced by water electrolysis; producing hydrogen from water remains expensive and inefficient using non-platinum group metals. This is related to the high

overpotential associated with electrolytic evolution of oxygen at the anode [2, 3]. Therefore, it is necessary to minimize the anodic overpotential of the oxygen evolution reaction.

Electrocatalysis involves optimization of electrode processes by choosing appropriate electrode materials. The main requirements of the electrode material for OER are high surface area, high electric conductivity, good electrocatalytic properties, and minimization of gas bubble adhesion and low costs. Among these, the electrocatalytic behavior is the most important property, which directly influences the overpotential of the oxygen evolution reaction and hence the energy cost of the overall process. It has been demonstrated that nanostructured materials with high surface to volume ratio enhance the electron transfer properties at a lower overpotential [4 - 7].

Transition metal oxides, which can exist in various valency states, exhibit good catalytic activity, making them a versatile material for chemical and electrochemical reactions. Moreover, they possess good stability and have been extensively investigated as electrocatalysts to decrease the overpotential of the oxygen evolution reaction [8].

Among transition metal oxides, spinel oxides form an interesting class of compounds due to their remarkable optical, electrical, magnetic and catalytic properties [9 – 11]. Among spinel type oxides, cobalt spinels have received great attention due to their high catalytic activity, larger availability, lower cost and their good corrosion stability [12, 13].

Spinel oxides of the type $M_xCo_{3-x}O_4$ (where M= Ni, Cu, Mn, Zn) possess enhanced electrocatalytic activity and stability. These compounds exhibit relatively high conductivity due to electron transfer between the cations, with low activation energy due to hopping mechanism. Copper substitution was found to possess high stability, good electrochemical property, lower cost, and better availability compared to other substitution cations [13 – 16].

In recent years, hydrogen peroxide emerged as an efficient oxidant for liquid-based fuel cells [17 - 19]. Hydrogen peroxide is a good candidate for applications such as underwater and space power generation where oxygen is not readily available.

In alkaline medium, at higher pH,

$HO_2^- + H_2O + 2e^- \rightarrow 3OH^-$ (1.2)[20]

The two-electron reduction reaction of H_2O_2 requires less activation energy compared to the four-electron oxygen reduction reaction. Since the hydrogen peroxide is in liquid form, its storage, handling as well as its feeding into the fuel cell is more convenient than gas phase oxidants [21]. Noble catalysts like platinum, palladium, silver, gold or combination of these metals show an excellent activity towards electroreduction of H_2O_2, but they are very expensive [22 – 25]. Cobalt oxide spinel has proved to exhibit considerable activity and stability for H_2O_2 electroreduction [26, 27].

1.2. Our research

In order to design a suitable material for various applications, it is necessary to understand the relationship between morphology, structure, composition and electron transfer properties. In this research we have prepared various compositions of copper-cobalt oxide (Co_3O_4, $Cu_{0.25}Co_{2.75}O_4$, $Cu_{0.5}Co_{2.5}O_4$, $Cu_{0.75}Co_{2.25}O_4$, and $CuCo_2O_4$) and their electrocatalytic properties are correlated to their composition, structure and morphology. Two methods of preparation have been chosen for the preparation of the electrodes: co-precipitation and thermal decomposition methods.

The surface morphology of the films was examined with scanning electron microscopy (SEM) and composition of the prepared films was analyzed by energy dispersive X-ray

spectroscopy (EDX). X-ray diffraction patterns were recorded to determine the film structure. The catalytic activity of the prepared electrodes towards oxygen evolution and hydrogen peroxide electroreduction reactions was studied by cyclic voltammetry.

1.3. Structure of thesis

This thesis is presented in five chapters: chapter 1 gives a brief introduction of $Cu_xCo_{3-x}O_4$ electrocatalysts and aim of this research; chapter 2 deals with previous work on eletrocatalysis for oxygen evolution reaction, fundamental principles and instrumentation of techniques used in this work for the characterization of material, namely - scanning electron microscopy (SEM), energy dispersive spectroscopy (EDX), X-ray diffraction (XRD) and cyclic voltammetry (CV). Chapter 3 outlines the experimental part of this research. It explains the preparation methods of our electrocatalysts and techniques used for the characterization of the prepared materials. Chapter 4 presents the experimental results and discussions based on material's characterization and electrocatalytic activity measurements. Chapter 5 summarizes the conclusions of this thesis and proposes future work.

Chapter 2: Theory and background

2.1. Literature review

Electrolytic water splitting has received great attention due to its wide range of applications in industry, such as energy conversion and energy storage devices. The overpotential of OER at the anode is a major factor limiting efficiency of water electrolysis. A great deal of effort has been devoted to design appropriate electrode material for achieving the lowest possible overpotential. For example, RuO_2 electrode- one of the most active catalyst for OER, achieved an overpotential of 0.25V in alkaline medium [28].

Numerous electrocatalysts have been proposed to decrease the anodic overpotential of the oxygen evolution reaction. The preservation of shape and structural integrity of the electrode has great importance with respect to technological and economic considerations. In 1967, Beer succeeded in preparing stable and electroactive oxides of platinum group metals like platinum, rhodium, iridium, ruthenium and palladium with titanium oxide or with oxides of other valve metals such as tantalum, zirconium and niobium. These dimensionally stable anodes were registered under the trademark of DSA. The discovery of dimensionally stable anodes (DSA) revolutionized the chlorine industry. The graphite anodes were replaced by dimensionally stable anodes and resulted in increased cell output and decreased power consumption. Later, these electrodes were found to possess activity for the oxygen evolution reaction [29, 30].

Many transition metal oxides have been investigated as DSA type electrodes. Among these, dioxides (eg. IrO_2, RuO_2/TiO_2) [31, 32], spinel (eg. $M_xCo_{3-x}O_4$ where M = Cu, Ni or Mn) [33], perovskites (eg. $La_{1-x}Ca_xCoO_3$, $La_{1-x}Sr_xFeO_{3-y}$) [34, 35], and pyrochlores (eg. $Pb_2Ru_2O_{6.5}$) [36]

have been successfully applied as anode coatings in a number of electrolytic processes such as oxygen and chlorine evolution reactions.

Trasatti *et al*. reviewed the work carried out on the various transition metal oxides for oxygen evolution reaction and emphasized that RuO_2 and IrO_2 are most active, but fairly expensive, catalyst in acid and alkaline media [14, 6].

Due to the cost considerations, replacement of precious noble metals is necessary. Spinel type cobalt oxides (Co_3O_4) have emerged as cheaper alternatives to DSA electrodes in alkaline media and have shown interesting electrocatalytic activity and stability towards OER [14, 37]. The catalytic activity of cobalt oxide can be increased by partial substitution of cobalt ions by other 3d-transition metals. A review of cobalt-based spinel oxides has been given by M. Hamdani *et al.* [11]. Among the spinel cobaltites of the type MCo_2O_4 (M = Cu, Mn, Ni, Zn, etc.), copper-substituted cobaltites have the advantage of high stability and catalytic activity with low cost and large availability [13, 14].

Singh and Singh reported an improved catalytic activity of cobaltites with introduction of Cu and Ni. The copper-substituted cobaltites were found to possess higher activity [38]. Marsan *et al.* also observed enhanced catalytic activity with the introduction of copper into the cobalt oxide lattice [39]. Similar results were obtained by Nikolov *et al.* [15]. Angelov *et al.* and Li *et al.* studied the effect of copper content in the surface structure and the composition of $Cu_xCo_{3-x}O_4$ [40, 41] and they found that copper to cobalt ratio at the surface is higher than that of the bulk.

The preparation method of oxide influences the physicochemical and electrochemical properties. Several methods have been used to prepare spinel cobaltites. These include: thermal decomposition [16, 39], sol gel [33, 42, 43], spray pyrolysis [44 - 46], precipitation [38, 47], gel

hydrothermal oxidation [48] and electrodeposition [49] methods. Of course, the specific parameters used with each of these methods will greatly affect the morphology, final composition, structure and stability of the films; hence the importance of controlling the film preparation parameters carefully.

In order to study the effect of substitution cations in cobalt oxides, R.N.Singh *et al.* prepared $M_xCo_{3-x}O_4$ (where M = Cu, Ni, Mn) by the co-precipitation method [38]. Copper substituted cobalt oxide ($Cu_{0.5}Co_{2.5}O_4$) was found to possess the highest catalytic activity compared to other substitution cations. Whereas $M_xCo_{3-x}O_4$ (where M = Cu, Ni) prepared by the sol gel method indicated that nickel substituted ($NiCo_2O_4$) cobaltites exhibited a higher catalytic activity compared to other cobaltites [50]. This is an indication of the effect of the preparation method on the properties of the electrode materials.

2.2. Cobalt spinel structure and properties

The chemical formula of spinel compounds can be expressed as AB_2O_4, where A represents a divalent cation (A^{2+}), which occupies one-eighth of tetrahedral holes, where as the trivalent cation (B^{3+}) occupies one half of the octahedral holes in a cubic close packed array of oxide anions. The unit cell of the spinel is shown in Fig 2.1 and consists of eight formula units, in which there are 32 octahedral and 64 tetrahedral interstices. The inverse spinel structure is represented as $B(AB)O_4$, where half of the B cations are in the tetrahedral site and the other half occupy octahedral site along with A [14, 51, 52].

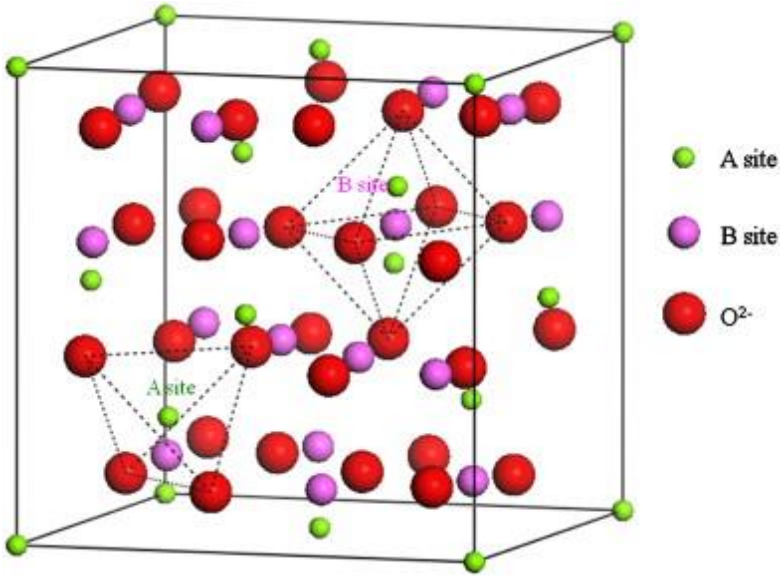

Fig. 2.1: Schematic diagram of spinel crystal structure (adapted from reference 53).

Cobalt oxide spinels (Co_3O_4) adopt normal cubic spinel structure and can be represented as $Co^{2+}(Co^{3+})_2O_4$. Some of the Co^{2+} sites in the spinel can be substituted by foreign divalent metal ions, producing a binary spinel oxides of the type $M_xCo_{3-x}O_4$ (where M= Ni, Cu, Mn, Zn) with enhanced electrocatalytic activity. These compounds possess a relatively higher conductivity. The conductivity in these materials is achieved by movement of carriers along octahedral sites. Spinels are always associated with excess oxygen atom, hence a part of M^{3+} atoms are converted to M^{4+} with the formation of conductivity chain.

$$M^{4+} \rightleftharpoons M^{3+} + \text{hole} \qquad (2.1)$$

Thus substitution of octahedral site is expected to increase the conductivity of the material [14, 54].

Spinels of the type $Cu_xCo_{3-x}O_4$ are one the most active oxide [4, 11, 14, 38]. When the amount of copper content x > 0.2 in $Cu_xCo_{3-x}O_4$, a transition from normal spinel to inverse spinel occurs and can be represented as

$$Co^{2+}_{1-x}Cu^{2+}_{x-y}Co^{3+}_{y}(Co^{3+}_{2-y}Cu^{2+}_{y})O_4$$

where x is the relative copper content in the spinel and y is copper content occupied in the octahedral sites of the spinel .The ionic radii of Co^{2+} are 58pm in tetrahedral and 52.5pm in octahedral sites, whereas the ionic radii of Cu^{2+} are 57pm in tetrahedral site and 73pm in octahedral site. The difference in the radius at two sites is 5.5pm for cobalt and 16pm for copper. So an increase in the lattice parameter is expected with addition of copper [47, 55]. In spinel oxides, the mixed valences of cations contribute to the reversible adsorption of oxygen by providing donor acceptor sites for chemisorption [4].

2.3. Scanning electron microscope (SEM)

Scanning electron microscopy is a powerful technique in the analysis of organic and inorganic materials. It provides topographic and morphological information, which is necessary to understand the behavior of surfaces.

2.3.1. The principle of scanning electron microscopy

In scanning electron microscopy, the electron beam interacts with specimen and the signals produced contain information about the composition and morphology of the sample. The electron beam is focused into a small probe and rastered across the surface of a specimen. Due to the large depth of the field, it provides a three dimensional appearance to the images [56].

2.3.2. Instrumentation

A schematic of a scanning electron microscope is shown in the Fig. 2.2. The electron beam is emitted from an electron gun. The two condenser lenses decrease the crossover diameter of the electron beam .The objective lens focuses the electron beam as a probe and the deflection system cause the beam to move over the specimen and a rectangular raster is generated. The magnification is determined by the ratio of the raster on the viewing screen to the corresponding length of the raster on the specimen being scanned.

As the high-energy beam interacts with the specimen, they produce elastic or inelastic scattering. Elastic scattering results from the scattering of the incident electrons by atoms in the specimen and deflected from the specimen at a large angle. These electrons are called backscattered electrons and are useful for the formation of compositional contrast. Inelastic scattering produces secondary electrons, which deflect at a small angle and are responsible for topographic contrast. These electrons are detected by an Everhart-Thornley detector, amplified and then displayed on a screen [56, 57]. Fig 2.3 shows the photograph of scanning electron microscope used in this work.

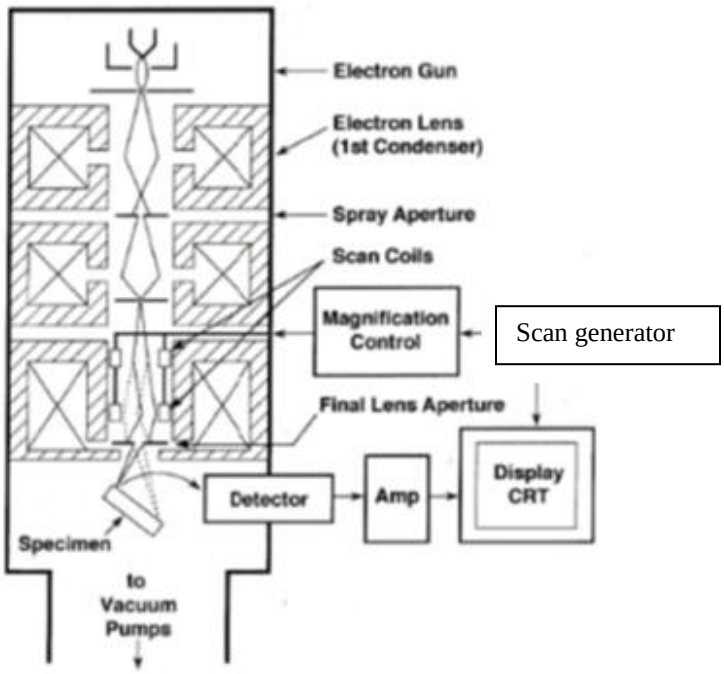

Fig. 2.2: Schematic drawing of the structure of scanning electron microscope (adapted from reference 56).

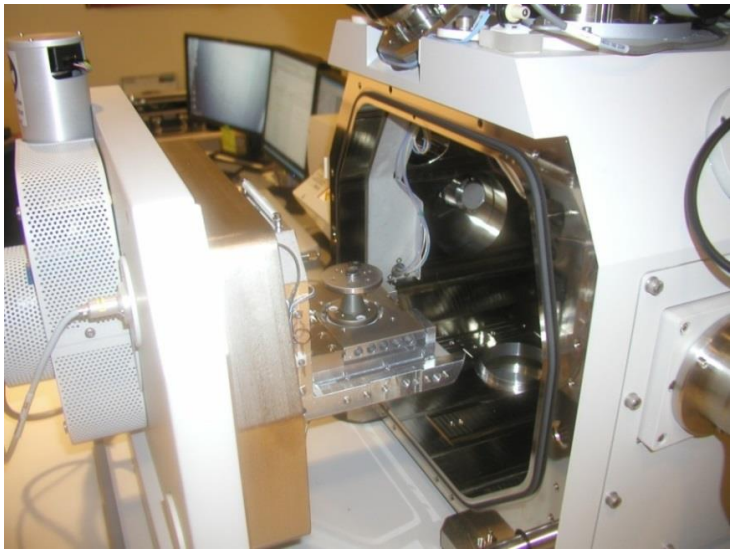

Fig. 2.3: Picture of the loading chamber of the scanning electron microscope (SEM = FEI, QUANTA 3D PEG) used in this work.

2.4. Energy dispersive X-ray spectroscopy (EDX)

Energy dispersive X-ray spectroscopy is a powerful analytical technique used for elemental analysis. EDX systems are commonly a part of the scanning electron microscope or transmission electron microscope. It uses a primary electron beam to generate characteristic X-rays from the sample.

2.4.1. Principle of Energy dispersive X-ray spectroscopy (EDX)

EDX relies on the principle that each element has a unique atomic structure and produces a characteristic X-ray spectrum. When a high energy radiation strikes a specimen, it generates X-ray radiation with a range of wavelength called continuous X-rays or white X-rays, with a sharp intensity maxima at certain wavelengths, superimposed on the continuous spectrum as shown in the Fig. 2.4. These intensity maxima are characteristic of the specimen. The energy of the radiation is high enough to knock out an electron from the inner shell, and the inner electron vacancy is filled by an outer shell electron and a characteristic X-ray is generated. The energy of the emitted radiation is equal to the difference in the amount of the energy of the two shells, which is the characteristic of the particular atom [56, 57]. The high energy of electrons allows them to escape the sample from a depth of about 300 nm.

The atom consists of a nucleus, at the centre, and the electrons lying in various shells like K, L, M etc., surrounding the nucleus. The designation of shells as K, L, M... corresponds to the principal quantum numbers n = 1, 2, 3…, respectively. The vacancy created in the shell can be filled in by an electron from any of the outer shells and a characteristic radiation is emitted. For example, a vacancy in the K shell can be filled in by an electron from an L shell or M shell, and the emitted X-ray can be assigned as Kα and Kβ X-rays, respectively. The intensity of Kα X-

rays are higher than the Kβ, as the probability of filling the K shell by an electron from the L shell is much higher than the possibility of filling it by an electron from the M-shell [58].

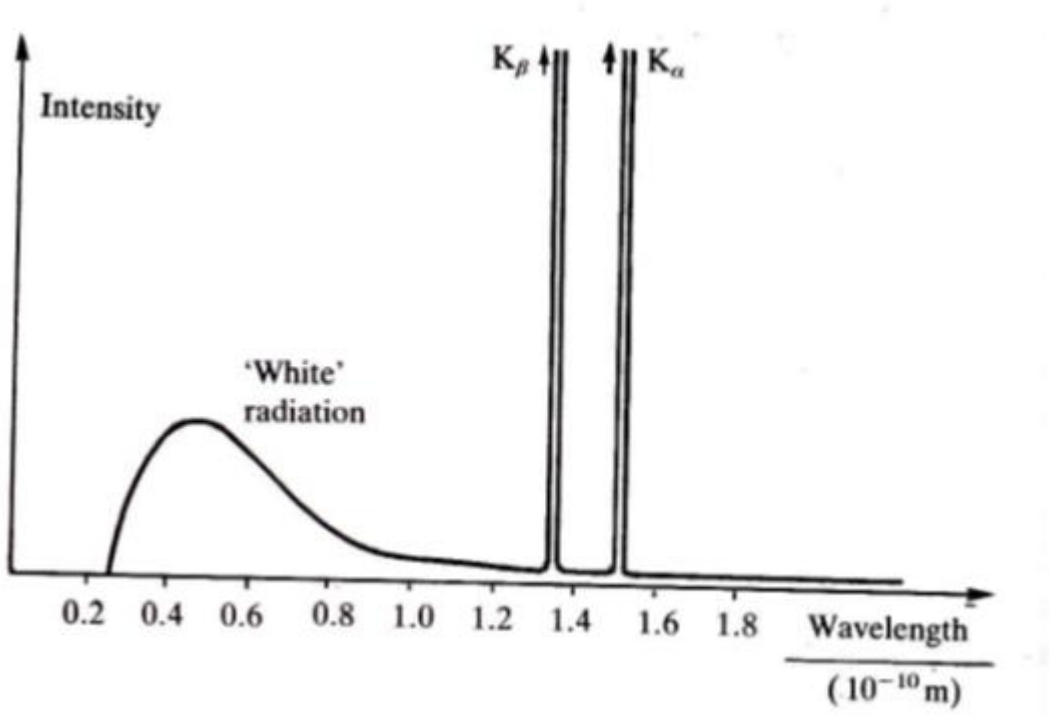

Fig. 2.4: X-ray emission spectrum (adapted from reference 51).

2.4.2. Instrumentation

In an EDX system, the electron beam interacts with an inner electron of the specimen ejecting an electron of the shell. The X-ray photons from the sample are collected by the detector and produce electron–hole pairs. The Si (Li) is the most commonly used detector in EDX system. The preamplifier converts these electron-hole pairs into a voltage pulse and the signal is further amplified by a linear amplifier. The amplified signal reaches a computer X- ray

analyzer and it is represented as a histogram of intensity as a function of voltage [56]. A schematic representation of the energy dispersive spectroscope is shown in the Fig. 2.5.

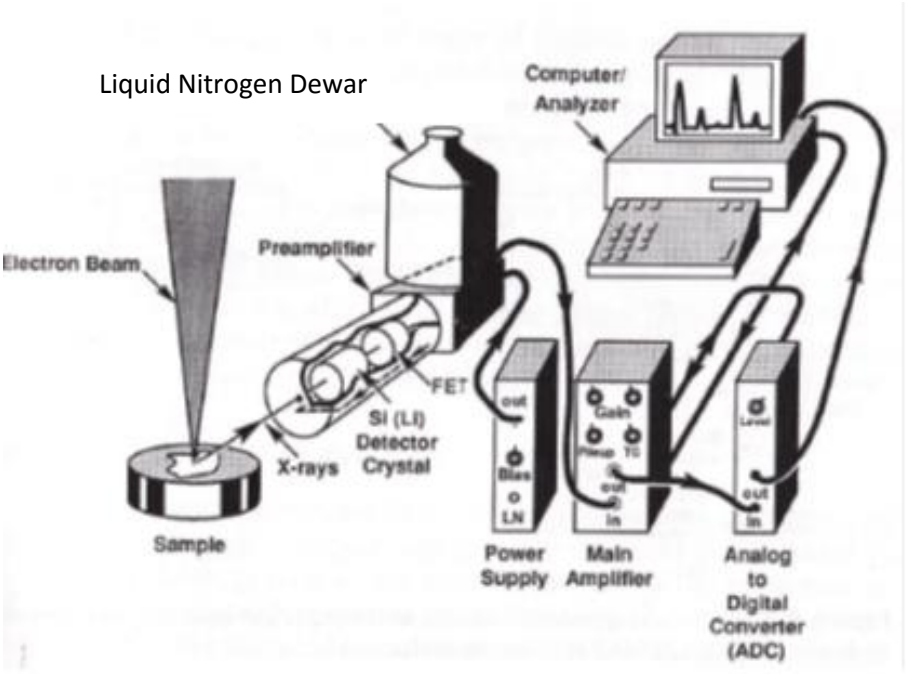

Fig. 2.5: Schematic representation of energy dispersive spectroscope (adapted from reference 56).

2.5. X-ray diffraction (XRD)

X-ray diffraction was discovered by Von Laue in 1912 and since then, this technique has been widely used for material characterization. X-ray diffraction is an effective method for elucidating the crystal structure of materials. It has great importance in science and industry.

2.5.1. Principle of X-ray diffraction

Crystalline materials possess a regular arrangement of atoms, ions or molecules with interatomic distance of the order of 100 pm. Since the spacing between planes is of the same

order as that of the wavelength of the X-rays, they produce diffraction patterns. The X-ray beams diffracted from the crystal plane interfere constructively when the path length difference between the two diffracted beams is equal to an integral number of wavelengths. From Fig 2.6, it follows that the path difference between the two reflected rays (EF+FG) is equal $2d_{hkl}\sin\theta$.

According to the Bragg's condition,

$$2d_{hkl}\sin\theta = n\lambda \quad (2.2)$$

where λ is the wavelength of the incident wave and n is an integer. The spacing between the atomic planes (d_{hkl}) of a crystal can be calculated by knowing the incident angle at which constructive interference occurs and the wavelength (λ) of the incident beam. For a cubic crystal, the lattice parameter (a_0) is calculated from the plane spacing (d_{hkl}) using the following relation:

$$a_0 = d\,(h^2 + k^2 + l^2)^{1/2} \quad (2.3)$$

where h, k and l are Miller indices, representing a series of parallel planes in a crystal with a spacing of d_{hkl} [51, 58].

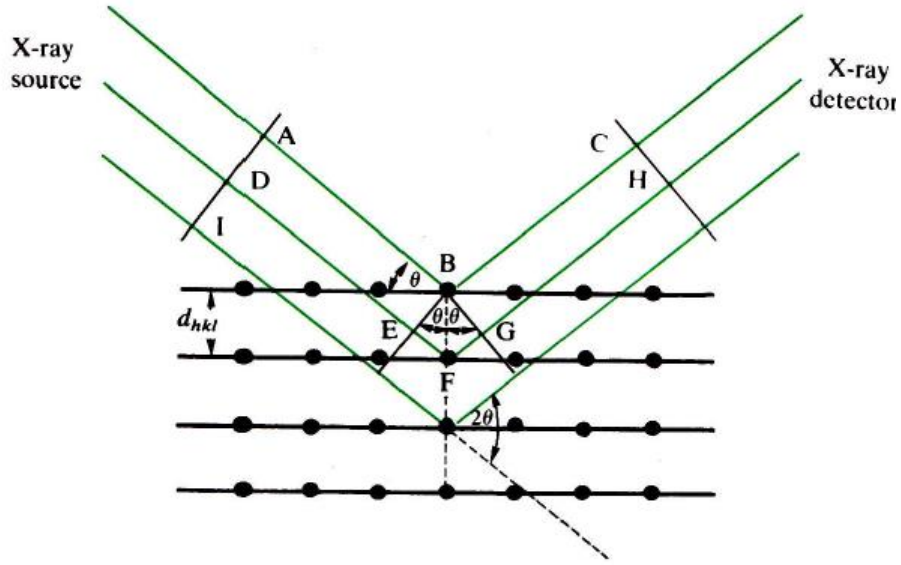

Fig. 2.6: Bragg reflection from a set of crystal planes (adapted from reference 51).

2.5.2. Instrumentation

In a diffractometer, the intensity of a diffracted beam is measured as a function of diffraction angle (2θ). The diffractometer consists of an x-ray source, sample and detector. Geometric arrangement of the X-ray diffractometer is shown in the Fig. 2.7. X-rays, produced from the X-ray tube, are diffracted from the sample and form a convergent diffracted beam. The special slits in the diffractometer (Soller slits are the most commonly used) collimate the incident and diffracted beams. The diffracted beams pass through the monochromatic filter before reaching the detector in order to suppress the wavelengths, except for the Kα radiation and to decrease the background radiation originating in the specimen. The intensity of the diffracted beam is measured directly by the detector in a range of 2θ [57, 58]. XRD patterns were collected on the Bruker AXS D2 Phaser diffractometer, is shown in the Fig. 2.8.

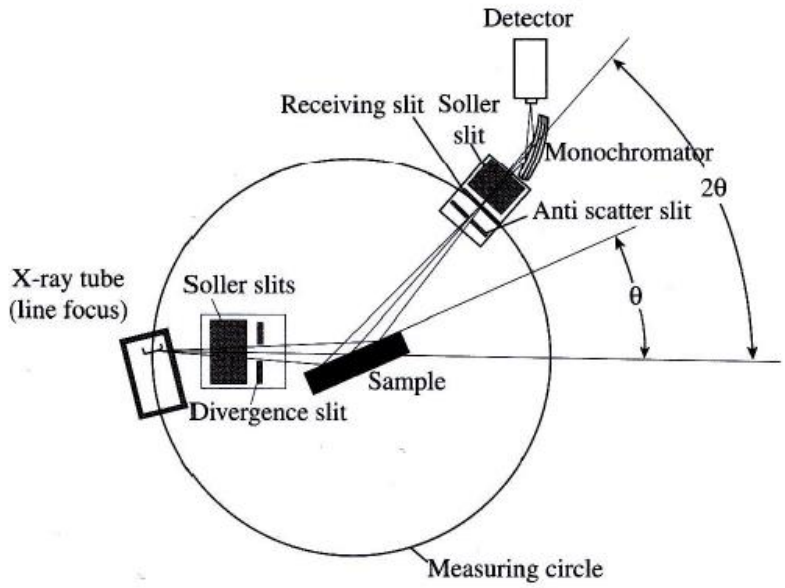

Fig. 2.7: Geometric arrangement of X-ray diffractometer (adapted from reference 57).

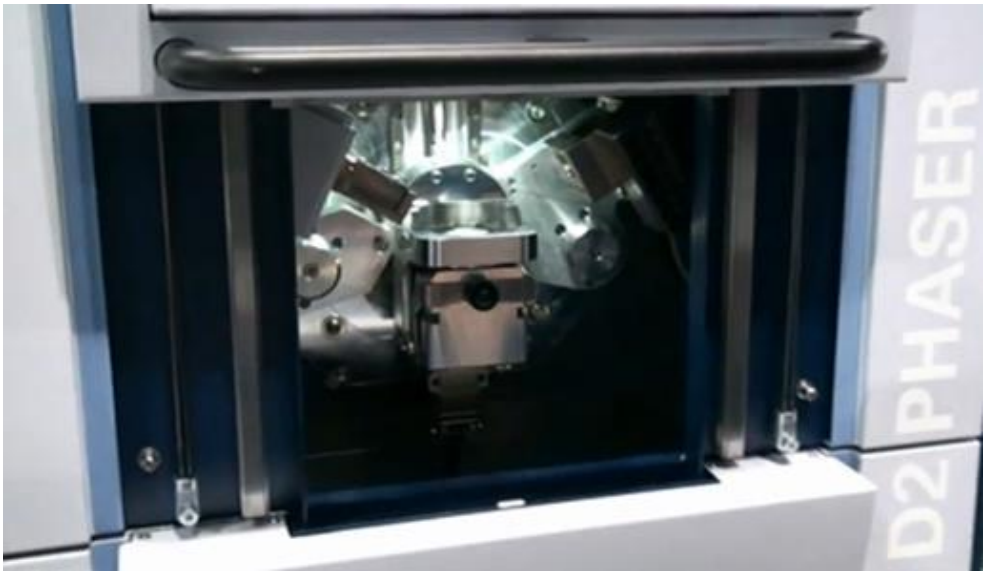

Fig. 2.8: Picture of the Bruker AXS D2 Phaser diffractometer used in this work.

2.6. Cyclic Voltammetry

Cyclic voltammetry has become a popular technique in obtaining information about complicated electrode reactions. Cyclic voltammograms are graphical representations of the current as a function of potential difference between reference and working electrodes. When the electroactive species is present, the current will be recorded, as the applied potential becomes sufficiently negative or positive.

2.6.1. Principle of Cyclic voltammetry

The analyte of interest needs to be redox active within the experimental window. The potential is swept in a linear manner to the set potential and then reversed. The oxidation or reduction of the material at or near the working electrode results in the generation of the current. During the anodic sweep, the applied potential increases and the current has a positive sign, while during the cathodic sweep the applied potential decreases and the current has a negative sign. The analysis of the current response can give information about electron transfer mechanisms at the electrode solution interface.

The reversible equilibrium reaction at the electrode can be represented as

$$\text{Oxidant} + ne^{-1} \rightleftharpoons \text{Reductant} \qquad (2.4)$$

The current associated with the transfer of electrons by an oxidation or reduction process is known as faradaic current. At the interface between electrode and electrolyte, there exists a segregation of positive and negative charges. Due to the presence of oppositely charged supporting electrolyte, adjacent to the electrode, a capacitive charging current (j_{cap}) is generated as the potential changes. This capacitive charging current is proportional to the scan rate.

$$j_{cap}/A = (dQ/dt)1/A = C_{dl}(dE/dt) = C_{dl}v \quad (2.5)$$

where C_{dl} is the capacitance of the double layer per unit area, Q is the charge, E is the potential, t is the time, A is the area of the working electrode and v is the scan rate [59, 60].

2.6.2. Roughness factor (R_F)

The roughness factor can be defined as the real surface area per unit geometric area.

$$R_F = A/A_g \quad (2.6)$$

where R_F represents roughness factor, A the real surface area and A_g the geometric surface area [59, 61]. This parameter is very important when dealing with high surface area materials, such as porous or nanostructured electrodes.

Cyclic voltammetry can be used to determine the roughness factor of electrodes. Cyclic voltammograms are recorded in a narrow potential region, where such capacitive current is measured at different sweep rates. The charging current density in the middle of the potential region is plotted as a function of scan rate and from the slope of the linear plot, the double layer capacitance is calculated [38, 39].

$$C_{dl} = di_{cap}/d(\partial E/\partial t) \quad (2.7)$$

where C_{dl} is the double layer capacitance, $\partial E/dt$ is the scan rate and i_{cap} is the current density. The double layer capacitance of a smooth surface is assumed to be $60\mu Fcm^{-2}$. The double layer capacitance of iodide at Hg and AgI solution interface has been established as $30\mu Fcm^{-2}$. Devnathan *et al.* have measured the double layer capacitance on mercury using electrocapillary` measurements for mercury in potassium iodide solution. The differential capacitance of oxide-aqueous solution interface at the near point of zero charge (pzc) is close to that of Hg and AgI

solution interface. Capacities on positively and negatively-charged oxide surfaces are more symmetrical for oxide-aqueous solution, whereas higher capacity is observed for Hg and AgI solution interface at positive side.

The roughness factor for a sample of unknown roughness is calculated from the ratio of C_{dl} of the sample and C_{dl} of a smooth oxide surface [61 – 63].

2.6.3. Instrumentation

The basic components for a cyclic voltammetry experiment are the potentiostat, the computer and the electrochemical cell. The electrochemical cell usually consists of an electrolyte (salt and solvent), and one or more electroactive species. A three-electrode system is used for the all of our electrochemical experiments: working electrode, reference electrode, and counter electrode (auxiliary electrode). The potentiostat measures the potential difference between the working electrode and reference electrode and applies current through the counter electrode. The reaction of interest takes place at the working electrode.

The reference electrode provides a stable potential and the potential of the working electrode is measured against the reference electrode. The most commonly used reference electrodes in aqueous medium is the silver/silver chloride (Ag/AgCl) electrode. The half-cell reactions can be written as:

$$AgCl_{(solid)} + e^{-1} \rightleftharpoons Ag_{(solid)} + Cl^{-1}{}_{(solution)} \qquad (2.8)$$

Another commonly used electrode in aqueous solution is the calomel reference electrode and the corresponding half-cell reaction is represented as [59, 60]:

$$1/2Hg_2Cl_{2(solid)} + e^{-1} \rightleftharpoons Hg_{(liquid)} + Cl^{-1}{}_{(solution)} \quad (2.9)$$

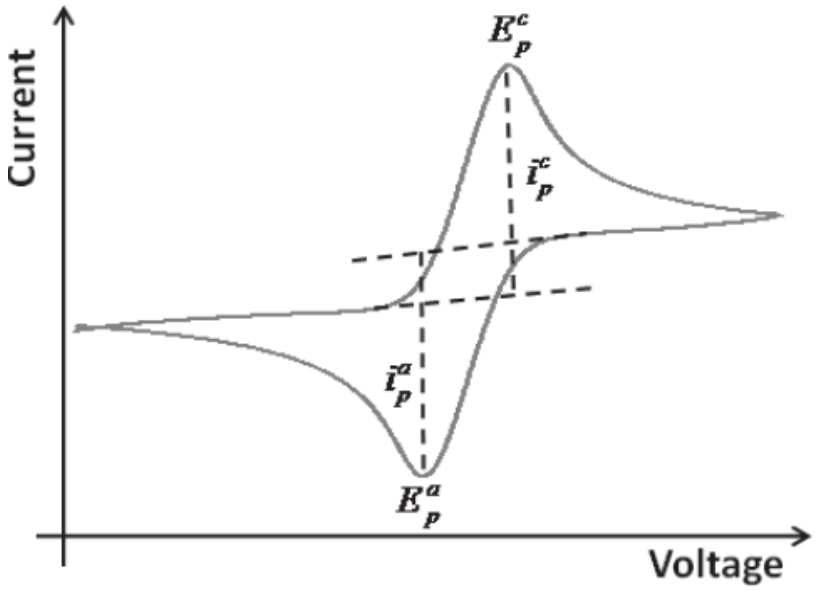

Fig.2.9. A typical cyclic voltammogram for redox species in solution (E_p^c = peak cathodic potential, E_p^a = peak anodic potential, I_p^c= peak cathodic current and I_p^a= peak anodic current) (adapted from reference 64).

Chapter 3: Experimental Techniques

3.1. Preparation of $Cu_xCo_{3-x}O_4$

The preparation method influences particle size, shape and surface chemistry of the materials [65]. In this work, thermal decomposition of mixed nitrate precursors and co-precipitation of metal sulfate are adopted for the preparation of copper-cobalt oxide spinel ($Cu_xCo_{3-x}O_4$) with x values ranging from 0 to 1.

3.1.1. Thermal decomposition method

The thermal decomposition method is a successful method for the preparation of $Cu_xCo_{3-x}O_4$ with high x values (x > 0.7) [16, 36, 44]. The salt precursor was prepared by dissolving Co $(NO_3)_2.6H_2O$ (A.C.S Sigma Aldrich ≥ 98%) and Cu $(NO_3)_2$. $3H_2O$ (Sigma Aldrich 99.0% - 100.5%) in a solvent mixture of isopropanol: ultrapure water in (4:1) ratio. These nitrate salt solutions, mixed in an appropriate molar ratio (x = 0, 0.25, 0.5, 0.75, 1) with 9 drops of Triton X-100 and directly deposited on a fluorine doped tin oxide coated transparent conductive glass (FTO coated glass). The solvent was evaporated by heating at 60ºC and subsequently calcined at 300ºC for ten minutes. Multiple oxide layers were prepared by repeating the procedure, and a final annealing step was carried out at 300ºC for one hour [39, 66].

3.1.2. Co-precipitation method

According to Goldstein and Tseung, the hydroxide co-precipitation method could achieve high surface area spinel catalyst [65]. Sulfates of metals ($CoSO_4.7H_2O$ Analar BDH and $CuSO_4.5H_2O$ Analar BDH) were dissolved in distilled water and mixed in stoichiometric amounts (x= 0, 0.25, 0.5, 0.75, 1). The solution was kept at 70ºC with pure oxygen bubbling. When the solution is saturated with oxygen, 5M NaOH (≥98% Sigma Aldrich) was added slowly until the pH of the solution reached 11. The reaction mixture was held for one hour under these conditions. The precipitate was filtered, washed and dried in air and heated at 350ºC for 1hour. The obtained oxide powder was mixed with a 9 drops of 5% Triton X-100 to obtain a slurry and that was subsequently deposited on transparent conductive glass (FTO). The resulting film was heated at 360ºC for one hour to get an adherent oxide film. This process was repeated to get enough oxide loading [38].

3.2. Characterization of samples

The surface morphology of the films was examined with a scanning electron microscope (SEM = FEI, QUANTA 3D PEG) and the composition of the prepared films were analyzed by energy dispersive X-ray spectrometry (EDX = EDAX GENESIS). Karen Rethoret (EM laboratory technician) provided assistance and training for the use of SEM and EDX. X-ray diffraction patterns were recorded with a X-ray diffractometer (Bruker AXS D2 phaser) using Cu kα radiation of wavelength 0.15418 nm. This instrument is located in the X-ray powder diffraction lab at the University of Toronto and Dr. Srebri Petrov performed the measurements and data analysis. X-ray diffraction measurements were carried out using Cu kα radiation. Ni-

filter has been used to eliminate Cu Kβ radiation. High-resolution Solid State Lynxeye XE has been used as a detector and the Reitveld method was utilized for data refinement.

Cyclic voltammetry studies were carried out in a cylindrical Teflon cell in 1M KOH, and the potentials of the working electrode were measured against the SCE. Platinum wire was used as the counter electrode. The geometrical area of the electrode used in the studies was $0.50cm^2$. Cyclic voltammograms were recorded at a scan rate of $50mVs^{-1}$.

Catalytic activity of the prepared electrodes for the electroreduction of H_2O_2 was assessed using cyclic voltammetry. Cyclic voltammograms were recorded at room temperature using 3M NaOH containing 0.6M H_2O_2 at a scan rate of $5mVs^{-1}$. All measurements were performed in a cylindrical Teflon cell. Platinum wire and SCE were used as counter and reference electrodes, respectively.

The electrochemical surface area of the $Cu_xCo_{3-x}O_4$ electrodes was determined from double layer charging curves using cyclic voltammetry in a small potential region of -0.10mV to 10mV(SCE) in 1M KOH. The cyclic voltammograms were recorded at different scan rates and the charging current density was plotted as a function of scan rate.

Chapter 4: Results and discussions

This chapter will present the results obtained during our research. Firstly the surface morphology of films prepared by thermal decomposition and co-precipitation method are discussed through SEM micrographs. Secondly EDX analysis results are discussed to study composition of the materials. Subsequently structure analysis results obtained from X-ray diffraction analysis are presented. Finally cyclic voltammetry results for oxygen evolution reaction and electroreduction of H_2O_2 are presented for the films prepared by thermal decomposition method.

4.1. Film morphology – scanning electron microscopy (SEM)

The surface texture of the $Cu_xCo_{3-x}O_4$ electrodes, prepared by thermal decomposition method and co-precipitation method at various x values (x= 0, 0.25, 0.5, 0.75, 1), were analyzed by scanning electron microscopy.

SEM micrographs of various compositions of cobalt spinels provided information on the nature of the surface of the electrodes and offer a better understanding of the variations in the properties of the surface as a result of the addition of copper.

Two magnification values were chosen to report the morphology of the samples.SEM micrographs of Cu-Co oxides, prepared by co-precipitation method, are shown in Fig. 4.1. The oxides consist of indefinite flake shaped grains and no obvious difference in the morphology was observed with the variation of copper content. The grains are approximately 100 nm in size and the surface is very porous for all the compositions studied.

a)

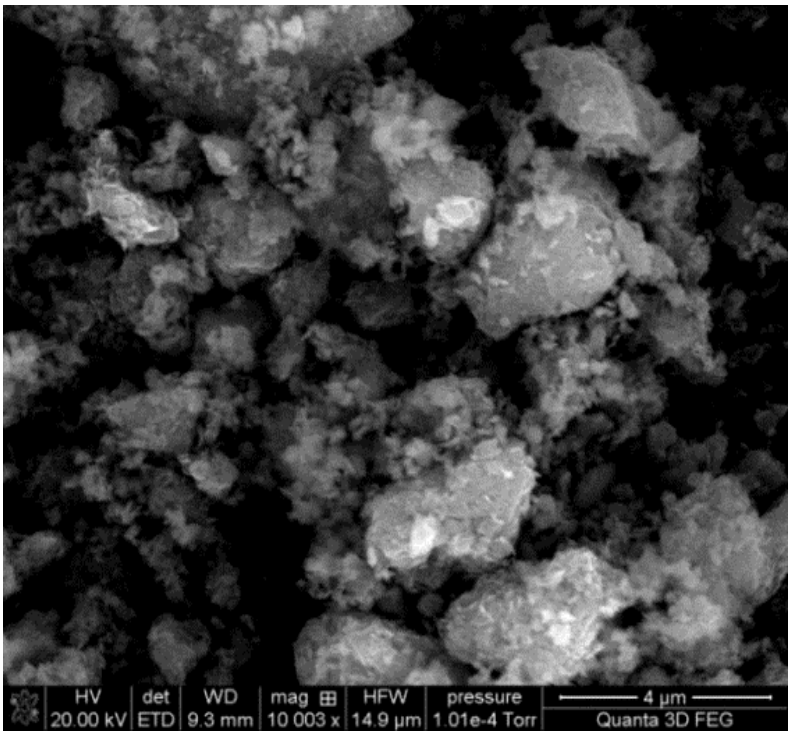
HV
20.00 kV
det
ETD
WD
9.3 mm
mag
10 003 x
HFW
14.9 µm
pressure
1.01e-4 Torr
4 µm
Quanta 3D FEG

b)

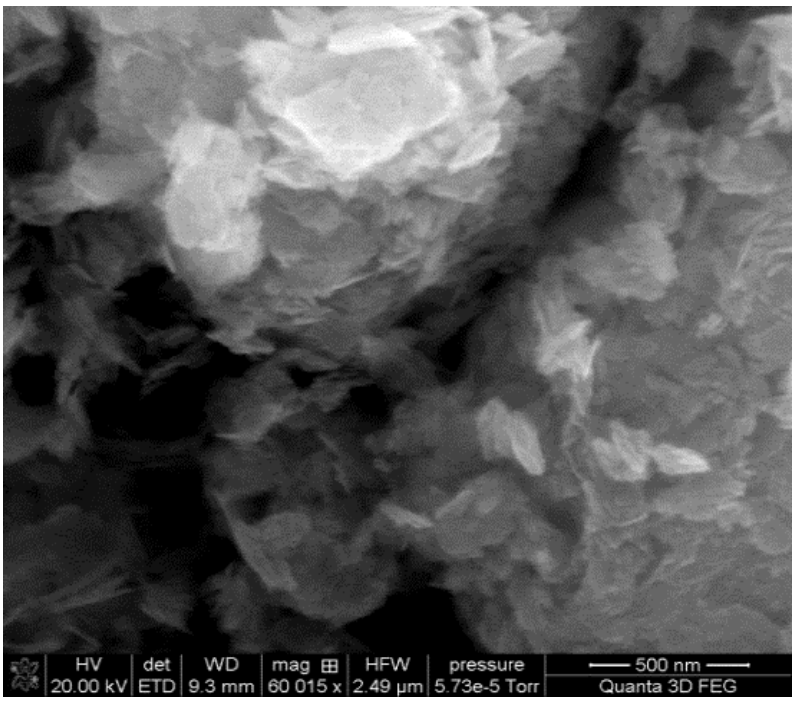
HV
20.00 kV
det
ETD
WD
9.3 mm
mag
60 015 x
HFW
2.49 µm
pressure
5.73e-5 Torr
500 nm
Quanta 3D FEG

c)

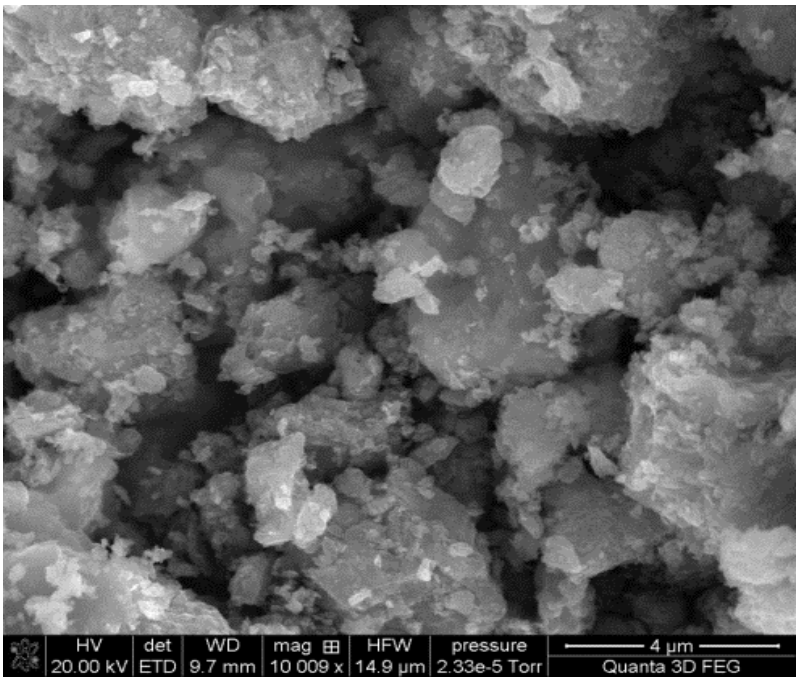
HV
20.00 kV
det
ETD
WD
9.7 mm
mag
10 009 x
HFW
14.9 µm
pressure
2.33e-5 Torr
4 µm
Quanta 3D FEG

d)

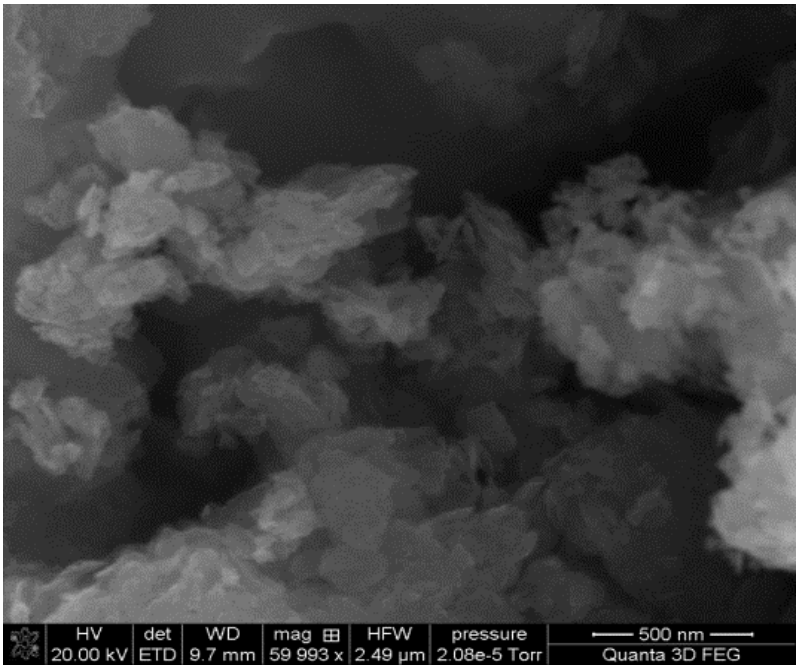
HV
20.00 kV
det
ETD
WD
9.7 mm
mag
59 993 x
HFW
2.49 µm
pressure
2.08e-5 Torr
500 nm
Quanta 3D FEG

e)

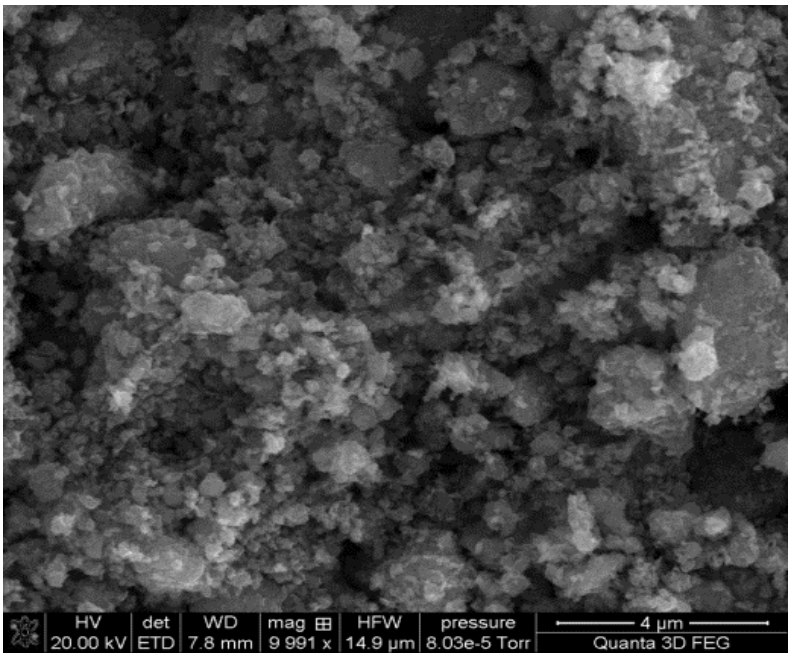
HV
20.00 kV
det
ETD
WD
7.8 mm
mag
9 991 x
HFW
14.9 µm
pressure
8.03e-5 Torr
4 µm
Quanta 3D FEG

f)

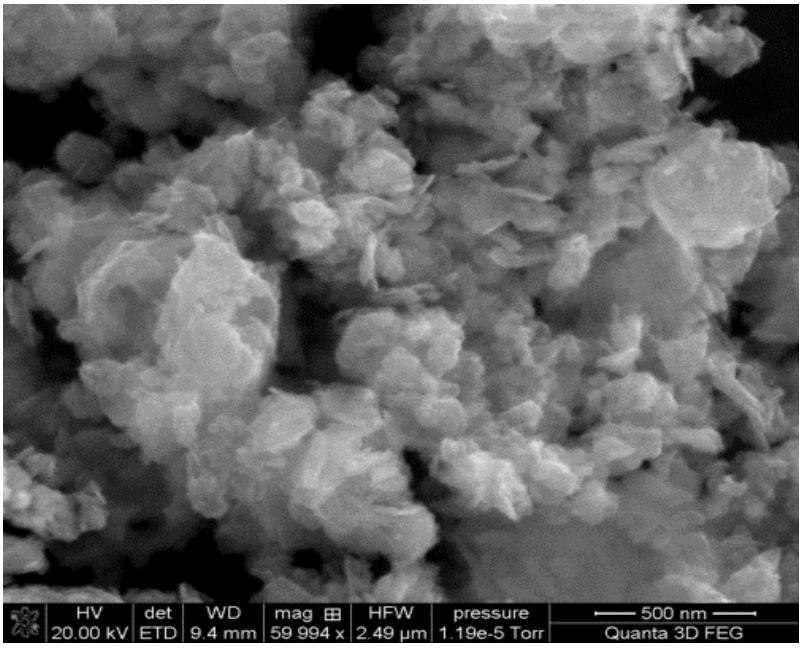
HV
20.00 kV
det
ETD
WD
9.4 mm
mag
59 994 x
HFW
2.49 µm
pressure
1.19e-5 Torr
500 nm
Quanta 3D FEG

g)

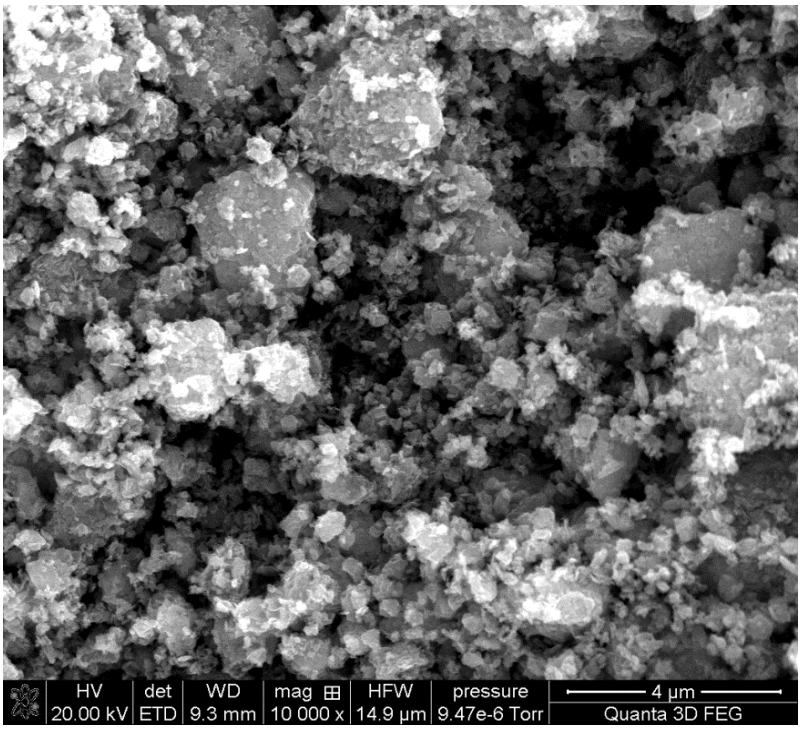
HV
20.00 kV
det
ETD
WD
9.3 mm
mag
10 000 x
HFW
14.9 µm
pressure
9.47e-6 Torr
4 µm
Quanta 3D FEG

h)

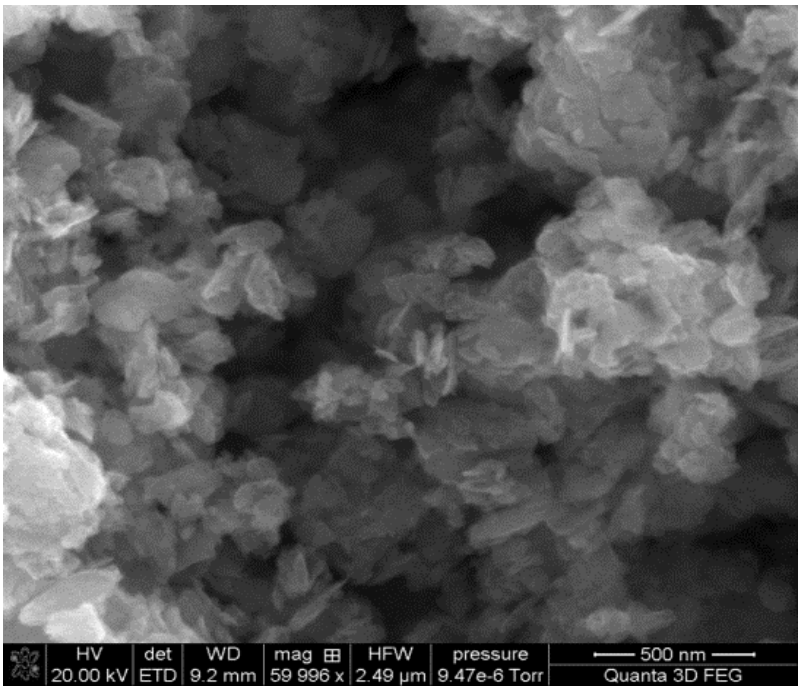
HV
20.00 kV
det
ETD
WD
9.2 mm
mag
59 996 x
HFW
2.49 µm
pressure
9.47e-6 Torr
500 nm
Quanta 3D FEG

i)

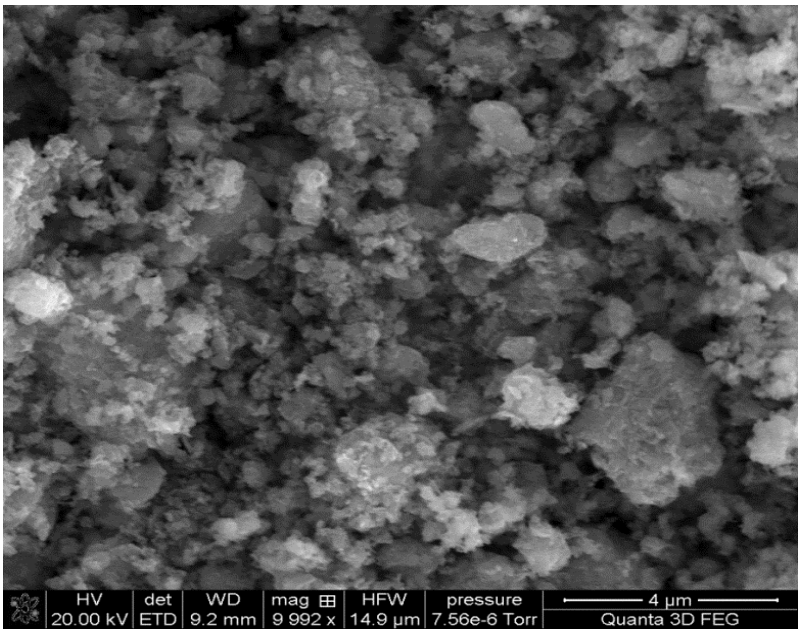

j)

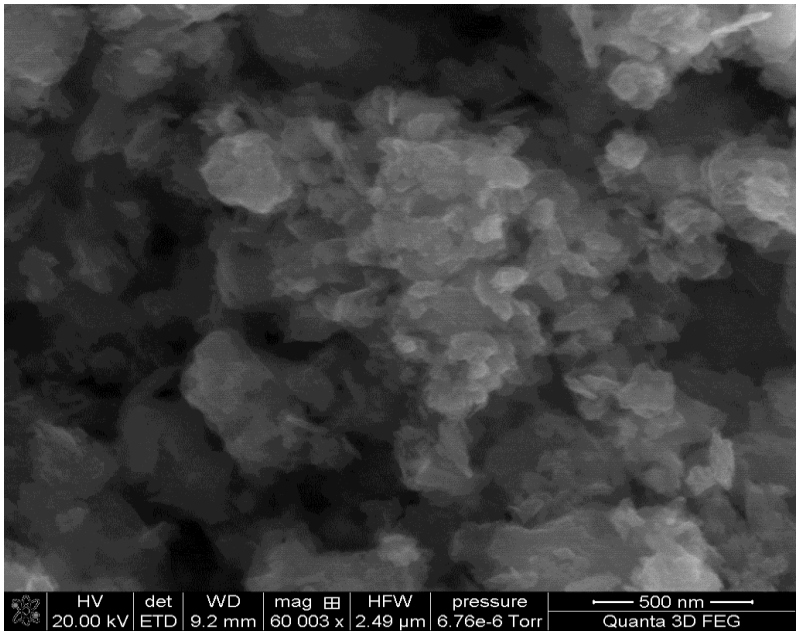

Fig. 4.1: SEM micrographs of a) and b) Co_3O_4, c) and d) $Cu_{0.25}Co_{2.75}O_4$, e) and f) $Cu_{0.5}Co_{2.5}O_4$, g) and h) $Cu_{0.75}Co_{2.25}O_4$, i) and j) $CuCo_2O_4$ prepared by co-precipitation method. Two magnification values were chosen for each samples as noted on the micrographs namely 10,000x (micrographs a), c), e), g) and i)) and 60,000x (micrographs b), d), f), h) and j)).

Fig. 4.2 shows the SEM micrographs of Cu-Co oxides prepared by the thermal decomposition method. In contrast with the case of the co-precipitation method, the SEM micrographs of the samples prepared by thermal decomposition show variations in their surface morphology with copper substitution.

The surface morphology of Co_3O_4 (Fig. 4.2 a) and b)) shows that grains were rather flat with a mean size of about 1-2µm. Copper substitution resulted in the formation of fine grains of Cu-Co oxides in the form of platelets that are oriented preferentially perpendicular to the surface, which may lead to an increased porosity of the oxide film. At higher copper substitution (x = 0.5) the surface appears more homogeneous, grains were uniformly covering the substrate and porosity appears to have further increased. In general, the size of Cu-Co oxide grains was found to be smaller than that of the pure Co_3O_4. The former is also observed to be quite anisotropic.

a)

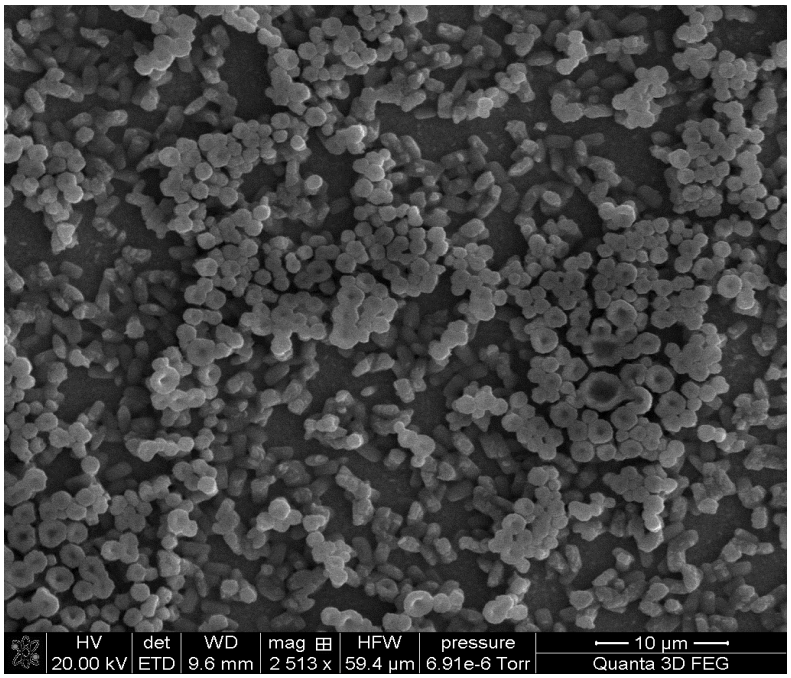

b)

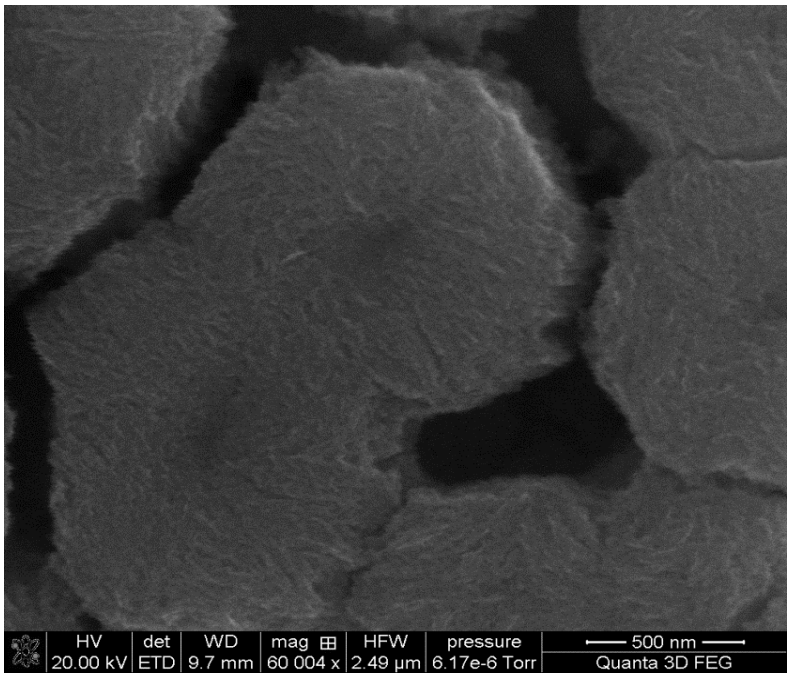
HV
20.00 kV
det
ETD
WD
9.7 mm
mag
60 004 x
HFW
2.49 µm
pressure
6.17e-6 Torr
500 nm
Quanta 3D FEG

c)

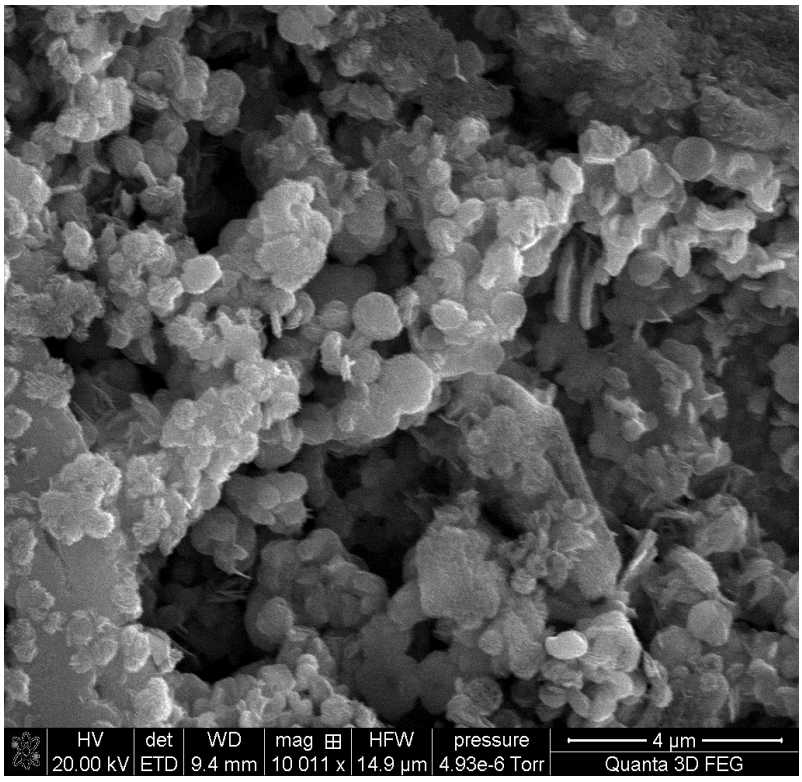
HV
20.00 kV
det
ETD
WD
9.4 mm
mag
10 011 x
HFW
14.9 µm
pressure
4.93e-6 Torr
4 µm
Quanta 3D FEG

d)

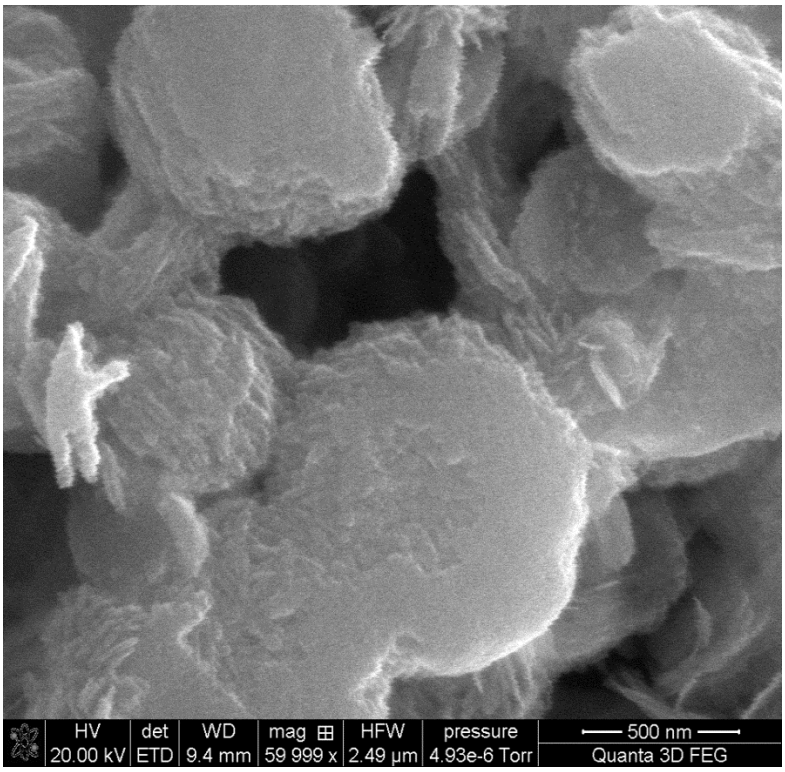
HV
20.00 kV
det
ETD
WD
9.4 mm
mag
59 999 x
HFW
2.49 µm
pressure
4.93e-6 Torr
500 nm
Quanta 3D FEG

e)

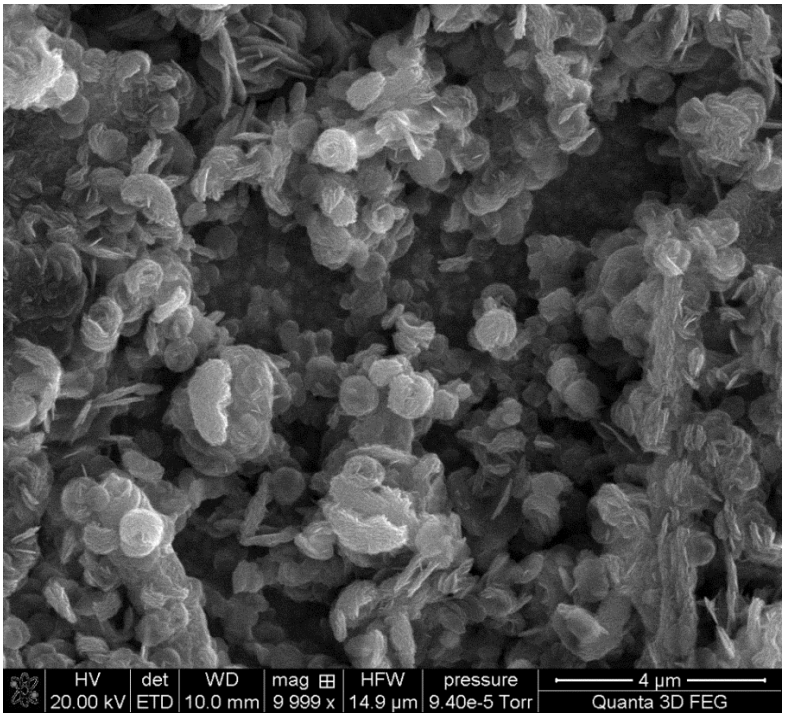
HV
20.00 kV
det
ETD
WD
10.0 mm
mag
9 999 x
HFW
14.9 µm
pressure
9.40e-5 Torr
4 µm
Quanta 3D FEG

f)

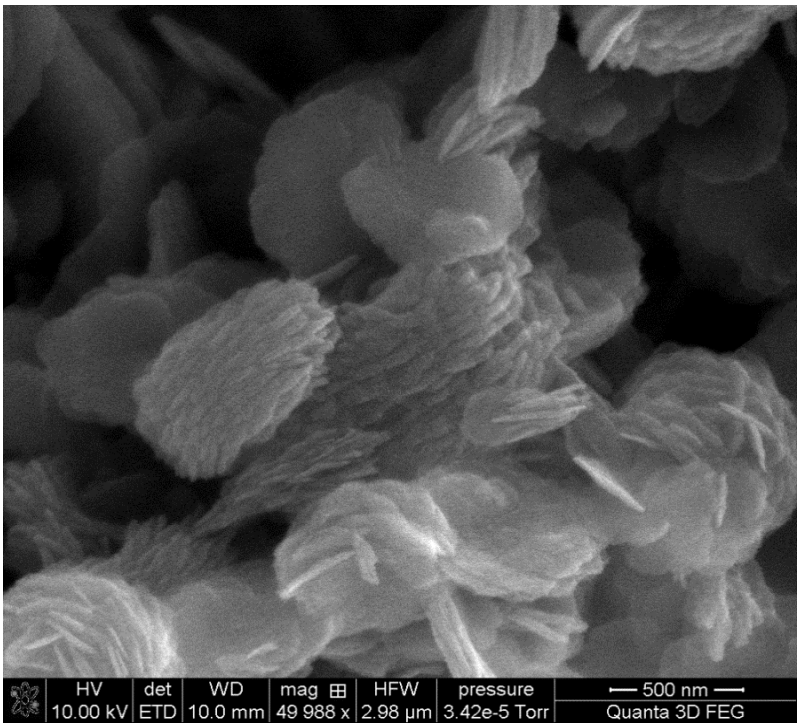
HV
10.00 kV
det
ETD
WD
10.0 mm
mag
49 988 x
HFW
2.98 µm
pressure
3.42e-5 Torr
500 nm
Quanta 3D FEG

g)

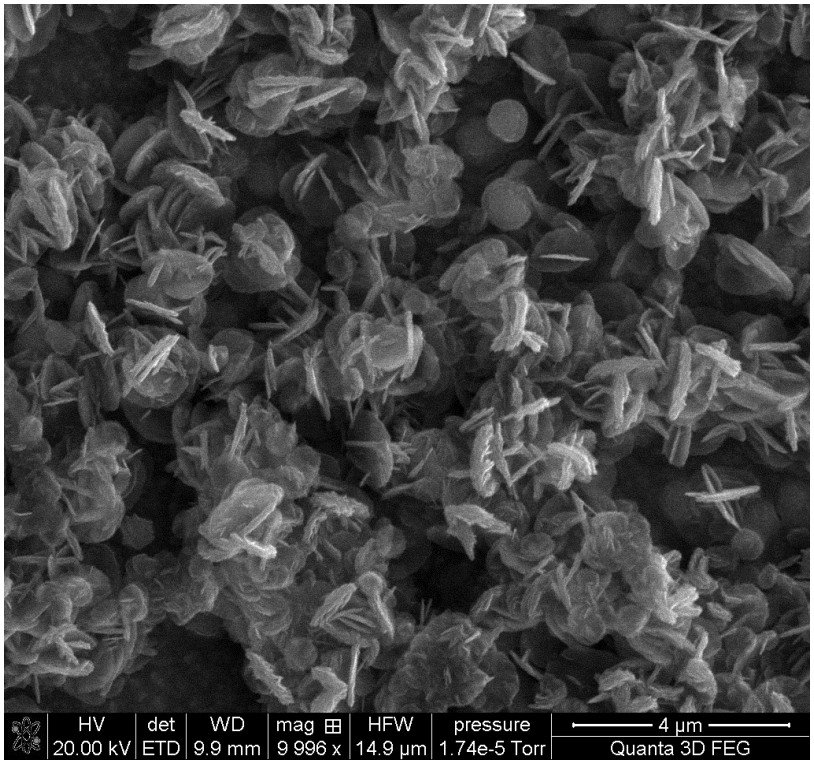
HV
20.00 kV
det
ETD
WD
9.9 mm
mag
9 996 x
HFW
14.9 µm
pressure
1.74e-5 Torr
4 µm
Quanta 3D FEG

h)

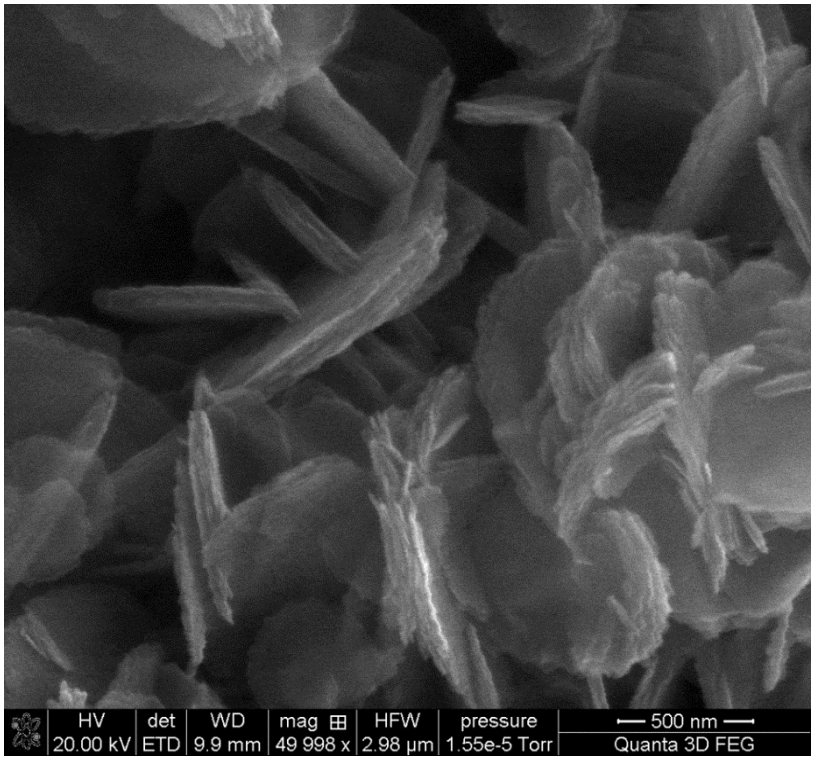
HV
20.00 kV
det
ETD
WD
9.9 mm
mag
49 998 x
HFW
2.98 µm
pressure
1.55e-5 Torr
500 nm
Quanta 3D FEG

i)

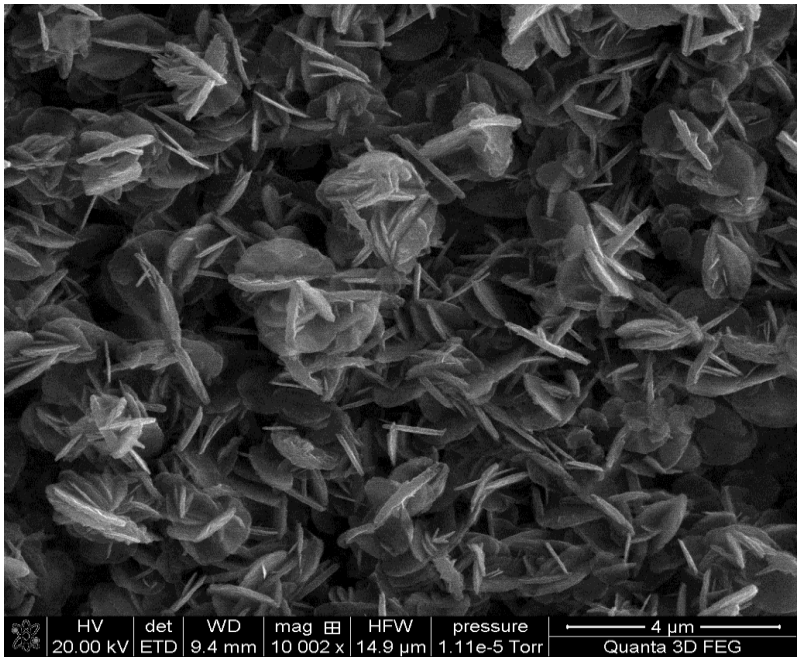
HV
20.00 kV
det
ETD
WD
9.4 mm
mag
10 002 x
HFW
14.9 µm
pressure
1.11e-5 Torr
4 µm
Quanta 3D FEG

j)

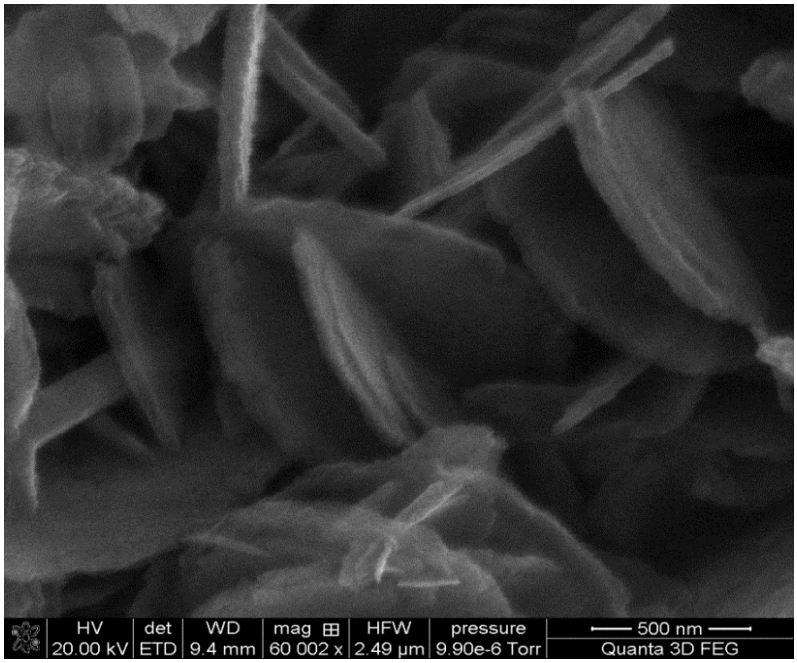

Fig. 4.2: SEM micrographs of a) and b) Co_3O_4; c) and d) $Cu_{0.25}Co_{2.75}O_4$; e) and f) $Cu_{0.5}Co_{2.5}O_4$; g) and h) $Cu_{0.75}Co_{2.25}O_4$; and i) and j)$CuCo2O_4$ prepared by thermal decomposition method. Different magnification values, namely ca. 2,500x (micrographs a)), 10,000x (micrographs c), e), g) and i)) and ca. 60,000x (micrographs b), d) f) h) j)), were chosen for each sample as noted on the micrographs.

4.2. Film composition - energy dispersion X-ray spectroscopy (EDX)

Energy dispersive X-ray spectroscopy is a powerful analytical technique for chemical analysis and is a useful tool to study the composition of the specimen. The analysis of $Cu_xCo_{3-x}O_4$ electrodes could provide information about the composition of copper cobalt oxides and the correlation between the stoichiometric and EDX elemental composition.

The elemental analysis of the $Cu_xCo_{3-x}O_4$ electrodes prepared by co-precipitation method is shown in the Fig.4.3 (a - e). The stoichiometric copper to cobalt ratio and the ratio obtained by the EDX analysis are listed in the Table 4.1. A good correlation exists between the stoichiometric and EDX copper to cobalt ratio for all the compositions prepared by co-precipitation method. EDX spectra of $Cu_xCo_{3-x}O_4$ prepared by the co-precipitation method indicate the presence of sulfur. It could be due to the incomplete removal of sulfates during the washing of the precipitate, which was originally presented as sulfates of metals.

EDX analysis of the electrodes prepared by thermal decomposition method is summarized in the Table 4.2. Thermal decomposition method also shows a good agreement between the stoichiometric and EDX ratio, even though copper cobalt ratio is slightly higher than stoichiometric ratio. The EDX spectra of $Cu_xCo_{3-x}O_4$ prepared by thermal decomposition method exhibits additional peaks of tin as it is deposited on fluorine doped tin oxide glass, are shown in the Fig. 4.4 (a – e).

a)

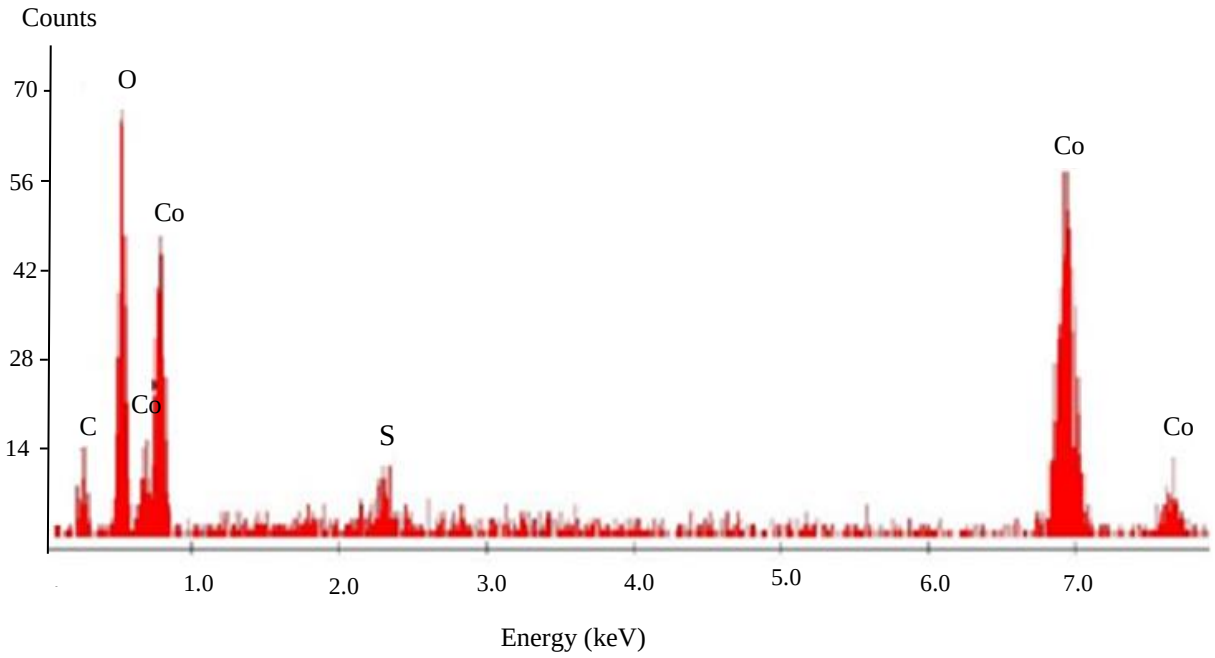
Counts
70
56
42
28
14
O
Co
Co
C
S
Co
Co
1.0
2.0
3.0
4.0
5.0
6.0
7.0
Energy (keV)

b)

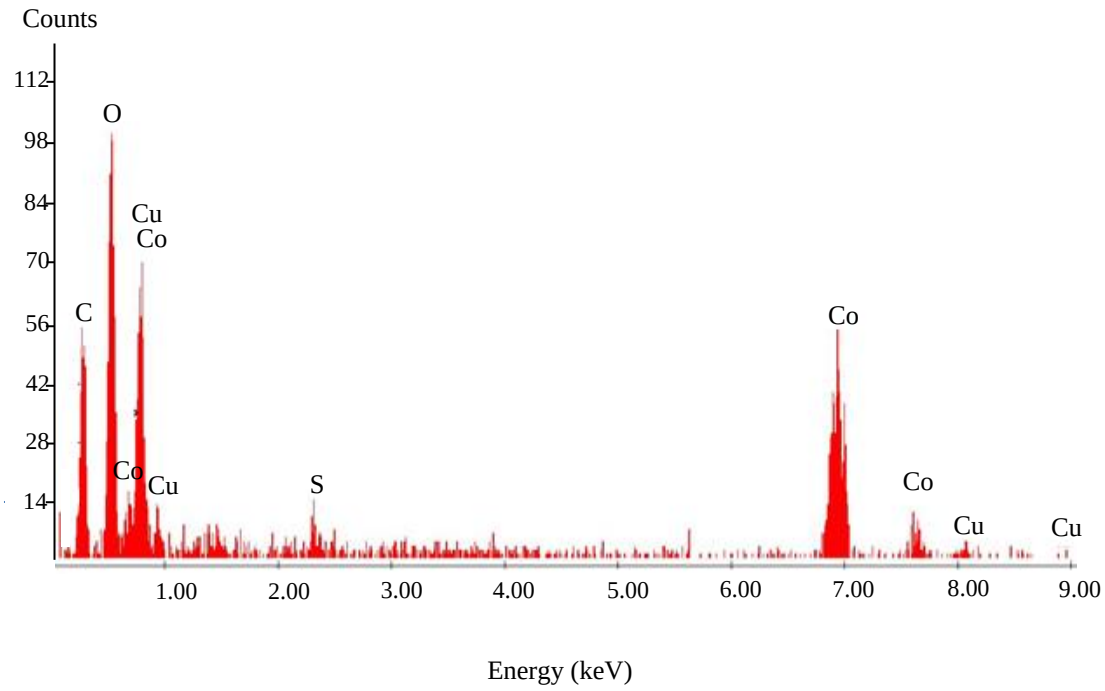
Counts
112
98
84
70
56
42
28
14
O
Cu
Co
C
Co
Cu
S
Co
Co
Cu
Cu
1.00
2.00
3.00
4.00
5.00
6.00
7.00
8.00
9.00
Energy (keV)

c)

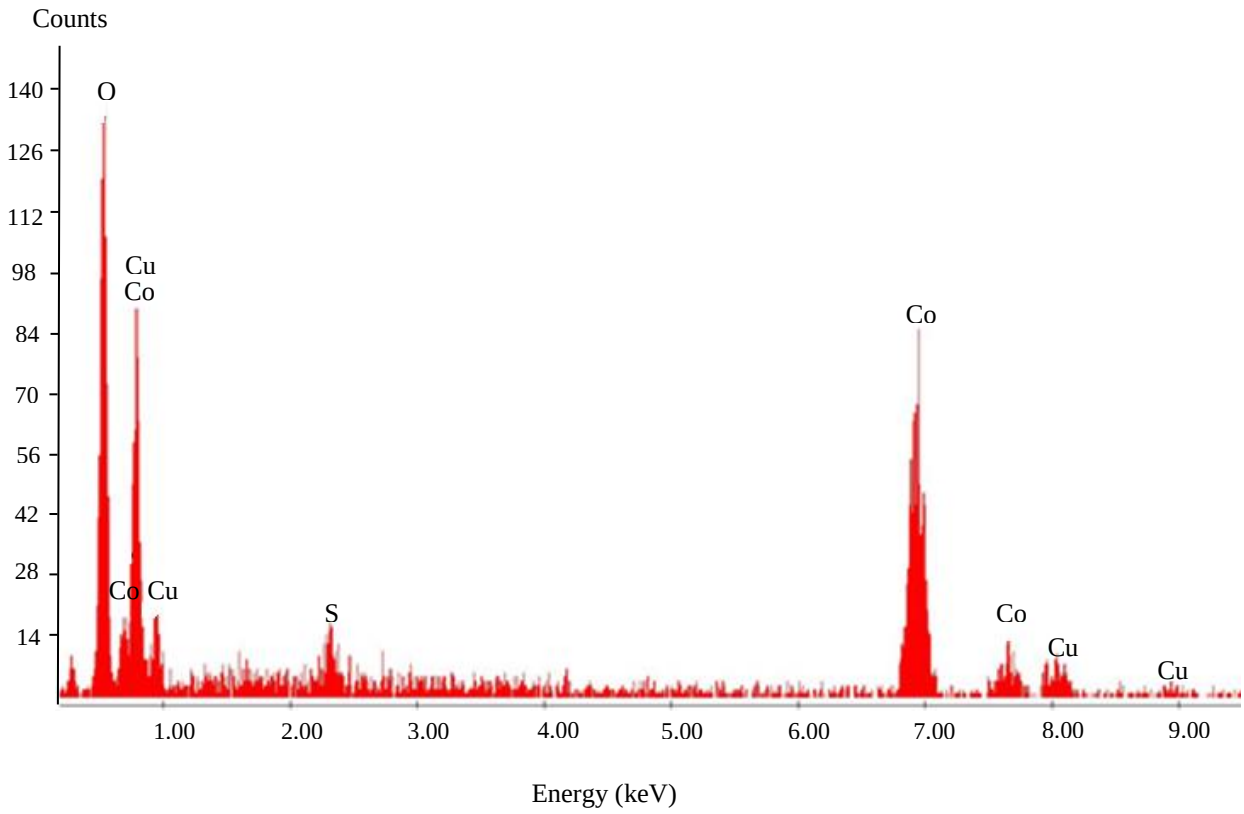
Counts
140
126
112
98
84
70
56
42
28
14
O
Cu
Co
Co Cu
S
Co
Co
Cu
Cu
1.00
2.00
3.00
4.00
5.00
6.00
7.00
8.00
9.00
Energy (keV)

d)

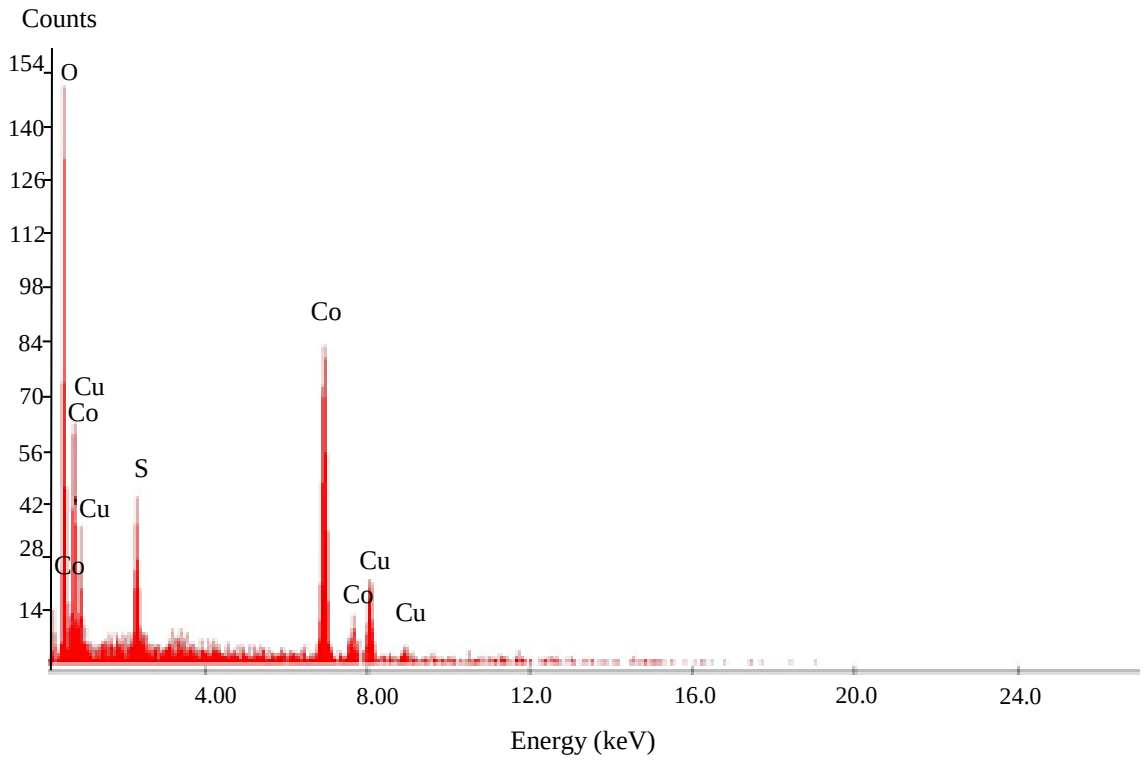
Counts
154
140
126
112
98
84
70
56
42
28
14
O
Cu
Co
S
Cu
Co
Co
Cu
Co
Cu
4.00
8.00
12.0
16.0
20.0
24.0
Energy (keV)

e)

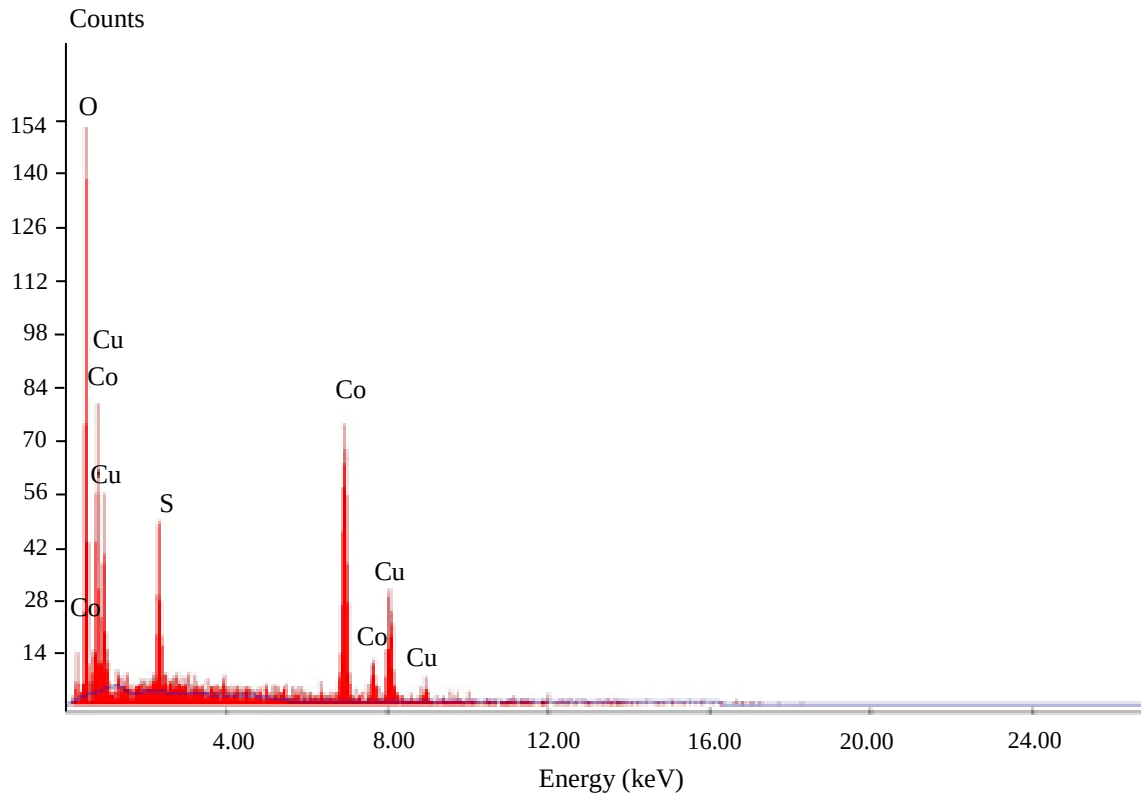

Fig. 4.3: EDX spectra of a) Co_3O_4, b) $Cu_{0.25}Co_{2.75}O_4$, c) $Cu_{0.5}Co_{2..5}O_4$, d) $Cu_{0.75}Co_{2.25}O_4$, and e) $CuCo_2O_4$ prepared by co-precipitation method.

`

a)

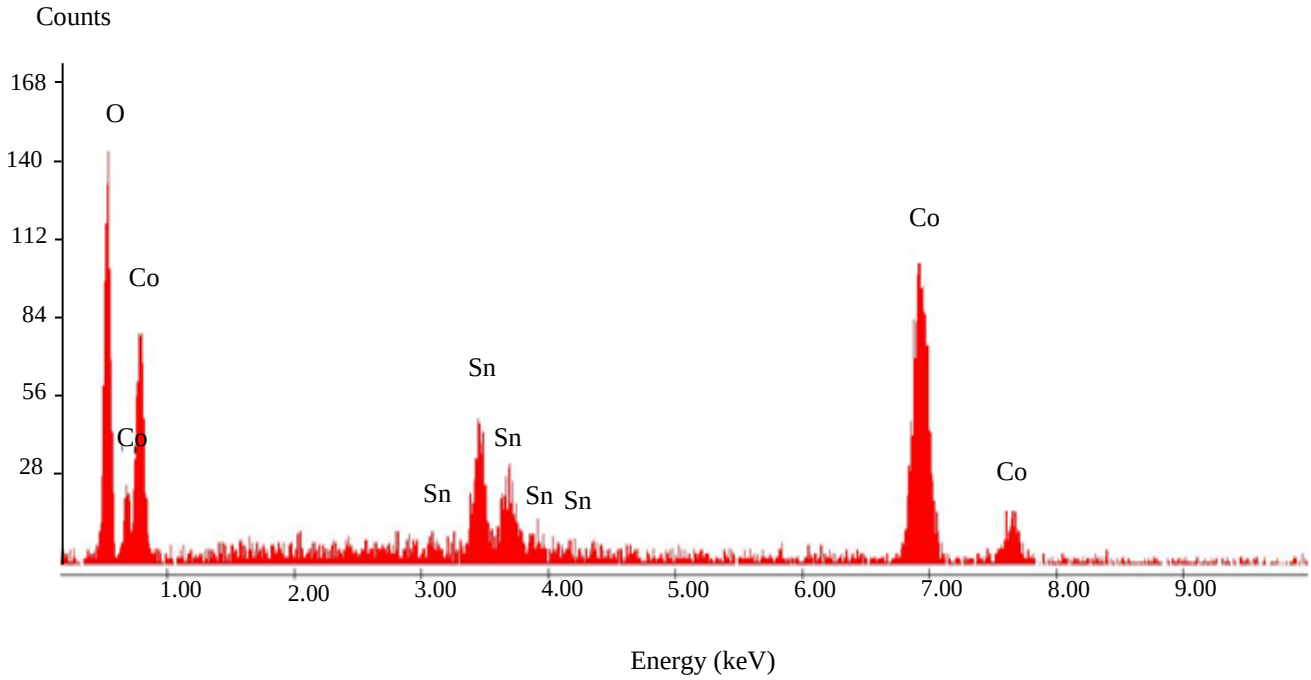
Counts
168
140
112
84
56
28
O
Co
Co
Sn
Sn
Sn
Sn
Sn
Co
Co
1.00
2.00
3.00
4.00
5.00
6.00
7.00
8.00
9.00
Energy (keV)

b)

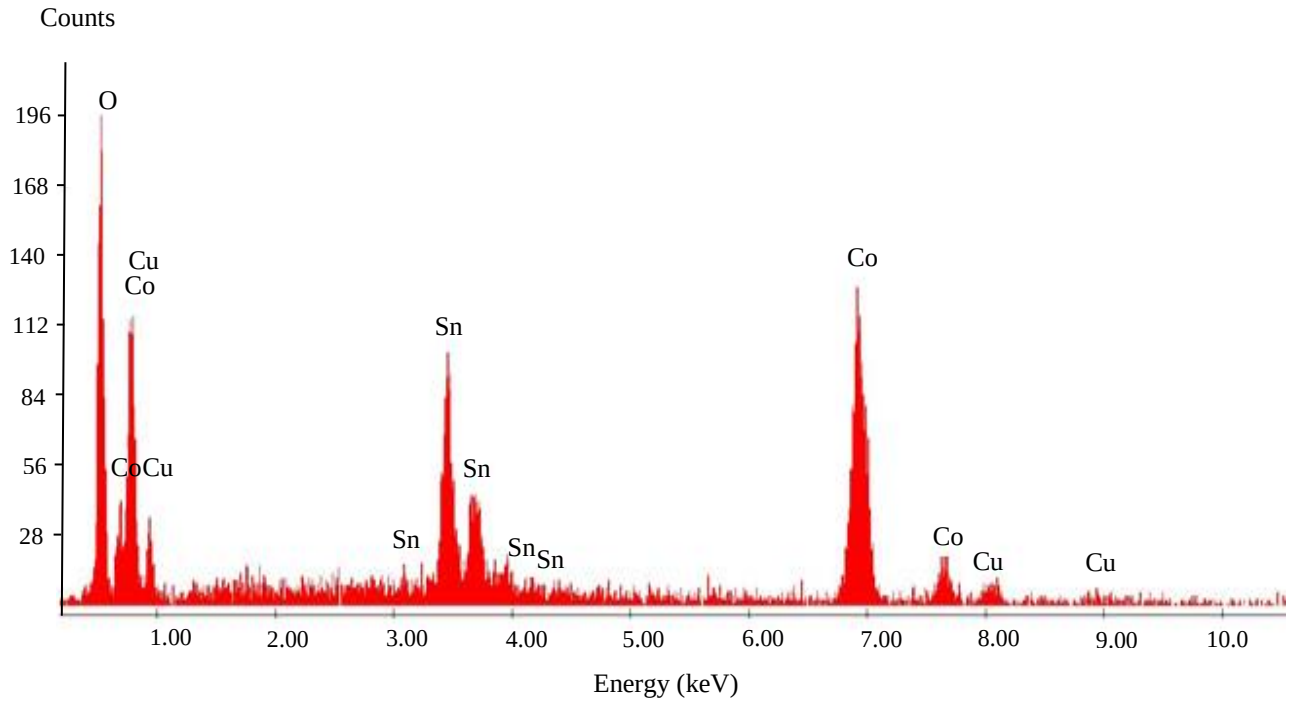
Counts
196
168
140
112
84
56
28
O
Cu
Co
Co
Cu
Sn
Sn
Sn
Sn
Sn
Co
Co
Cu
Cu
1.00
2.00
3.00
4.00
5.00
6.00
7.00
8.00
9.00
10.0
Energy (keV)

c)

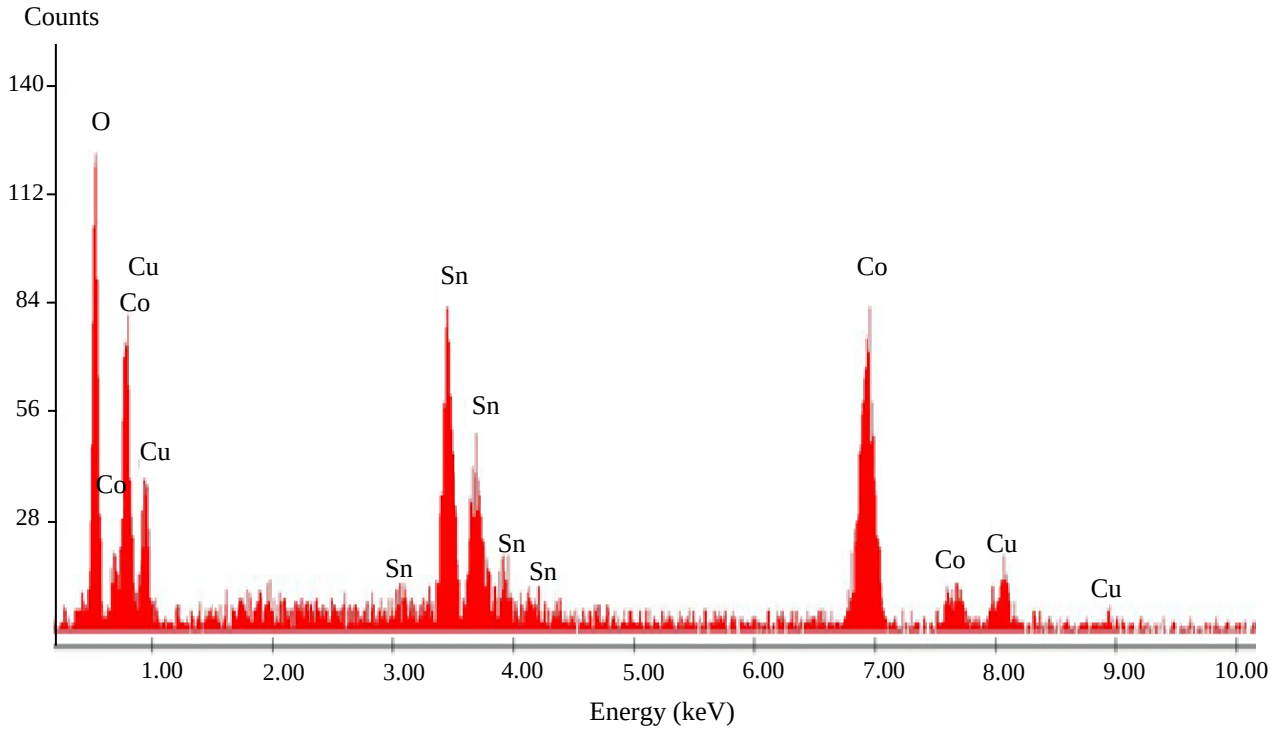
Counts
140
112
84
56
28
O
Cu
Co
Cu
Co
Sn
Sn
Sn
Sn
Sn
Co
Co
Cu
Cu
1.00
2.00
3.00
4.00
5.00
6.00
7.00
8.00
9.00
10.00
Energy (keV)

d)

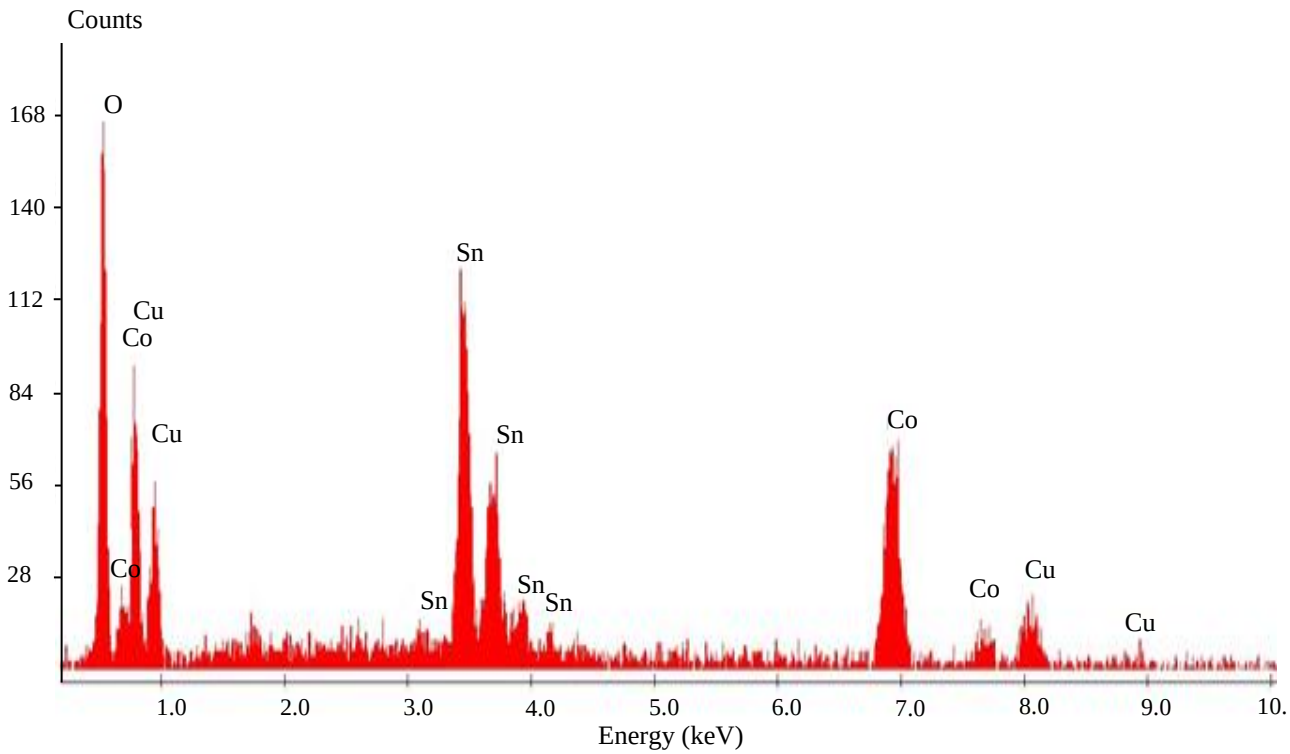
Counts
168
140
112
84
56
28
O
Cu
Co
Cu
Co
Sn
Sn
Sn
Sn
Sn
Co
Co
Cu
Cu
1.0
2.0
3.0
4.0
5.0
6.0
7.0
8.0
9.0
10.
Energy (keV)

e)

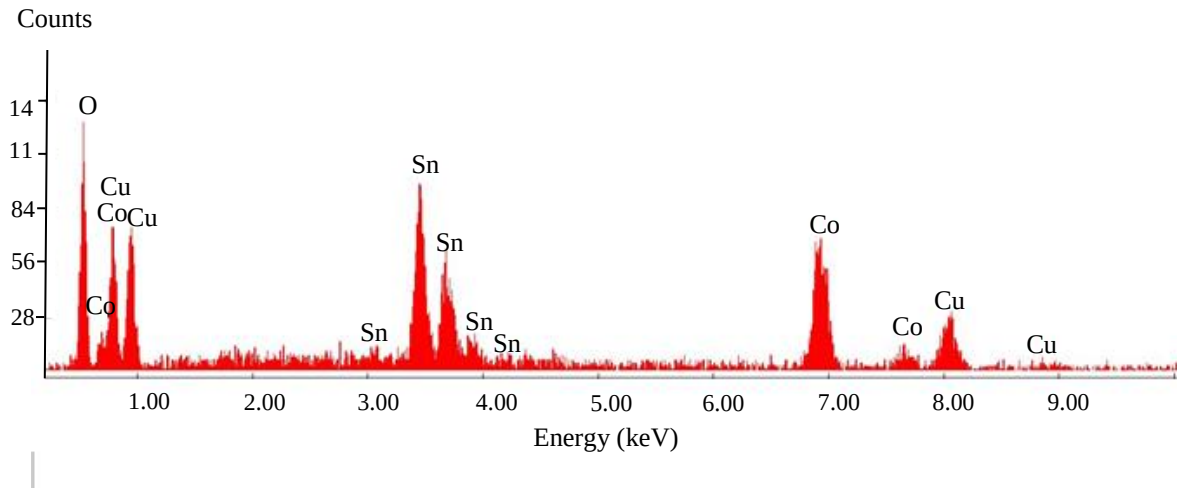

Fig. 4.4: EDX spectra of a) Co_3O_4, b) $Cu_{0.25}Co_{2.75}O_4$, c) $Cu_{0.5}Co_{2..5}O_4$, d) $Cu_{0.75}Co_{2.25}O_4$, and e) $CuCo_2O_4$ prepared by thermal decomposition method.

Table 4.1: Stoichiometric and EDX copper - cobalt ratio of the $Cu_xCo_{3-x}O_4$ electrodes prepared by co-precipitation method.

Stoichiometric Cu/Co ratio	(Cu/Co)EDX (Co-precipitation method) ± 17%	Expected Composition of the electrode	Composition of the electrode according to EDX measurement
0.00	0.00	Co_3O_4	Co_3O_4
0.09	0.10	$Cu_{0.25}Co_{2.75}O_4$	$Cu_{0.28}Co_{2.72}O_4$
0.20	0.23	$Cu_{0.5}Co_{2.5}O_4$	$Cu_{0.5}Co_{2.5}O_4$
0.33	0.39	$Cu_{0.75}Co_{2.25}O_4$	$Cu_{0.84}Co_{2.16}O_4$
0.50	0.54	$CuCo_2O_4$	$Cu_{1.05}Co_{1.95}O_4$

Table 4.2: Stoichiometric and EDX copper – cobalt ratio of the $Cu_xCo_{3-x}O_4$ electrodes prepared by thermal decomposition method.

Stoichiometric Cu/Co ratio	(Cu/Co)EDX (Thermal decomposition method) ± 17%	Expected Composition of the electrode	Composition of the electrode according to EDX measurement
0.00	0.00	Co_3O_4	Co_3O_4
0.09	0.11	$Cu_{0.25}Co_{2.75}O_4$	$Cu_{0.30Co2.70}O_4$
0.20	0.26	$Cu_{0.5}Co_{2.5}O_4$	$Cu_{0.62}Co_{2.38}O_4$
0.33	0.38	$Cu_{0.75}Co_{2.25}O_4$	$Cu_{0.83}Co_{2.17}O_4$
0.50	0.54	$CuCo_2O_4$	$Cu_{1.11}Co_{1.89}O_4$

For the co-precipitation method, samples with x value greater than 0.5, EDX copper-cobalt ratio tend to exceed what is expected based on the stoichiometry of the solution. The thermal decomposition method yielded a larger copper to cobalt EDX ratio with the addition of copper.

The error in the EDX measurement may arise from the homogeneity of the material. In order to evaluate this error, copper cobalt ratio was measured at different spots of the same sample ($CuCo_2O_4$) and the standard deviation and relative error were calculated. Both thermal decomposition method and co-precipitation method shows a relative error of 17%.

The error, which may be generated during the preparation of the solution, will also affect the final composition of the $Cu_xCo_{3-x}O_4$ electrode. However, the error calculation shows that for the co-precipitation and thermal decomposition methods the resulting errors on the Cu/Co ratio are between 0.7 and 1.7%, and between 2.5 and 5.1%, respectively (see Tables A4 and A6 in the appendix). This indicates that the majority of the error is inerrant to the EDX method and possible inhomogeneity of the material.

However, it is not possible to confirm with EDX if Cu is actually being substituted in the spinel structure. This was investigated using x-ray diffraction and the results are presented in the next section.

4.3. Film structure X-ray diffraction

X-ray diffraction is a powerful technique for elucidating the structure of crystalline materials and determining the atomic arrangement in space with high precision. X-ray diffraction analysis of $Cu_xCo_{3-x}O_4$ electrodes reveals the structure of the material and provides information on how addition of copper affects the structure of the Co_3O_4 lattice.

The X-ray diffraction pattern of Co_3O_4 and $Cu_{0.5}Co_{2.5}O_4$, prepared by the co-precipitation method, are given in Fig. 4.5. The circles in the plot represent the experimental data obtained from the sample (labeled 1). The curve along these circles was obtained after refinement. The extracted peaks are shown below this curve (labeled 2). The bottom line represents the discrepancies between this curve and the experimental data (labeled 3). Using the Reitveld method it is possible to identify the presence of other phase present in the samples as shown in Fig. 4.5 b).

XRD pattern of Co_3O_4 displays characteristic peaks of the cubic spinel structure with space group Fd3m .The peaks can be indexed to the planes of cobalt spinel, namely (220), (311), (222), (400), (422), (511) and (400). XRD patterns of $Cu_{0.5}Co_{2.5}O_4$ show the evidence for the formation of CuO crystalline phase along with spinel structure. The extracted peaks of CuO are shown by the curve (4). The lattice parameter (a_0) was calculated from the d spacing of the highest intensity plane (311) using the formula:

$$a_0 = d\,(h^2 + k^2 + l^2)^{1/2}$$

Where h, k, l are Miller indices. The lattice parameters of Co_3O_4 and $Cu_{0.5}Co_{2.5}O_4$ are 8.092 ± 0.007 Å and 8.099 ± 0.007 Å respectively. A small increase in the lattice parameter supports the incorporation of some copper in the spinel lattice of Co_3O_4. The error associated with the lattice parameter was calculated using the standard deviation of two sets of experimental values obtained by Reitveld refinement.

The cobalt spinel lattice accommodates copper ions forming a solid solution until it becomes oversaturated. At the oversaturation, a new phase of CuO segregate, which act as resistive phase in the spinel structure; decrease the electrocatalytic activity of the electrode [14]. The X-ray

analysis of $Cu_{0.5}Co_{2.5}O_4$ indicates the formation of 2.8 ± 0.7% CuO crystalline phase along with spinel structure. The error associated with the percent of CuO was determined by performing the Reitveld analysis several times (three times) with slightly different parameters (see section A.3 in the appendix).

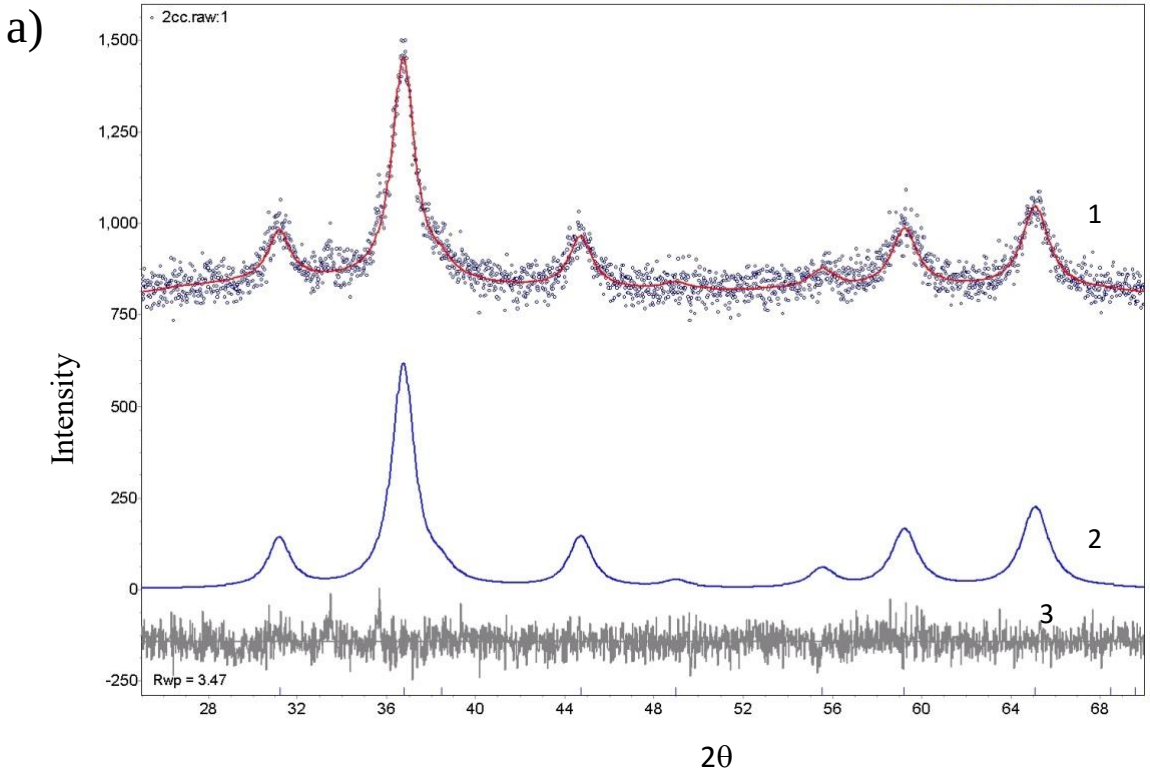

b)

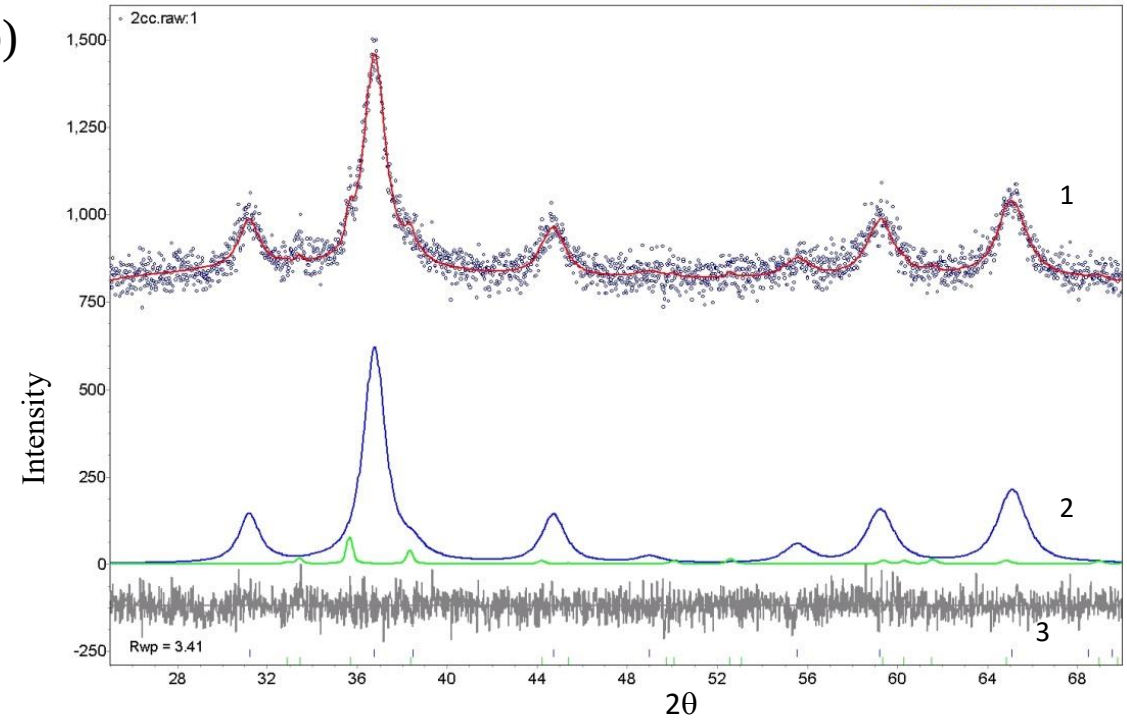

Fig. 4.5: XRD patterns of a) Co_3O_4 and b) $Cu_{0.5}Co_{2.5}O_4$ prepared by Co-precipitation method. Note that in (b) 2.8 ± 0.7% of monoclinic CuO is detected.

XRD patterns of $Cu_xCo_{3-x}O_4$ electrodes prepared by thermal decomposition method are shown in Fig.4.6. All the samples exhibit characteristic peaks assigned to the spinel structure. $CuCo_2O_4$ sample has additional peaks from CuO crystalline phase and this corresponds to the sample containing 9.8 ± 0.6% of CuO (Fig. 4.6 e)). The error associated with the percent of CuO was determined by performing the Reitveld analysis several times (three times) with slightly different parameters (see section A.3 in the appendix).

a)

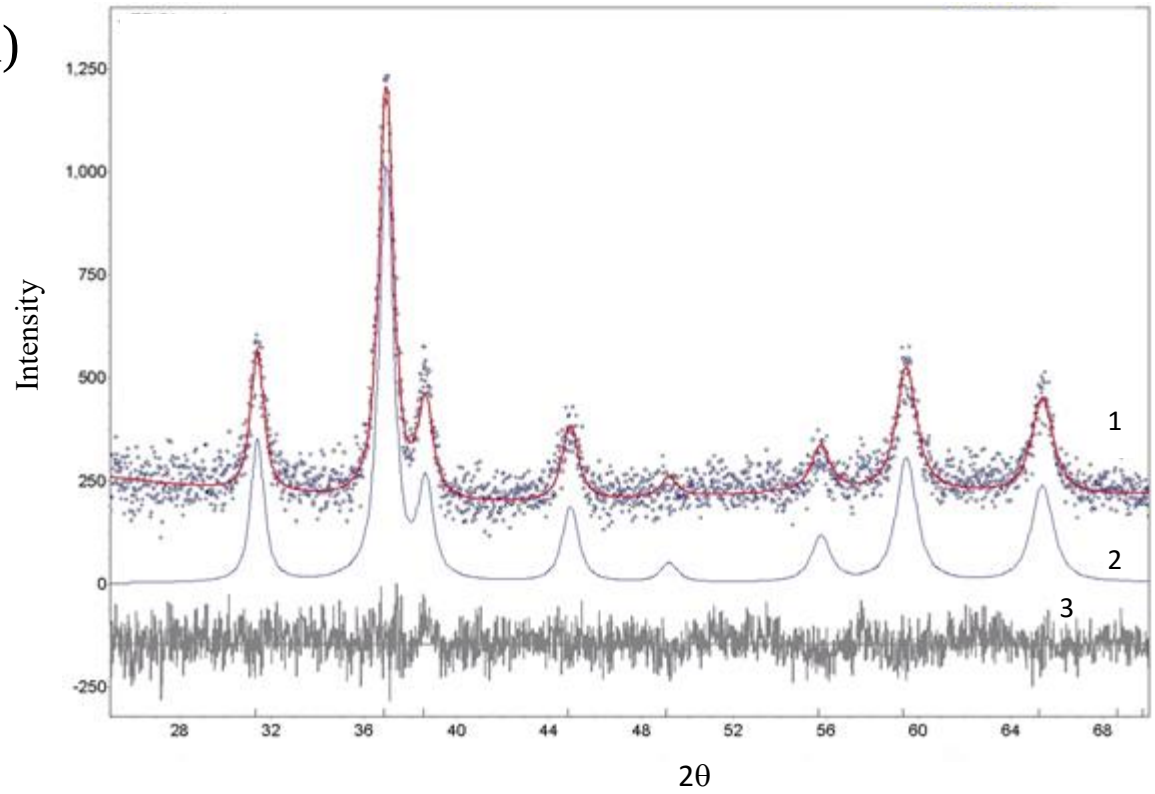
Intensity
1,250
1,000
750
500
250
0
-250
28
32
36
40
44
48
52
56
60
64
68
1
2
3
2θ

b)

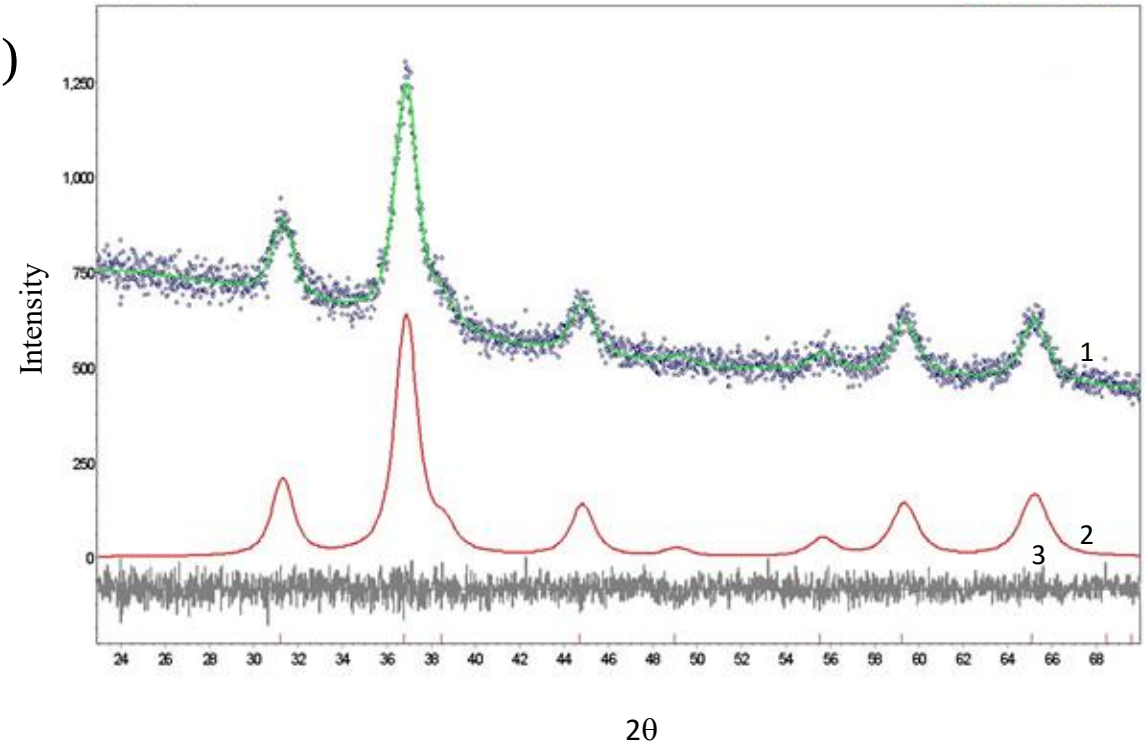
Intensity
1,250
1,000
750
500
250
0
24
26
28
30
32
34
36
38
40
42
44
46
48
50
52
54
56
58
60
62
64
66
68
1
2
3
2θ

c)

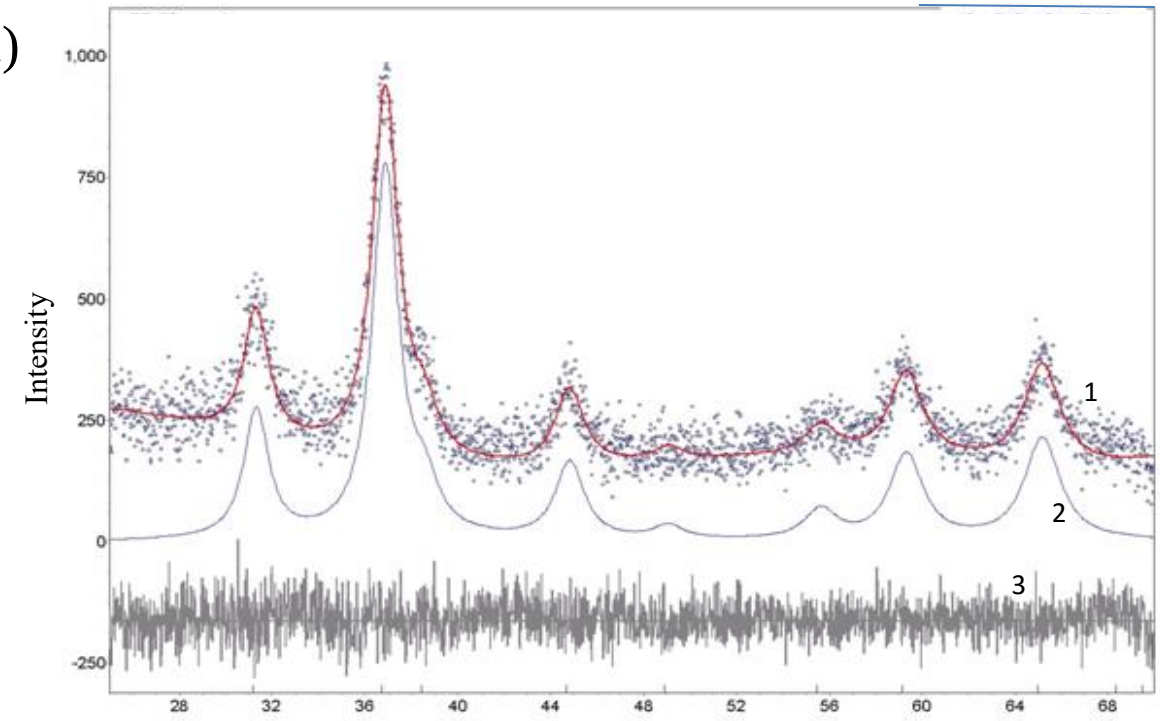
Intensity
1,000
750
500
250
0
-250
28
32
36
40
44
48
52
56
60
64
68
1
2
3

2θ

d)

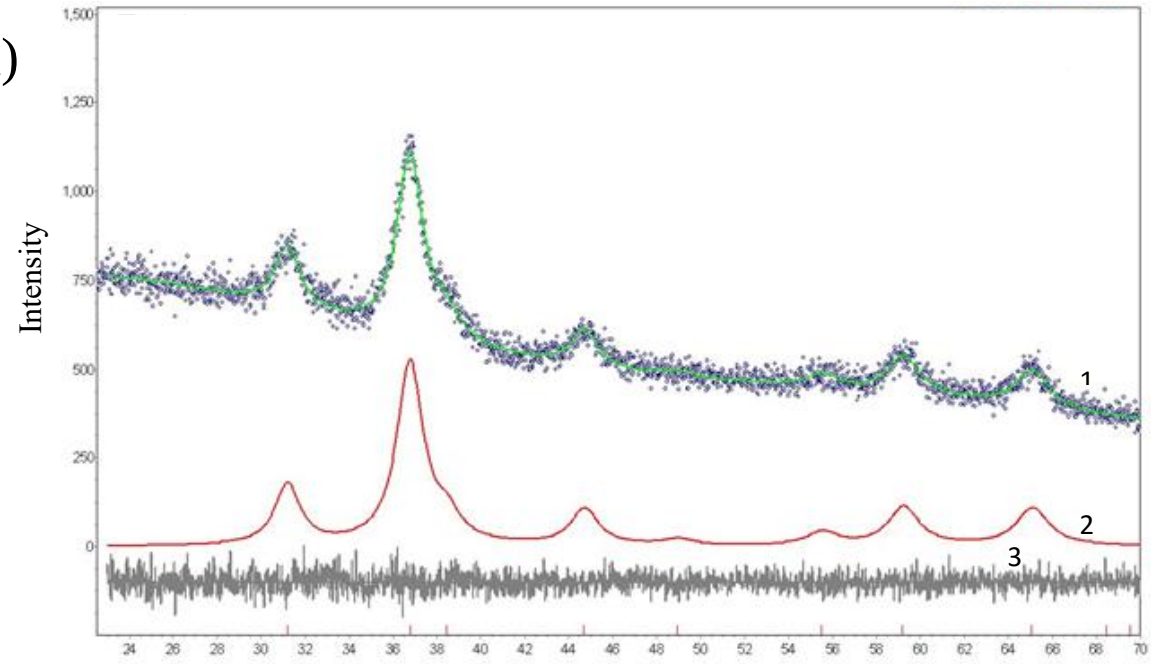
Intensity
1,500
1,250
1,000
750
500
250
0
24
26
28
30
32
34
36
38
40
42
44
46
48
50
52
54
56
58
60
62
64
66
68
70
1
2
3

2θ

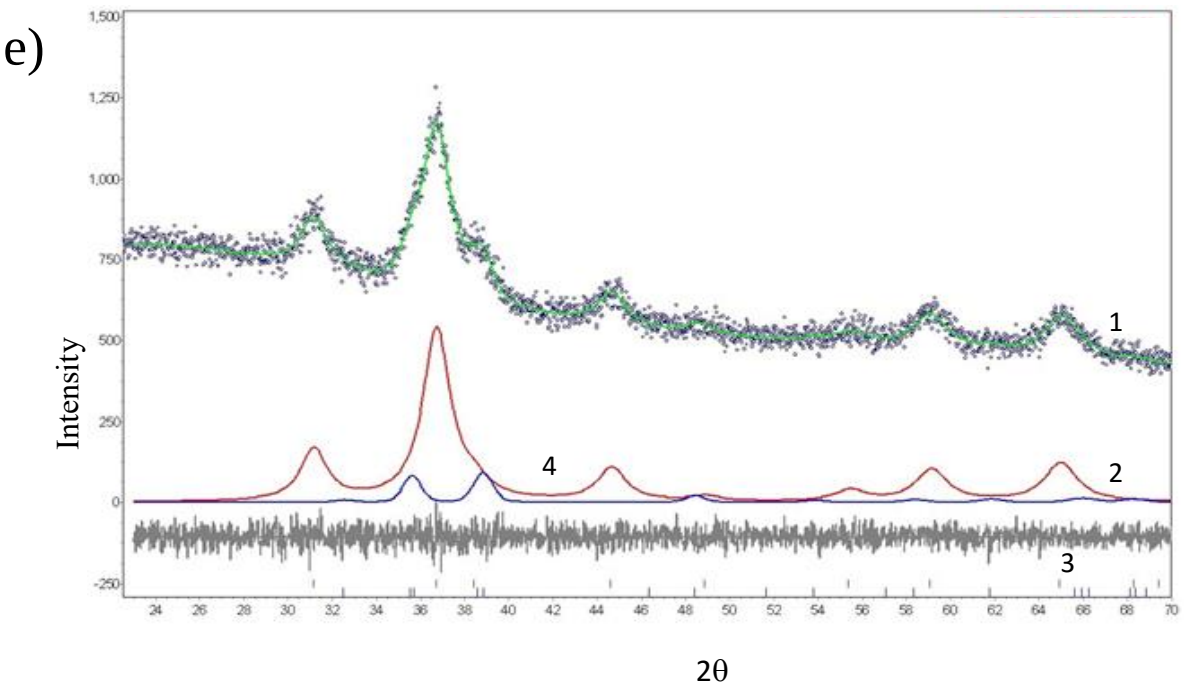

Fig. 4.6: XRD patterns of (a) Co_3O_4 (b) $Cu_{0.25}Co_{2.75}O_4$, (c) $Cu_{0.5}Co_{2.5}O_4$, (d) $Cu_{0.75}Co_{2.25}O_4$, and (e) $CuCo_2O_4$ prepared by thermal decomposition method.

The lattice parameter calculation indicates an increase in the lattice parameter with the increase of copper content, which would explain the substitution of cobalt ions by copper ions in the spinel lattice. The a_0 values for different x values are listed in the Table 4.3. In thermal decomposition method, the error associated with the lattice parameter ranges from ±0.002 Å to ±0.009 Å, which is estimated by calculating the standard deviation of two set of lattice parameter values obtained by the Reitveld refinement method.

La Rosa *et al.* reported the lattice parameters of $Cu_xCo_{3-x}O_4$ films on titanium support prepared by thermal decomposition method [16]. In Fig. 4.7, a graph is plotted between the lattice parameter constant and copper-cobalt ratio of $Cu_xCo_{3-x}O_4$ electrodes, and is compared to

the lattice parameter obtained by La Rosa *et al.* The slope obtained from the linear regression of the graph shows that La Rosa *et al.* obtained a higher slope (0.082 ± 0.019 Å) compared to the slope (0.060 ± 0.020 Å) obtained in this work. This may indicate a higher incorporation of copper in the spinel lattice prepared by La Rosa *et al.* [16].

Table 4.3: The lattice parameter of $Cu_xCo_{3-x}O_4$ electrode prepared by thermal decomposition method

Composition	Lattice parameter (Å)
Co_3O_4	8.084 ± 0.003
$Cu_{0.25}Co_{2.75}O_4$	8.099 ± 0.002
$Cu_{0.5}Co_{2.5}O_4$	8.106 ± 0.003
$Cu_{0.75}Co_{2.25}O_4$	8.108 ± 0.003
$CuCo_2O_4$	8.114 ± 0.009

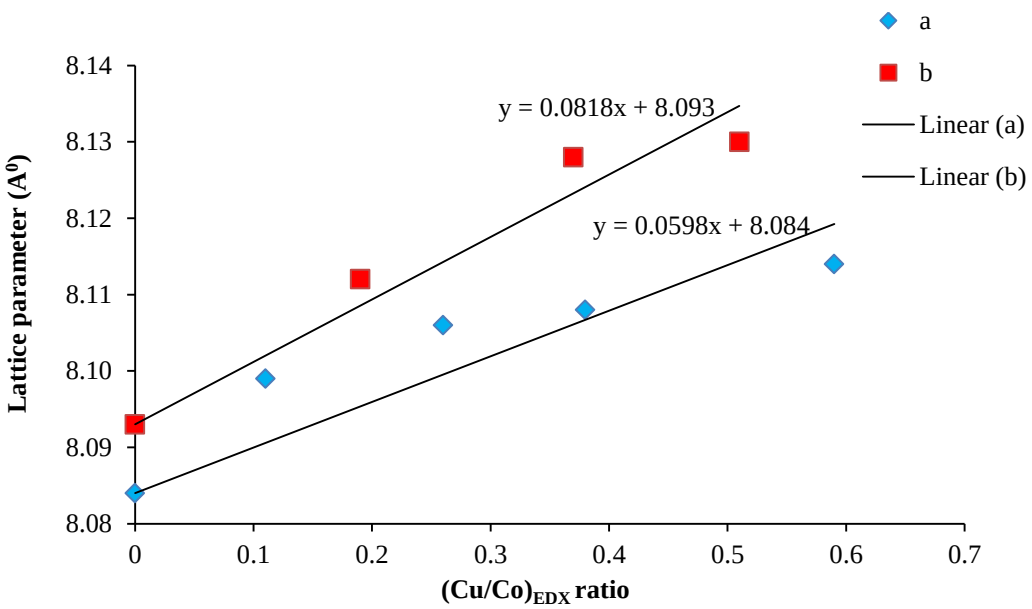

Fig. 4.7: Graphical representation of $(Cu/Co)_{EDX}$ ratio in $Cu_xCo_{3-x}O_4$ as a function of lattice parameter for (a) the lattice parameter of the prepared film ($Cu_xCo_{3-x}O_4$) in this work, and (b) the lattice parameter of the $Cu_xCo_{3-x}O_4$ films prepared by La Rosa *et al* [16].

However, one should note that the lattice parameters for pure cobalt oxide vary for both series of samples. According to JCPDS-ICDD 9-418 the lattice parameter of pure Co_3O_4 is 8.084 Å. A similar lattice parameter of 8.084 ± 0.003 Å was obtained in this work. La Rosa *et al.* obtained a higher lattice parameter (8.093Å). This increase in the lattice parameter may be due to the influence of the titanium support on the crystallographic properties of the oxide.

Table 4.4: Percent of CuO detected in the $Cu_xCo_{3-x}O_4$ electrode prepared by co-precipitation and thermal decomposition methods.

Composition of the electrode	Percentage of CuO (Co-precipitation method) ± 0.7%	Percentage of CuO (Thermal decomposition method) ± 0.6%
Co_3O_4	ND[1]	ND[1]
$Cu_{0.25}Co_{2.75}O_4$	NM[2]	ND[1]
$Cu_{0.5}Co_{2.5}O_4$	2.8	ND[1]
$Cu_{0.75}Co_{2.25}O_4$,	NM[2]	ND[1]
$CuCo_2O_4$	NM[2]	9.8

[1]ND: not detected

[2]ND: not measured

Based on the data presented and discussed so far, it was found that the electrodes prepared by thermal decomposition method possess a single phase spinel structure up to an x value of 0.75. The unit cell expansion with the addition of copper explains the effective incorporation of copper into the spinel lattice and support the formation of a solid solution.

The XRD analysis of $Cu_{0.5}Co_{2.5}O_4$ electrode (x = 0.5) prepared by co-precipitation method indicated the evidence of diffraction lines of characteristic monoclinic CuO phase along with spinel structure, which suggests that the thermal decomposition method can incorporate a higher amount of copper than the co-precipitation method. One can see that there are sharp differences in the mean particle sizes of the second phase (CuO) in both samples. In the sample $Cu_{0.5}Co_{2.5}O_4$,

prepared by co-precipitation method, the peaks corresponding to CuO phase appears sharper, which resulted from the large mean particle size of CuO (95 nm), while in $CuCo_2O_4$, prepared by thermal decomposition method, the peaks are broadened due to the small particle size of CuO particles (6 nm).

Also the electrodes prepared by thermal decomposition method were shown to be stable in solution environment. The samples prepared via co-precipitation method were unstable in solution; significant material lost was observed over a short time after immersion in the electrolyte, most likely due to a poor adhesion even after annealing. Hence the electrochemical characterization will be performed using the samples prepared by the thermal decomposition method.

4.4. Surface Area characterization and Electrocatalytic behavior - cyclic voltammetry

Cyclic Voltammetry is a widely used analytical technique to investigate electrochemical processes under various conditions. It is a useful way to identify the surface redox transition and to study the electrocatalytic properties of an analyte. The cyclic voltammogram of $Cu_xCo_{3-x}O_4$ provides information about the redox potential of the electrode at various compositions. It also tells how the variations in the composition influence the electrocatalytic property of the film.

4.4.1. Roughness factor (R_F)

Knowledge about the real surface area allows us to compare the experimental results on different materials, since this parameter is likely to differ from one sample to the next. Cyclic voltammetry has been used to determine the real surface area of $Cu_xCo_{3-x}O_4$ electrodes [36, 37].

The cyclic voltammograms shown in Fig. 4.8 were recorded in 1M KOH at varying scan rates for a narrow potential range, i.e., -0.100 mV to 100 mV (SCE). The anodic and cathodic current densities for each electrode were found to have nearly equal magnitude at different scan rates. The current density in the middle of the narrow potential region (i.e., 0 mV) is plotted vs. scan rate and a linear plot was obtained, both anodic and cathodic slopes were measured and an average was calculated, which gives the double layer capacitance (C_{dl}) of the sample (Fig.4.9). The roughness factor (R_F) was calculated as the ratio of C_{dl} of $Cu_xCo_{3-x}O_4$ oxide and that of a smooth surface (i.e., 60 µF cm^{-2}). Mercury has very smooth surface where true surface area coincides with the geometric area of the electrode and has well-pronounced surface area compared to the other solid surfaces. Table 4.5 summarizes the roughness factor for each oxide.

a)

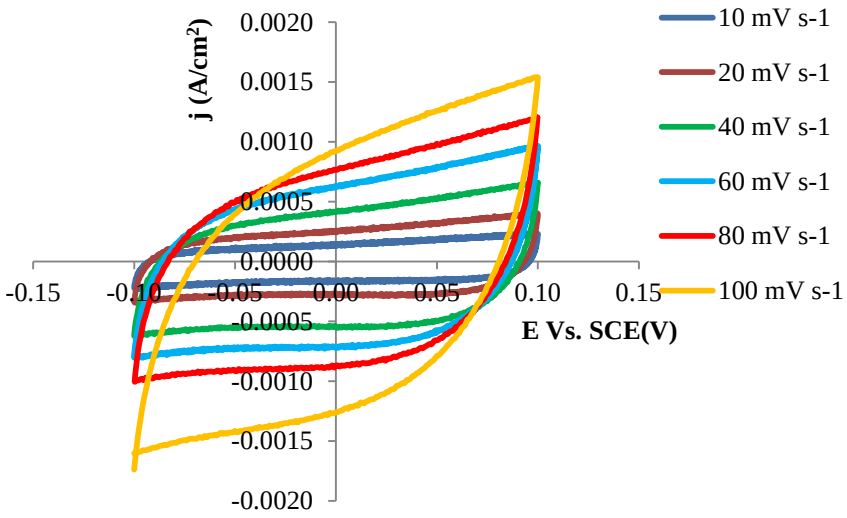

b)

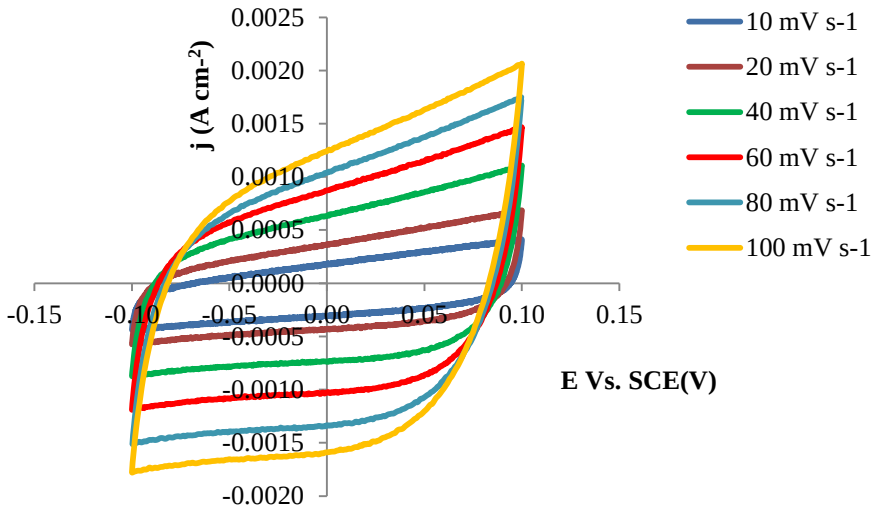
0.0025
0.0020
0.0015
0.0010
0.0005
0.0000
-0.0005
-0.0010
-0.0015
-0.0020
j (A cm-2)
-0.15
-0.10
-0.05
0.00
0.05
0.10
0.15
E Vs. SCE(V)
10 mV s-1
20 mV s-1
40 mV s-1
60 mV s-1
80 mV s-1
100 mV s-1

c)

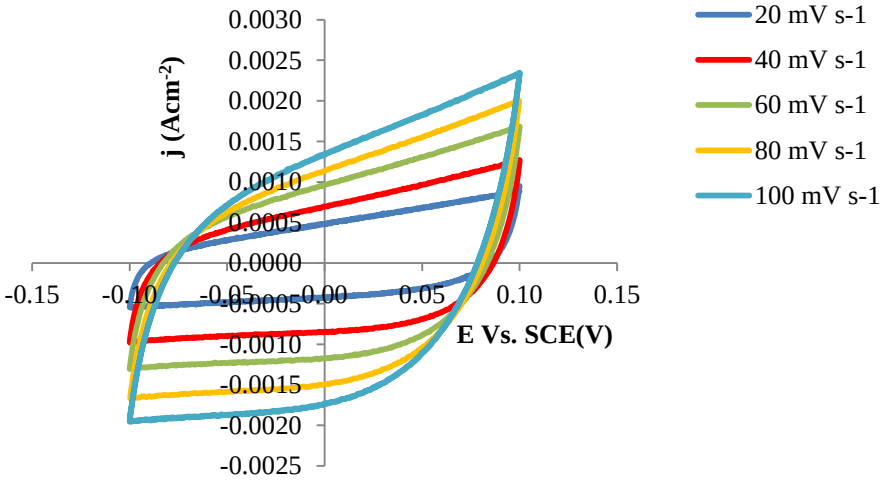
0.0030
0.0025
0.0020
0.0015
0.0010
0.0005
0.0000
-0.0005
-0.0010
-0.0015
-0.0020
-0.0025
j (Acm-2)
-0.15
-0.10
-0.05
0.00
0.05
0.10
0.15
E Vs. SCE(V)
20 mV s-1
40 mV s-1
60 mV s-1
80 mV s-1
100 mV s-1

d)

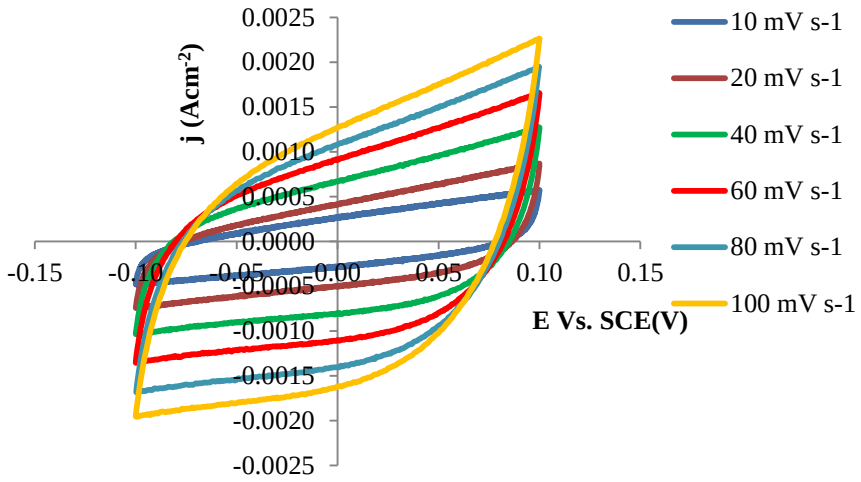

e)

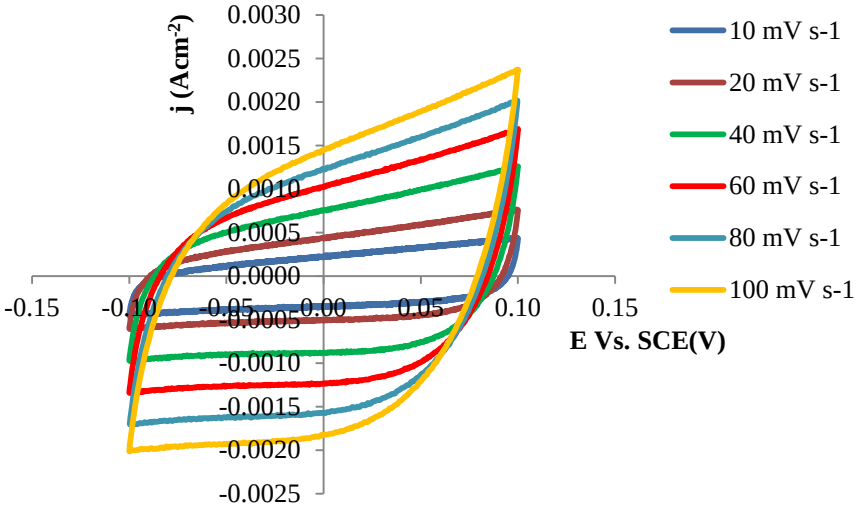

Fig. 4.8: Cyclic voltammograms of the a) Co_3O_4, b) $Cu_{0.25}Co_{2.75}O_4$, c) $Cu_{0.5}Co_{2.5}O_4$, d) $Cu_{0.75}Co_{2.25}O_4$, and e) $CuCo_2O_4$ electrodes in 1M KOH for scans recorded in a potential range of -0.100 mV to 100 mV (SCE) at various sweep rates.

a)

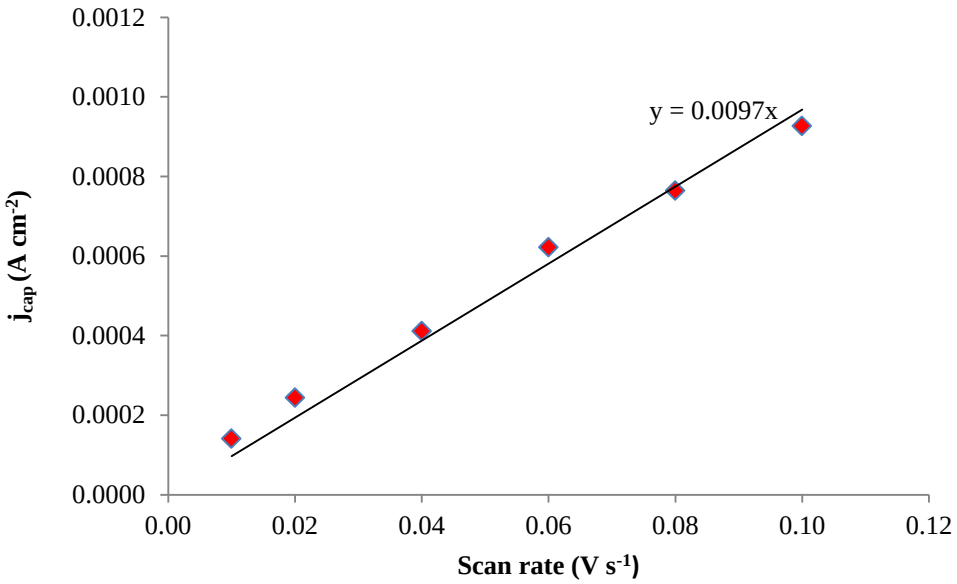
0.0012
0.0010
0.0008
0.0006
0.0004
0.0002
0.0000
0.00
0.02
0.04
0.06
0.08
0.10
0.12
y = 0.0097x
j_cap (A cm^-2)
Scan rate (V s^-1)

b)

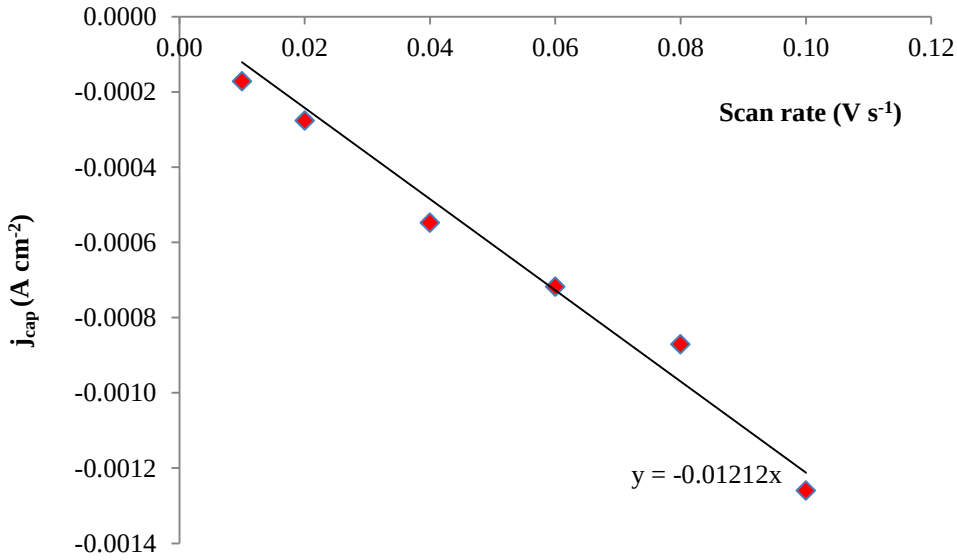
0.0000
-0.0002
-0.0004
-0.0006
-0.0008
-0.0010
-0.0012
-0.0014
0.00
0.02
0.04
0.06
0.08
0.10
0.12
Scan rate (V s^-1)
y = -0.01212x
j_cap (A cm^-2)

c)

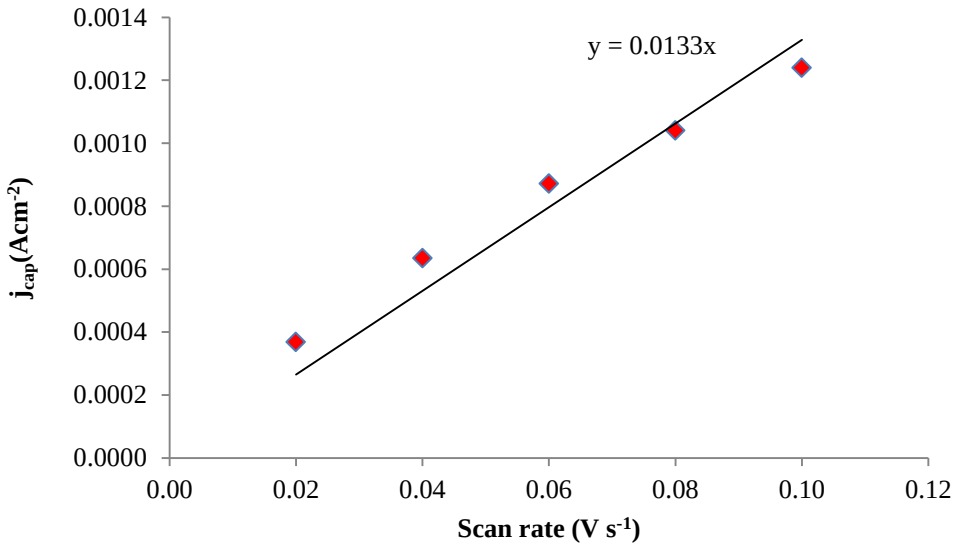
y = 0.0133x
0.0014
0.0012
0.0010
0.0008
0.0006
0.0004
0.0002
0.0000
0.00
0.02
0.04
0.06
0.08
0.10
0.12
jcap(Acm-2)
Scan rate (V s-1)

d)

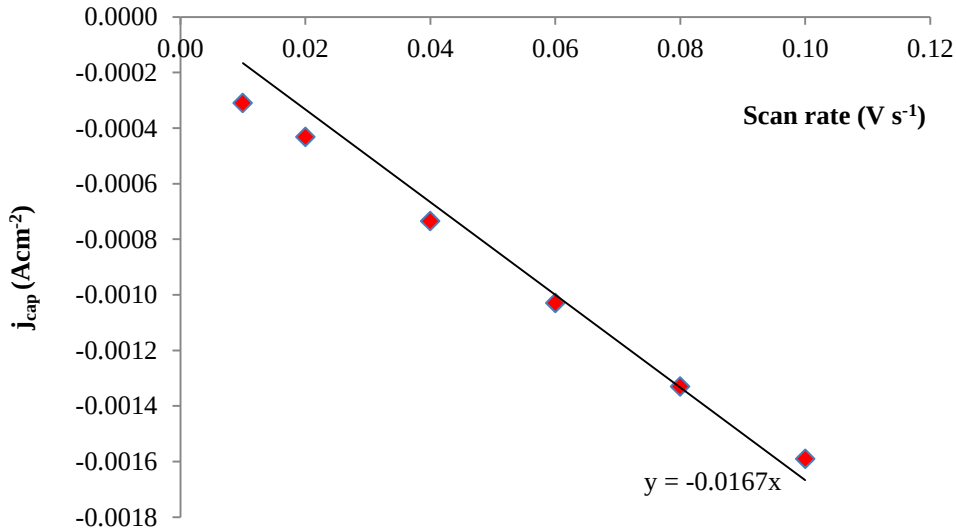
0.0000
0.00
0.02
0.04
0.06
0.08
0.10
0.12
-0.0002
-0.0004
-0.0006
-0.0008
-0.0010
-0.0012
-0.0014
-0.0016
-0.0018
Scan rate (V s-1)
jcap (Acm-2)
y = -0.0167x

e)

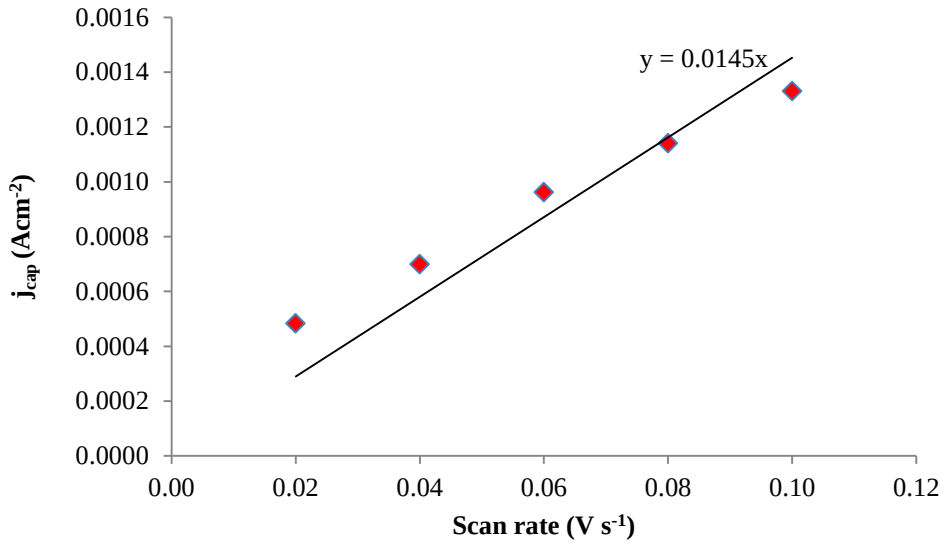
y = 0.0145x
0.0016
0.0014
0.0012
0.0010
0.0008
0.0006
0.0004
0.0002
0.0000
0.00
0.02
0.04
0.06
0.08
0.10
0.12
j_{cap} (Acm^{-2})
Scan rate (V s^{-1})

f)

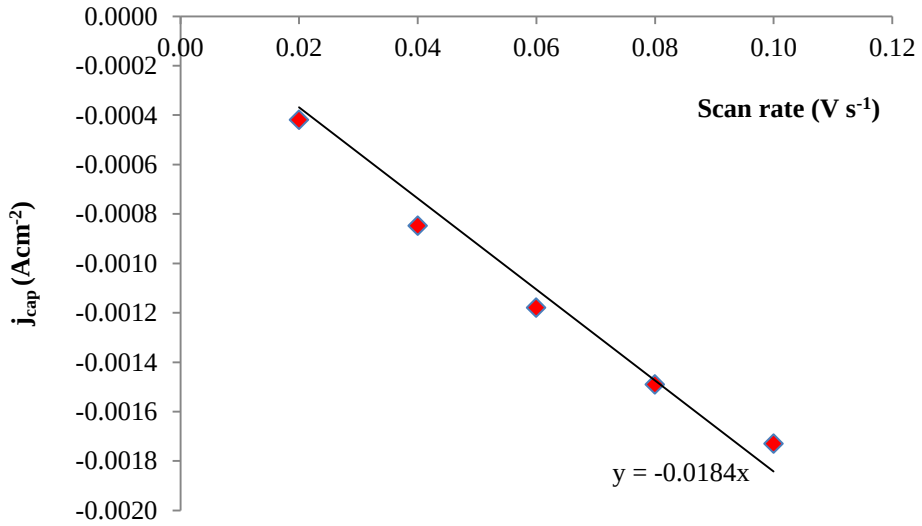
0.0000
-0.0002
-0.0004
-0.0006
-0.0008
-0.0010
-0.0012
-0.0014
-0.0016
-0.0018
-0.0020
0.00
0.02
0.04
0.06
0.08
0.10
0.12
Scan rate (V s^{-1})
j_{cap} (Acm^{-2})
y = -0.0184x

g)

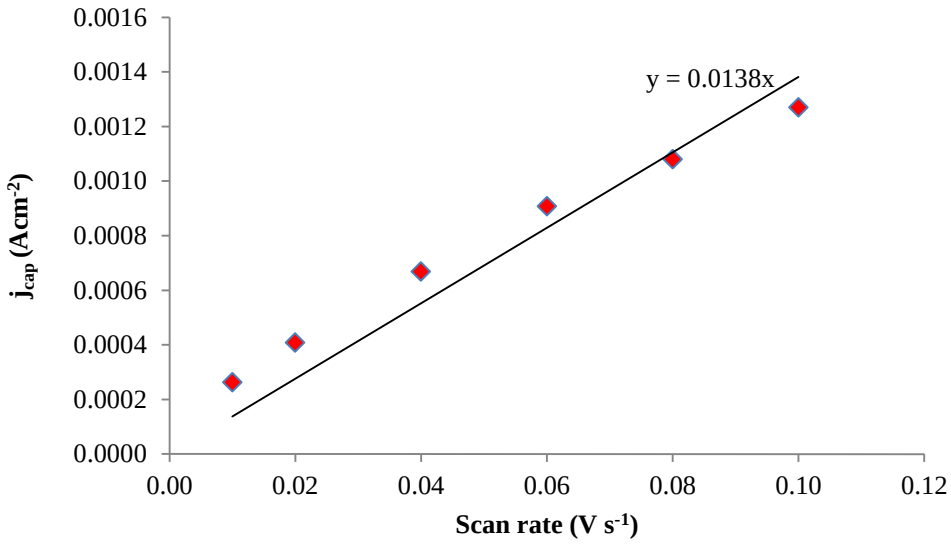
0.0016
0.0014
0.0012
0.0010
0.0008
0.0006
0.0004
0.0002
0.0000
y = 0.0138x
j_{cap} (Acm^{-2})
0.00
0.02
0.04
0.06
0.08
0.10
0.12
Scan rate (V s^{-1})

h)

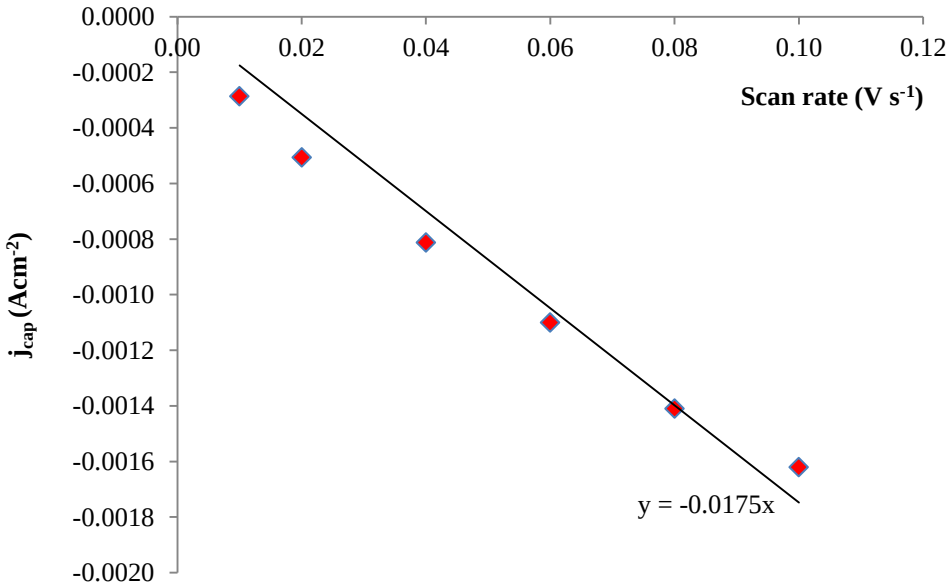
0.0000
-0.0002
-0.0004
-0.0006
-0.0008
-0.0010
-0.0012
-0.0014
-0.0016
-0.0018
-0.0020
j_{cap} (Acm^{-2})
0.00
0.02
0.04
0.06
0.08
0.10
0.12
Scan rate (V s^{-1})
y = -0.0175x

i)

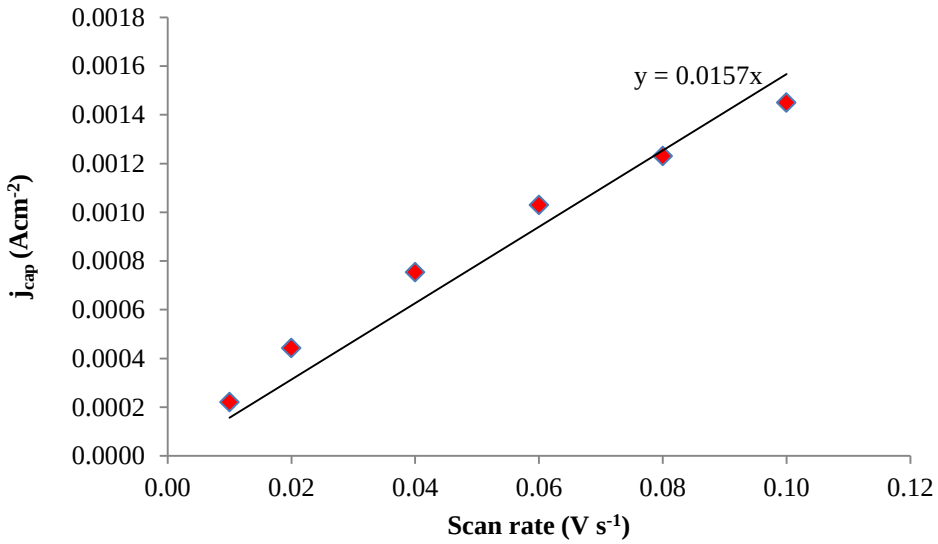

j)

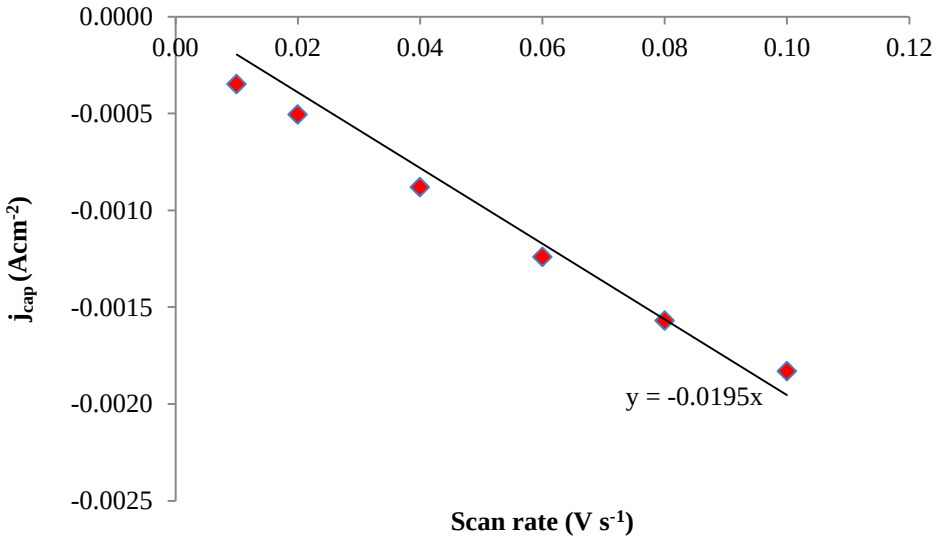

Fig. 4.9: Plot of the double layer charging current density vs. scan rate for the a) and b) Co_3O_4, c) and d) $Cu_{0.25}Co_{2.75}O_4$, e) and f) $Cu_{0.5}Co_{2.5}O_4$, g and h) $Cu_{0.75}Co_{2.25}O_4$, and i) and j) $CuCo_2O_4$ electrodes prepared by thermal decomposition method.

Table 4.5: Roughness factor of $Cu_xCo_{3-x}O_4$ prepared by thermal decomposition method

Composition	Film loading (mg cm^{-2})	Roughness factor (R_F)	Relative error (%)
Co_3O_4	0.7	182 ± 30	17
$Cu_{0.25}Co_{2.75}O_4$	0.6	250 ± 41	16
$Cu_{0.5}Co_{2.5}O_4$	0.9	275 ± 47	16
$Cu_{0.75}Co_{2.25}O_4$	0.6	261 ± 45	16
$CuCo_2O_4$	0.5	293 ± 46	16

From these measurements one can see that the introduction of copper into the cobalt spinel lattice increased the roughness of spinel oxide; Co_3O_4 having the lowest and $CuCo_2O_4$ possessing the highest roughness values. Marsan *et al.* have obtained a high roughness factor of 1400 with a catalyst loading of 3.3 mg cm^{-2} for $CuCo_2O_4$, prepared by thermal decomposition method [37]. Chartier *et al.* have observed an increased roughness factor with substitution of Nickel [44]. Again, this agrees with the work of J.P.Pandey *et al.*, who observed a high roughness factor for $M_xCo_{3-x}O_4$ (M = Ni, Cu) using the sol gel method [48].

The error in the roughness factor was estimated using the following equation:

$$\Delta R_f = R_f\,(\Delta \text{Slope} / \text{slope} + \Delta C_{dl}\,\text{smooth surface} / C_{dl}\,\text{smooth surface}) \qquad (4.1)$$

Where the error in the slope ((ΔSlope) is determined by calculating the standard deviation of anodic and cathodic slopes. The double layer capacitance of smooth surface (ΔC_{dl} smooth surface) is assumed to have a relative error of 5%. The absolute error of the samples prepared by

thermal decomposition method ranges from 30 – 47 and no significant difference in their relative error is observed, which varies from 16 – 17%.

4.4.2. Oxygen evolution reaction at $Cu_xCo_{3-x}O_4$ electrodes

Following the roughness characterization, the electrochemical characteristics of the films were studied. In order to study the oxygen evolution reaction at $Cu_xCo_{3-x}O_4$, cyclic voltammetry was carried out for the electrodes prepared by thermal decomposition method. Cyclic voltammograms were obtained for Co_3O_4, $Cu_{0.25}Co_{2.75}O_4$, $Cu_{0.5}Co_{2.5}O_4$, $Cu_{0.75}Co_{2.25}O_4$ and $CuCo_2O_4$ between a potential range of -0.8 V - 1.0 V at a scan rate of 50 mV s^{-1}, are shown in the Fig. 4.10. These cyclic voltammograms of $Cu_xCo_{3-x}O_4$ electrodes possessed the characteristic current response as a function of the applied potential. Each voltammogram has an anodic peak and a corresponding cathodic peak at the positive potential regions. These peaks are observed approximately at the same potentials, regardless of the copper content in the film. The values of anodic potential (E_p^a), cathodic potential (E_p^c) and redox potential ($E_p = (E_p^a + E_p^c)/2$) are summarised in the Table 6. These characteristic redox couples are assigned to Co (III)/Co (IV) surface transition according to the reaction [16, 19, 20]

$$CoOOH + OH^- \rightleftharpoons CoO_2 + H_2O + e^- \quad (4.2)$$

$Cu_{0.75}Co_{2.25}O_4$ has achieved the lowest redox potential compared to other compositions. Chi *et al.* reported similar features in their cyclic voltammograms (E_p = 0.38 V (SCE), for the materials prepared by the co-precipitation method [45]. R.N.Singh *et al.* obtained a redox potential of 276 mV (SCE) for $NiCo_2O_4$ prepared by spray pyrolysis [44]. Pourbaix diagram also indicates the presence of the redox couple CoO_2/ CoOOH, in this potential range at a pH of 13.8 [67].

In order to identify the exact nature of the species involved in this process, Marsan *et al.* carried out cyclic voltammetry on thin colloidal films of $Co(OH)_2$ between a potential range of -0.10 V and 0.50 V versus SCE in 1M KOH. Two anodic peaks, A_1 at 0.44 V and A_2 at 0.11 V and corresponding cathodic peaks, C_1 at 0.40 V and C_2 at 0.10 V were obtained. Later peaks are associated with Co(III)/Co(II) transition, were absent in this work. The peaks A_1/ C_1 with an equilibrium potential of 0.425V (SCE) were assigned to Co (III) /Co (IV) surface transition [68].

At the negative potential range, the cyclic voltammograms of copper-containing electrodes possessed an anodic peak, which is absent in Co_3O_4. This peak could be associated with the Cu^{I}/ Cu^{II} transition process. Marsan et al. also obtained a similar anodic peak for $CuCo_2O_4$ prepared by thermal decomposition method and this peak was assigned to Cu^{I}/ Cu^{II} transition [66].

$$Cu_2O + H_2O + 2OH^- \rightarrow 2Cu(OH)_2 + 2e^- \quad (4.3)$$

The cyclic voltammogram obtained from $Cu(OH)_2$/Pt vs Hg/HgO, in the negative potential region also indicates a redox transition corresponding to Cu^{11}/Cu^{1} [66].

As $Cu_xCo_{3-x}O_4$ electrodes with x value ranging from 0 to 1 exhibit a cathodic peak at the negative potential region, the presence of this peak could be due to the oxygen reduction reaction.

a)

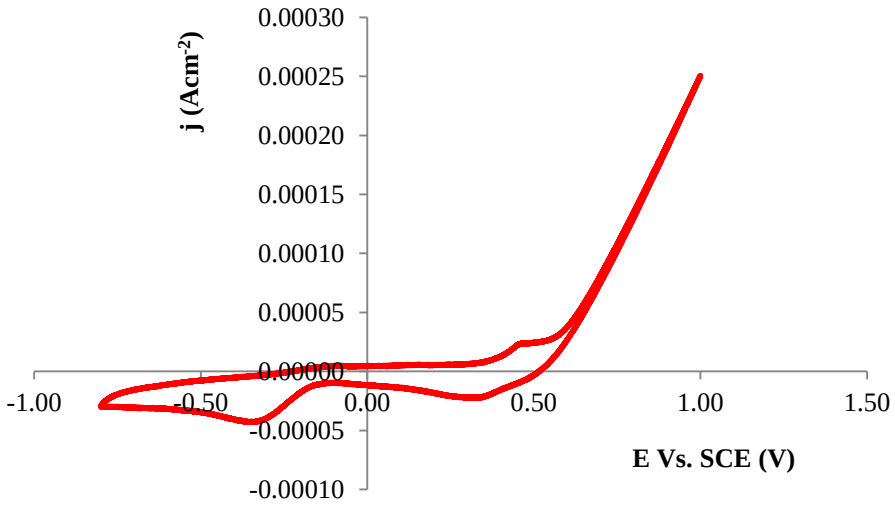
0.00030
0.00025
0.00020
0.00015
0.00010
0.00005
0.00000
-0.00005
-0.00010
j (Acm-2)
-1.00
-0.50
0.00
0.50
1.00
1.50
E Vs. SCE (V)

b)

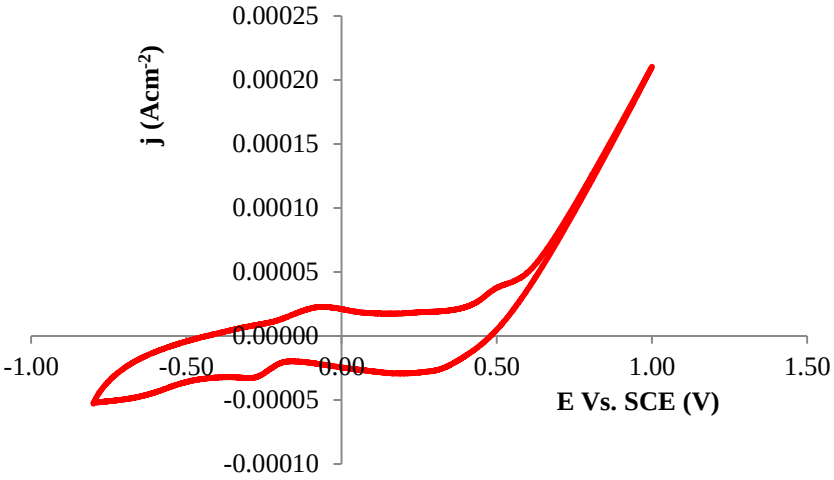
0.00025
0.00020
0.00015
0.00010
0.00005
0.00000
-0.00005
-0.00010
j (Acm-2)
-1.00
-0.50
0.00
0.50
1.00
1.50
E Vs. SCE (V)

c)

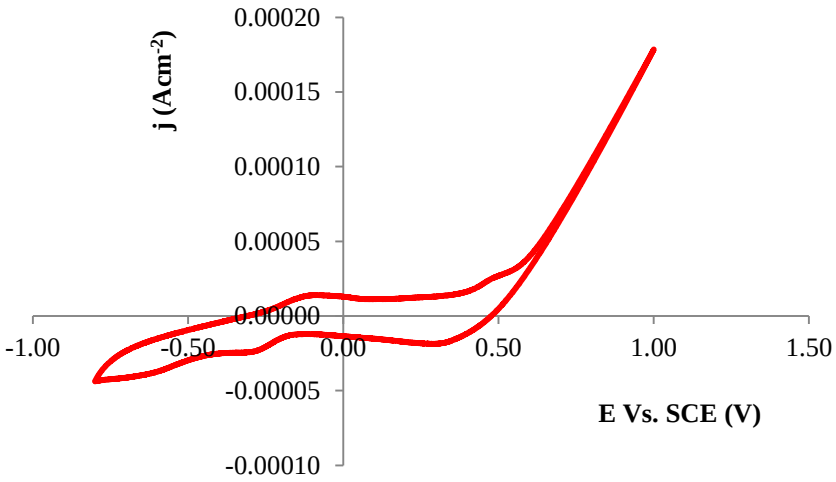
0.00020
0.00015
0.00010
0.00005
0.00000
-0.00005
-0.00010
j (Acm-2)
-1.00
-0.50
0.00
0.50
1.00
1.50
E Vs. SCE (V)

d)

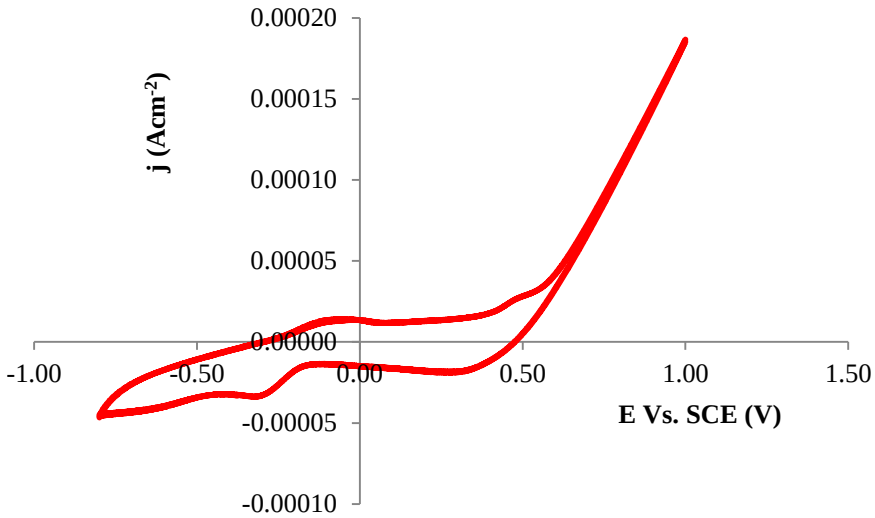
0.00020
0.00015
0.00010
0.00005
0.00000
-0.00005
-0.00010
j (Acm-2)
-1.00
-0.50
0.00
0.50
1.00
1.50
E Vs. SCE (V)

e)

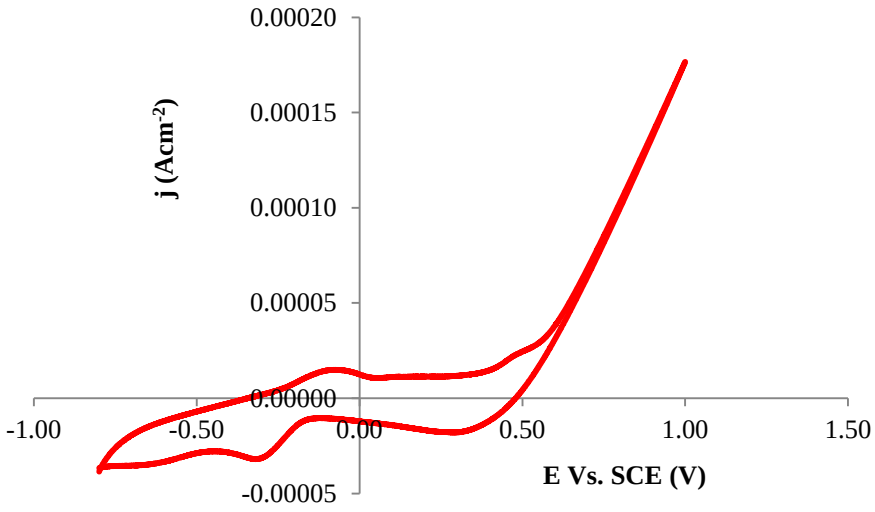

Fig. 4.10: Cyclic voltammograms of a) Co_3O_4, b) $Cu_{0.25}Co_{2.75}O_4$, c) $Cu_{0.5}Co_{2.5}O_4$, d) $Cu_{0.75}Co_{2.25}O_4$, and e) $CuCo_2O_4$ electrodes (prepared by thermal decomposition method) corrected for their real surface area using the roughness factor reported in section 4.4.1. Cyclic voltammograms were recorded in 1M KOH at a scan rate of 50 mV s^{-1}.

Table 4.6: The redox potential of $Cu_xCo_{3-x}O_4$ prepared by thermal decomposition method

Samples	E_p^a [SCE(V)]	E_p^c [SCE(V)]	$(E_p^a + E_p^c)/2$ [SCE(V)]
Co_3O_4	0.457 ± 0.052	0.326 ± 0.004	0.392 ± 0.027
$Cu_{0.25}Co_{2.75}O_4$	0.521 ± 0.013	0.224 ± 0.006	0.372 ± 0.010
$Cu_{0.5}Co_{2.5}O_4$	0.466 ± 0.044	0.298 ± 0.075	0.382 ± 0.020
$Cu_{0.75}Co_{2.25}O_4$	0.439 ± 0.042	0.295 ± 0.009	0.367 ± 0.022
$CuCo_2O_4$	0.496 ± 0.040	0.280 ± 0.024	0.388 ± 0.004

The standard reduction potential of the O_2/H_2O couple in alkaline medium is 0.401 V vs. NHE (0.159 V vs. SCE) [1]. This thermodynamic potential seldom achieves in practice and the oxygen evolution reaction is always accompanied by a high overpotential. The onset potential and overpotential of the $Cu_xCo_{3-x}O_4$ electrodes for oxygen evolution reaction is summarised in the Table 4.7. The Co_3O_4 possesses a higher overpotential for the oxygen evolution reaction (0.405V vs SCE). As the copper content increased in the cobalt spinel lattice, the overpotential decreased and $Cu_{0.75}Co_{2.25}O_4$ achieved a lowest overpotential of 0.354V vs SCE. This could be associated with the increased roughness factor of copper containing electrodes. As the surface area increases more active sites are available for oxygen evolution reaction and hence overpotential decreases. Thus the addition of copper improves the geometric properties of the sample. However, this potential is higher compared to the overpotential of OER on RuO_2 (0.25V). $CuCo_2O_4$ exhibits a higher overpotential even though it possesses the highest roughness factor, this might be due to the presence of resistive phase CuO in the spinel lattice of $CuCo_2O_4$.

The error calculation for all electrochemical measurements was obtained by the standard deviation of two set of experimental values.

Table 4.7: The onset potential and overpotential of $Cu_xCo_{3-x}O_4$ electrodes for OER, prepared by thermal decomposition method

Composition	Onset potential[SCE(V)]	Overpotential [SCE(V)]
Co_3O_4	0.564 ± 0.041	0.405 ± 0.053
$Cu_{0.25}Co_{2.75}O_4$	0.539 ± 0.003	0.380 ± 0.004
$Cu_{0.5}Co_{2.5}O_4$	0.531 ± 0.003	0.372 ± 0.003
$Cu_{0.75}Co_{2.25}O_4$	0.513 ± 0.009	0.354 ± 0.009
$CuCo_2O_4$	0.522 ± 0.001	0.363 ± 0.001

In order to compare the true electrocatalytic activity of $Cu_xCo_{3-x}O_4$ electrodes for oxygen evolution reaction, the charging current density in the potential range of -0.8 V – 1 V has been normalized to unit real surface area (Fig. 4.11). As shown in figure, the slope of the oxygen evolution reaction decreases with increase of x value in $Cu_xCo_{3-x}O_4$. At a given potential, Co_3O_4 has achieved a higher current density and this current density was found to decrease with the addition of copper. This indicates that cobalt sites are active for the oxygen evolution reaction. The copper substitution decreases the number of active cobalt sites in the spinel lattice and hence the current density decreases. R.N.Singh *et al.* observed a decrease in true catalytic activity for oxygen evolution reaction when the cobalt is replaced with Ni and Cu in Co_3O_4 [38].

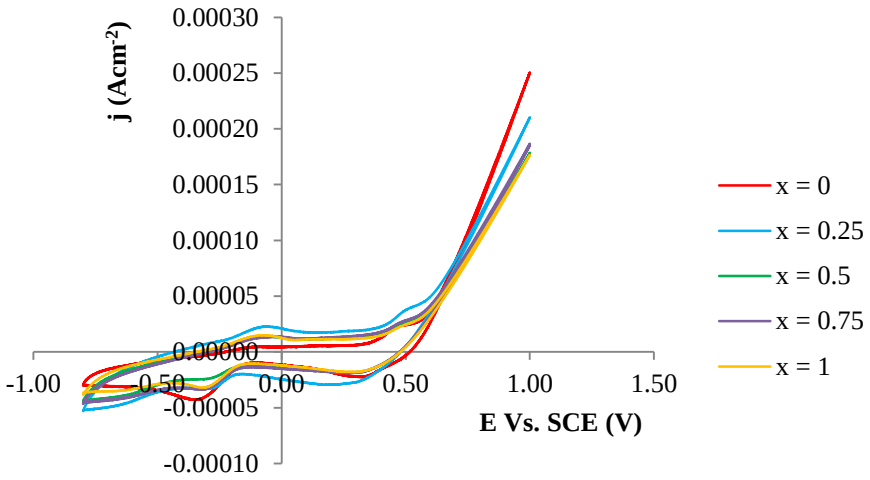

Fig. 4.11: Cyclic voltammograms of $Cu_xCo_{3-x}O_4$ corrected for the real surface area of electrodes using the roughness factor reported in section 4.4.1.

4.4.3. Electroreduction of hydrogen peroxide

The catalytic property of the $Cu_xCo_{3-x}O_4$ electrodes, prepared by thermal decomposition method was analyzed by the electroreduction of hydrogen peroxide. The cyclic voltammograms of the electrodes were recorded in 3M NaOH containing 0.6 M hydrogen peroxide at a scan rate of 5 mV s^{-1}. The cyclic voltammograms, corrected for the real surface area are shown in the figure 4.12 a. The current increased linearly with increase of the potential in the negative going scan. The cathodic current was generated by the electroreduction of the hydrogen peroxide. The onset potential for hydrogen peroxide reduction as well as the potential, at which maximum current density generated is listed in the Table 4.8.

Co_3O_4 electrode achieved the lowest onset potential (-0.152 V) and obtained a maximum current density of $-1.25*10^{-4}$ A cm^{-2} at a potential of -0.46 V. $Cu_{0.25}Co_{2.75}O_4$ also achieved a high current density of -1.23×10^{-4} A cm^{-2} at a potential of -0.48 V, however the onset potential (-0.176 V) is higher compared to the onset potential of Co_3O_4. Further addition of copper resulted in the lowering of current density. $CuCo_2O_4$ recorded the lowest current density of -0.531 A cm^{-2} at a potential of -0.371 V. As shown in figure 4.12 a, at a given potential, Co_3O_4 exhibits the highest current density compared to other copper substituted electrodes. Thus, the true catalytic activity was found to decrease with the copper substitution. The oxygen evolution was observed in the anodic reaction as shown in the Figure 4.12 b.

According to Honda *et al.* the following mechanism is expected to occur during the electroreduction of H_2O_2 on Ag in alkaline solution [69].

Hydrogen peroxide dissociates partly in the alkaline solution as,

$$H_2O_2 + OH^- \rightleftharpoons HO_2^- + H_2O \quad (4.4)$$

HO_2^{-1} takes part in the anodic reaction and H_2O_2 takes part in the cathodic reaction by the following mechanisms.

Anodic reaction: $HO_2^- + OH^- \rightarrow O_2 + H_2O + 2e^-$ (4.5)

Cathodic reaction: $H_2O_2 + 2e^- \rightarrow 2OH^-$ (4.6)

Table 4.8: The onset potential and the maximum current density obtained during the electroreduction of $Cu_xCo_{3-x}O_4$ (CVs are shown in Fig. 4.12)

Composition	Onset potential [SCE (V)]	Potential [SCE(V)]	Current density (A cm^{-2})(10^{-4})
Co_3O_4	-0.152 ± 0.011	-0.46 ± 0.05	-1.250 ± 0.001
$Cu_{0.25}Co_{2.75}O_4$	-0.176 ± 0.001	-0.48 ± 0.05	-1.23 ± 0.01
$Cu_{0.5}Co_{2.5}O_4$	-0.187 ± 0.002	-0.37 ± 0.11	-0.783 ± 0.001
$Cu_{0.75}Co_{2.25}O_4$	-0.174 ± 0.006	-0.361± 0.067	-0.650 ± 0.001
$CuCo_2O_4$	-0.176 ± 0.004	-0.371± 0.122	-0.531 ± 0.001

a)

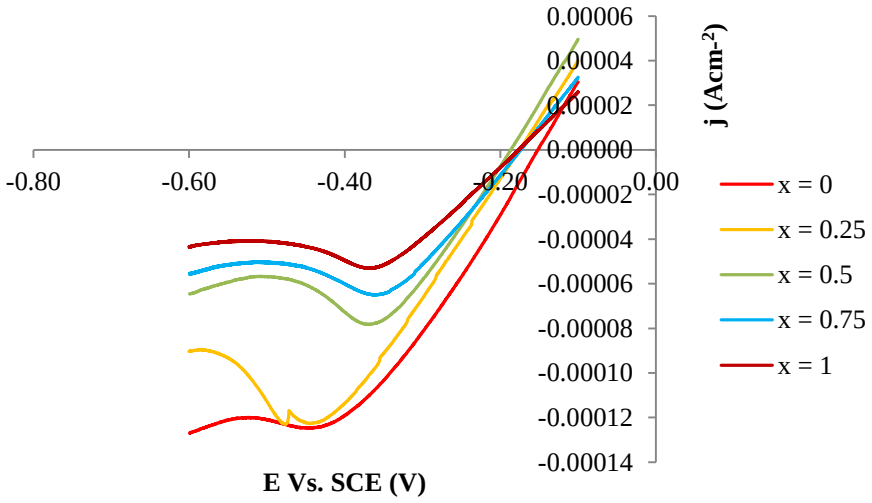

b)

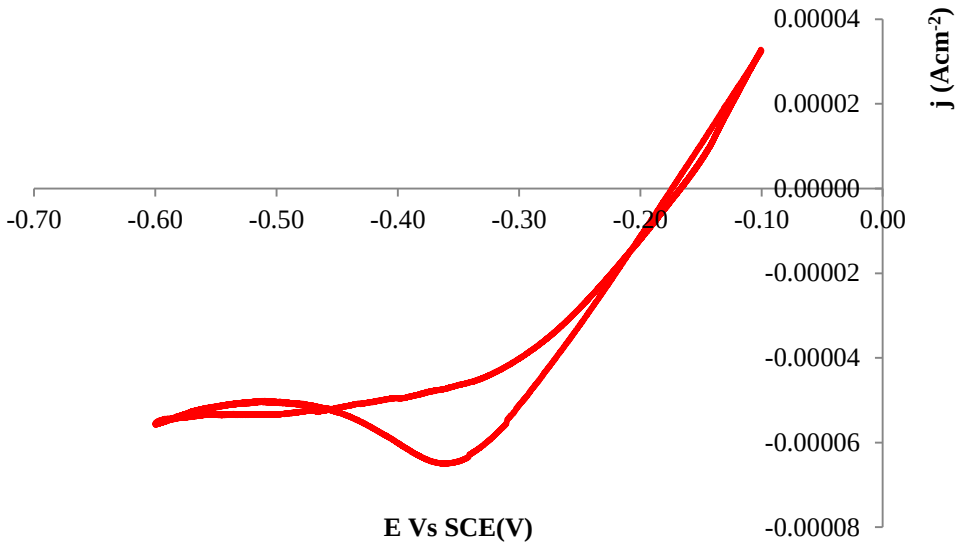

Fig. 4.12: a) Cyclic voltammogram of the electroreduction of H_2O_2 using $Cu_xCo_{3-x}O_4$ films prepared by thermal decomposition method, and b) cyclic voltammogram of $Cu_{0.75}Co_{2.25}O_4$. The solution was a 3 M NaOH solution containing 0.6M H_2O_2 and the sweep rate was 5 mV s^{-1}.

Chapter 5: conclusion and future work

5.1. Conclusion

In order to optimize a suitable electrode material for the oxygen evolution reaction, copper cobalt oxide spinels of various compositions ($Cu_xCo_{3-x}O_4$) with x value ranging from 0 to 1 have been prepared. Two methods have been used for the preparation of spinel cobaltites: the thermal decomposition method and the co-precipitation method. The morphology of the prepared materials was analyzed by scanning electron microscopy (SEM) and elemental analysis was done by energy dispersive X-ray spectroscopy (EDX). The structure analysis was performed by X-ray diffraction (XRD) and electrochemical experiments were carried out using cyclic voltammetry (CV).

The SEM analysis of the $Cu_xCo_{3-x}O_4$, prepared by the co-precipitation method shows that the material is highly porous, and the morphology is relatively identical for all of the compositions irrespective of copper content. Whereas the electrodes prepared by thermal decomposition method indicate that the surface morphology changes with copper content and the surface gradually became more porous and homogeneous as the copper content increased. Grain size was found to decrease with copper addition; $CuCo_2O_4$ electrode surface appears to be more porous and grains are uniformly distributed.

The EDX analysis of the electrode material prepared by co-precipitation method and thermal decomposition method shows a good correlation between the stoichiometric and EDX elemental composition, even though the copper cobalt ratio is slightly high at higher x values. This is presumably related to the increased roughness factor; as the roughness factor increases

the surface becomes more porous and the EDX analysis becomes less precise. Homogeneity of the material may also cause deviation in the EDX measurements.

The X-ray diffraction pattern of Co_3O_4 prepared by the co-precipitation method confirmed the formation of cubic spinel structure. However, the XRD pattern of $Cu_{0.5}Co_{2.5}O_4$ has additional peaks from copper (II) oxide along with spinel structure. The XRD patterns of the $Cu_xCo_{3-x}O_4$ electrodes prepared by thermal decomposition method exhibit diffraction peaks corresponding to cubic spinel structure and remains monophasic spinel oxide up to an x value 0.75. Meanwhile, $CuCo_2O_4$ display peaks of CuO along with spinel structure. The lattice parameter increases with addition of copper, which indicates the incorporation of copper into the cobalt spinel lattice.

The roughness factor was calculated using cyclic voltammetry for all the electrodes prepared by thermal decomposition method. The lowest roughness value was recorded for Co_3O_4. Copper addition increased the roughness factor of the electrodes and $CuCo_2O_4$ achieved the highest roughness factor. The increase in roughness value could be related to the decrease in the crystallite size.

Electrocatalytic activity for oxygen evolution reaction was analyzed for the electrodes prepared by the thermal decomposition method, by performing cyclic voltammetry. Cyclic voltammograms were obtained between the potential ranges of -0.8 V - 1.0 V in 1M KOH, at a scan rate of 50 mV sec^{-1}. Co_3O_4 exhibited the highest overpotential for the oxygen evolution reaction. This could be due to Co_3O_4 having the lowest roughness factor. As the amount of copper increased in the spinel lattice, the overpotential was found to decrease. This might be due to the increased roughness factor or surface area. As the surface area increases, more active

sites are available for oxygen evolution reaction and hence the overpotetial of OER decreases. $Cu_{0.75}Co_{2.25}O_4$ possessed the lowest overpotential, further addition of copper resulted in the higher overpotential and this could be related to the formation of CuO, a resistive phase in the spinel lattice.

In order to compare the true electrocatalytic activity of $Cu_xCo_{3-x}O_4$ at various compositions, the cyclic voltammograms were obtained with charging current density per unit real surface area. As the copper content increased in the spinel lattice, the slope of the oxygen evolution reaction decreased. At a given potential, Co_3O_4 possessed a maximum current density. This indicates that cobalt sites are active for oxygen evolution reaction and substitution of copper decreases the number of cobalt sites and hence the current density. So the effect of copper addition is to increase the surface area by decreasing the crystallite size of the particles and thus improve the geometric property of the electrode surface; hence the catalytic activity.

Cyclic voltammetry has been used to study the catalytic activity of $Cu_xCo_{3-x}O_4$ electrodes for the electroreduction of hydrogen peroxide in 3M NaOH, containing 0.6M hydrogen peroxide at a scan rate of 5 mV s^{-1}. Cyclic voltammograms per unit real surface area shows that all the electrodes prepared by thermal decomposition method have shown activity towards the electroreduction of H_2O_2. Co_3O_4 has achieved the lowest onsetpotential of -0.152 V and obtained a maximum current density of ca. -1.25 x 10^{-4}A cm^{-2} at -0.460 V. The current density decreased with further addition of copper. At a given potential, Co_3O_4 has achieved the highest current density compared to other compositions. Thus Co_3O_4 acts as a true catalyst for both oxygen evolution reaction as well as H_2O_2 reduction reaction.

5.2. Future work

Thickness of the film has influence on surface morphology and hence roughness factor. This will change the catalytic activity of the electrode. Hence the effect of thickness of the $Cu_xCo_{3-x}O_4$ films for the oxygen evolution reaction and electroreduction of hydrogen peroxide will be studied.

Dye sensitized solar cell (DSSC) will be fabricated using $Cu_xCo_{3-x}O_4$ thin films as counter electrode. Platinum is the most commonly used counter electrode, which is an expensive part of a dye sensitized solar cell. Counter electrode need to possess high catalytic activity for efficient charge transport. We have used oxygen evolution reaction and electroreduction of hydrogen peroxide as model reactions to study the catalytic activity of the $Cu_xCo_{3-x}O_4$ thin films.

Our studies show that $Cu_xCo_{3-x}O_4$ electrodes exhibit good catalytic activity for both oxygen evolution and hydrogen peroxide reaction and hence would be a suitable electrode for DSSC.

The double layer capacitance (C_{dl}) of oxide/KOH solution interface and oxide surface roughness will be determined by impedance measurements and will compare to cyclic voltammetric results. Also electrochemical studies such as oxygen evolution and electroreduction of hydrogen peroxide will be carried out on the electrodes prepared by co-precipitation method.

References

1. Bard A.J.; Faulkner L.R. *Eletcrochemical methods-Fundamentals and applications, 2nd ed.*; New York,2001.
2. O'Sullivan, E.J.M.; Calvo E.J.; Compton R.G. *Electrode Kinetic Reactions* (online); New York, 1987, p. 274. http://books.google.ca/books?id=VVr9Rp-uhcIC&pg=PA247&lpg=PA247&dq=electrode+kinetic+by+sullivan&source=bl&ots=rx8qfvaD1u&sig=wAohmprVMIM4KQL3Gj5vmPntNig&hl=en&sa=X&ei=KjGSU9CTNYOhyAStpYHIBg&ved=0CC0Q6AEwAg%20-%20v=onepage&q=electrode%20kinetic%20by%20sullivan&f=false#v=snippet&q=electrode%20kinetic%20by%20sullivan&f=false (accessed on Jan 14, 2014)
3. Veziroglu, T.N., *Int.J.Hydroen Energy*. **1987,** *12*, 99-129
4. Trasatti, S. J. *Electrochim. Acta.* **1984,** *29*, 1503.
5. Trasatti, S. J. *Electrochim. Acta.* **2000,** *45***,** 2377-2385.
6. Matsumoto, Y.; Sato, E. J. *Mat. Chem. Phy.* **1986,** *14*, 397- 426.
7. Jackie, Y. *Nanostructured materials* [Online}; Academic Press, 2001, Chapter 1. https://books.google.ca/books?id=_pbtbJwkj5YC&pg=PR4&lpg=PR4&dq=Jackie,+Y.,+%E2%80%99Nanostructured+materials,+2001&source=bl&ots=fWNC6TI7Ai&sig=hA4q-q7sc0GfIFd5gnro8WUPvvE&hl=en&sa=X&ved=0CCwQ6AEwAmoVChMI2LeGzpWTxwIVSj4-Ch2JNgxr#v=onepage&q=Jackie%2C%20Y.%2C%20%E2%80%99Nanostructured%20materials%2C%202001&f=false

8. Trasatti, S. Interfacial Electrochemistry of Conductive Oxides for Electrocatalysis. In *Interfacial electrochemistry: Theory, Experiment and Applications*; Wieckowski Ed; New York, 1999.

9. Kim, K. J.; Park, Y. R. J. *Solid state commun.* **2003,** *127*, 25-28.

10. Joshi, S. G.; Kulkarni, D. K.; Khandekar, P.V. J. *Bull.Mater.Sci.* **1982,** *4*, 455-459.

11. Hamdani, M.; Singh, R. N.; Chartier, P. *Int. J. Electrochem. Sci.* **2010,** *5*, 556-577.

12. Tavares, A. C.; Cartaxo, M. A. M.; da Silva Pereira, M. I.; Costa F. M. J. *Electroanal. Chem.* **1999,** *464*, 187-197.

13. Jia, Jingshu.; Li, Xinyong.; Chen, Guohua. J. *Electrochim. Acta.* **2010,** *55*, 8197-8206.

14. Trasatti, S.; Lodi.G. *Electrodes of Conductive Metallic Oxides,* Part A-B; Elsevier Science Publishers: Amsterdam, The Netherlands, 1980/1981.

15. Nikolov, I.; Darkaoui, R.; Zhecheva, E.; Stoyanova, R.; Dimitrov, N.; Vitanov, T. J. *Electroanal. Chem.* **1997,** *429*, 157-168.

16. Rosa-Toro, La; Berenguer, R.; Quijada, C.; Montilla, F.; Morallon, E.; Vazquez, J. L. J. *Phys. Chem.* **2006**, *110*, 24021.

17. Miley, G.H.; Luo, N.; Mather, J.; Burton, R.; Hawkins, G.; Gu, L.; Byrd, E.; Gimlin, R.; Shrestha, P. J.; Benavides, G.; Laystrom, J.; Carroll, D. J. *Power Sources.* **2007,** *165*, 509–516.

18. Choudhury, N.A.; Raman, R. K.; Sampath, S.; Shukla, A. K. J. *Power Sources,* **2005,** *143*, 1–8.

19. Hasvold, O.; Johansen, K.H.; Mollestad, O.; Forseth, S.; Storkersen, N. J. *Power Sources.* **1999**, *80*, 254–260.

20. Scholz, F., Pickett, C.J.; Inorganic electrochemistry:2006

21. Gu, L.; Luo, N.; Miley, G.H. J. *Power Sources.* **2007,** *173*, 77–85.

22. Yang, W.; Yang, S.; Sun, W.; Sun, G.; Xin, Q. *J. Electrochim. Acta.* **2006**, *52*, 9–14.

23. Chen, W.; Sun, G.; Liang, Z.; Mao, Q.; Li, H.; Wang, G.; Xin, Q.; Chang, H.; Pak, C.; *Seung*, D. *J. Power Sources.* **2006**, *160*, 933–939.

24. Bidault, F.; Brett, D. J. L.; Middleton, P. H.; Brandon, N. P. *J. Power Sources.* **2009**, *187*, 39–48.

25. Raman, R.K.; Prashant, S.K.; Shukla, A.K. *J. Power Sources.* **2006**, *162*, 1073–1076.

26. Cao, D.; Chao, J.; Sun, L.; Wang, G. *J. Power Sources.* **2008**, *179*, 87–91.

27. Jia, W.; Guo, M.; Zheng, Z.; Yu, T., Rodriguez, E. G.; Wang, Y.; Lei, Y. *J. Electroanal. Chem*. **2009,** *625*, 27–32.

28. Lee, Y., Suntivich, J., May, K. J., Perry, E. E., Shao-Horn, Y. *J. Phys. Chem. Lett*. **2012,** *3*, 399.

29. Duby, P. J. *Miner. Met. Mater. Soc*. **1993**, *45*, 41–43.

30. Beer, H.B. *J. Electrochem. Soc.* **1980,** *127*, 303C.

31. Denton, D.A. *J. Electrochim. Acta***. 1978***, 24*, 521-527.

32. Vukovic, M., *J. appl. electrochem.* **1987**, *17*, 737-745.

33. Singh, J. P.; Singh, R. N. *Indian* J. *Chem*. **2000**, *39A*, 819-825.

34. Bursell, M., Pirjamali, M., Kiros, Y. J.*Electrochim. Acta*, **2002,** *47*, 1651-1660.

35. Wattiaux, A., Grenier, J.C., Pouchard, M., Hagenrnuller, P. *This journal*, **1987**, 134, 1714

36. Prakash, J., Tryk, D., Yeager, E. *J. power sources*, **1990**, *29*, 413-422.

37. Trasatti, S. J. *Electrochim. Acta.* **1991**, *36*, 225-241.

38. Singh, J.P.; Singh, R.N. *J. New Mat. Electrochem. Systems.* **2000,** *3*, 131-139.

39. Marsan, B.; Fradette, N.; Beaudoin, G. *J. Electrochem. Soc.* **1992**, *139*, 1889.

40. Angelov, S.; Tyuliev, G.; Marinova, Ts. *Appl. Surf. Sci.* **1987**, *27*, 381-392

41. Li G. H.; Dai, L. Z.; Lu, D. S.; Peng, S.Y., J. *Solid State Chem.* **1990,** *89*, 167.

42. Baydi, M. El.; Tiwari, S. K.; Singh, R. N.; Rehspringer, J. L.; Chartier, P.; Koenig, J. F.; Poillerat, G., J. *Solid State Chem*. **1995**, *116*, 157-169.

43. Koninck, M. De.; Poirier, S. C.; Marsan, B. J. *Electrochem. Soc*. **2006,** *153*, A2103-A2110.

44. Gautier, J. L.; Trollund, E.; Rios E.; P.; Nkeng, P; Poillerat, G. J. *Electroanal. Chem.* **1997**, *428*, 47-56.

45. Patil, P. S.; Kadam, L. D.; Lokhande, C. D. *Thin Solid Films.* **1996**, *272*, 29-32.

46. Singh, R. N.; Koenig, J. F.; Poillerat, G.; Chartier, P. J. *Electrochem. Soc*. **1990**, *137*, 1408.

47. Chi, B.; Lin, H.; Li, J. *Int. J. of Hydrogen Energy*. **2008**, *33*, 4763-4768.

48. Jiang, Y.; Wu, Y.; Xie, B.; Xie, Y.; Qian, Y. *Mater. Chemistry and Physics.* **2002**, *74*, 234-237.

49. Sparatu, N.; Terashima, C.; Tokuhiro, K.; Sutanto, I.*; Tryk, D. A.; Park, S. M.; Fugishima, A.* J. *Electrochem. Soc*. **2003**, *150*, E337-E341.

50. Pandey,.J.P.; Singh, R. N.; Singh ,N. K.; Lal, B.; Chartier, P.; Koenig, J. F. J. *Electrochimica Acta*. **2000,** *45***,** 1911–1919.

51. Smart, L.; Moore E., *Solid State Chemistry – An Introduction, 2nd ed;* CRC press, Boca Raton, 2012.

52. Rao, C.N.R.; Gopalakrishnan. J.; *New Directions in Solid State Chemistry;* Cambridge University Press, New York, 1997.

53. Meng, X.; Li, H.; Chen, J.; Mei, L.; Wang, K.; Li, X. *J. Magnetism and Magnetic Materials,* **2009,** *321*, 1155-1158.

54. Rao, C. N. R.; Subba, Rao, G. V. J. phys. stat. sol. (a) **1970,** *1*, 597

55. Shannon, R. D.; Prewitt C.T.; J. *Acta Cryst.* **1969,** *B25*, 925.

56. Goldstein, J. I; Newbury, D. E; Joy, D. C; Lyman, C. E; Echlin, P.; Lifshin, E.; Sawyer, L.; Michael, J. R. *Scanning electron microscopy and X-ray microanalysis, 3rd ed.*; Kluwer Academic/Plenum Publishers: New York, 2003.

57. Leng, Y. *Materials characterization: Introduction to microscopic and spectroscopic methods*; John Wiley & Sons: Asia, 2008.

58. Cullity, B.D.; Stock, S. R.; *Elements of X-ray diffraction, 3rd ed*; Prentice hall: Upper Saddle River, 2001

59. Gosser, D. K., *Cyclic Voltammetry: Simulation and analysis of reaction mechanisms*; VCH: New York, 1993

60. Bond, A.M; *Broadening of electrochemical horizons: principles and illustrations of voltammetric and related techniques*; Oxford University Press: New York, 2002

61. Trasatti, S.; Petrii, O.A. J. *Electroanal. Chem* **1992,** *327*, 353-376

62. Levine, S., Smith, A.L., Discuss. Faraday Soc. **1971,** 52, 290

63. Devanathan, M. A., Peries, P., Trans. Faraday Soc. **1954,** 50, 1236.

64. Intech homepage. http://www.intechopen.com/books/howtoreference/biosensors-for-health-environment-and-biosecurity/biosensors-for-detection-of-low-density-lipoprotein-and-its-modified-forms (accessed May 20, 2004)

65. Goldstein, J. R.; Tseung, A.C.C. J. *Catal*, **1974**, 32,452-465.

66. Fatih, K; Marsan, B.; *Can.J.Chem.* **1997,** *75*,1597-1607.

67. Pourbaix, *M. Atlas of electrochemical equilibria in aqueous solutions*; National Association of Corrosion Engineers: Brussels, 1974.

68. Fradette, N.; Marsan, B.; J. *Electrochem. Soc.* **1998**, 145, 7, 2320

69. Honda M., Kodera T., Kita H., J.Electrochim. Acta, **1983,** 28, 5, 727

Appendix A

A1. Error Analysis

Every measurement is accompanied with a certain error or uncertainty as the measurement is limited by techniques, precision of the instrument and skill of the observer. The error calculation and analysis used in this work are given below.

A1.1 EDX error analysis

The general formula of quantitative analysis with an internal standard is expressed as

$$C_i / C_{(i)} = (Z_i A_i F_i) I_i / I_{(i)} \quad \text{(A1)}$$

where the C_i and I_i are the concentration and intensity of the internal standard of the element and $C_{(i)}$ and $I_{(i)}$ are the concentration and intensity of the element to be analyzed in a given sample, respectively. Internal standard represents a standard element of known concentration, assuming instrumental and matrix effects are similar for both standard and the sample to be analyzed. $Z_i A_i F_i$ represents the matrix factors affecting the X-ray intensity of the element i in the sample. The symbol Z represents the atomic number effect and refers to the difference in the characteristic X-ray generation due to the atomic number change in the matrix. The X-ray absorption factor (A) refers to the decrease in the density of characteristic X-rays from emitting location to the detector. F represents the florescence factor, which arises from the excitation of characteristic X-rays of the element to be analyzed by the characteristic X-rays emitted from matrix atom. This happens when the characteristic X-rays of the matrix atom have greater energy than required to excite the characteristic X-rays of element to be analyzed.

The ZAF method outlined above is suitable for heavy and medium weight elements and it relies extensively on computing tools where the software considers all the possible errors

occurring during EDX analysis. However, the Copper to cobalt EDX ratio in our work was determined without the use of standards. Hence, EDX measurement may generate potentially large errors of the order of 17% since our samples are highly porous and potentially inhomogeneous [A1, A2].

Homogeneity of the material is an important factor to be considered during the error analysis of EDX measurement. In order to estimate the error in the homogeneity of the material, the EDX analysis was carried out at different spots of the same sample. The error generated during the preparation of the solution is another factor that contributes to the error in the EDX measurement. To evaluate the magnitude of the error on the copper to cobalt ratio used in this thesis to characterize the composition of our materials, we evaluated first the error on the EDX measurements and then second the error associated with the preparation of the solutions used in sample preparation. This will allow us to understand the source of error and to discuss our results in the context of their accuracy and precision.

A1.1.1 EDX error analysis for the thermal decomposition method

To evaluate the realistic error for the Cu to Co ratio for samples prepared using the thermal decomposition method, the EDX signal was acquired from five different spots on the samples. The example below is for a $CuCo_2O_4$, i.e. x = 1.

Table A1: The EDX measurement at different spots of a $CuCo_2O_4$ electrode prepared by thermal decomposition method.

Element detected and Cu/Co ratio	Spot 1	Spot 2	Spot 3	Spot 4	Spot 5	Average and standard deviation* (Counts)	Average and standard deviation (Counts)	Relative error **%**
Copper	9.12	8.12	7.70	7.61	9.21	8.3$\underline{5}$2 ± 0.6$\underline{8}$6	8.4 ± 0.7	8
Cobalt	15.54	13.89	15.24	15.24	17.82	15.5$\underline{5}$ ± 1.2$\underline{7}$3	15.6 ± 1.3	6
Cu/Co						0.53$\underline{8}$ ± 0.08$\underline{8}$0	0.54 ± 0.09	17

*Averages and standard deviations used for calculations, i.e., before rounding up. The lines under the numbers refer to the position of the significant figure.

The data from EDX measurements have two decimal places. The average and standard deviation were calculated and are given in Table A1 before and after rounding up. The relative error for the Cu/Co ratio is 17%, which is very close to the value of 15% quote in the literature for EDX analysis performed on porous samples without the use of internal standards [A2].

The error in the copper-cobalt ratio was calculated using following equation

$$\Delta(Cu/Co) = (\Delta Cu/Cu + \Delta Co/Co) * Cu/Co \quad (A.2)$$

where ΔCu is obtained by standard deviation of amount of copper and ΔCo is obtained by standard deviation of amount of cobalt.

The standard deviation, $$\sigma = \sqrt{\sum (x_i - \mu)^2 / N} \quad (A.3)$$

Where x_i represents the individual measurements and μ the mean of infinite number of measurements. N is the number of measurements.

Calculation is shown below:

$\Delta Cu = \sqrt{[(9.120 - 8.352)^2 + (8.120 - 8.352)^2 + (7.700 - 8.352)^2 + (7.610 - 8.352)^2 + (9.210 - 8.352)^2]}$

$= \sqrt{(0.589 + 0.054 + 0.425 + 0.550 + 0.736)/5} = \sqrt{2.354/5} = \sqrt{0.471} = 0.686$

$\Delta Co = \sqrt{[(15.54 - 15.55)^2 + (13.89 - 15.55)^2 + (15.24 - 15.55)^2 + (15.24 - 15.55)^2 + (17.82 - 5.55)^2]}$

$= \sqrt{[(0.0001 + 2.7555 + 0.0961 + 0.0961 + 5.1529)/5]} = \sqrt{(8.1007/5)} = \sqrt{1.6201}$

$= 1.2728 = 1.273$

$\Delta(Cu/Co) = (\Delta Cu/Cu + \Delta Co/Co) * Cu/Co$

$= (0.686/8.352 + 1.273/ 15.550) * 8.352/15.550$

$= (0.0821 + 0.0819) * 0.5371 = 0.0880 = 0.09$

Relative error = (0.09/0.54) * 100= 17%

A.1.2 EDX error analysis for the co-precipitation method

Similarly, the EDX measurements for co-precipitation method are summarized in Table A2. The average, standard deviation and relative error were calculated. Co-precipitation method possesses a relative error of 17%. This value is equal to the value determined for samples prepared using the thermal decomposition method showing that inhomogeneity and/or porosity effects are similar in both types of samples.

Table A2: The EDX measurement at different spots of a $Cu_{0.5}Co_{2.5}O_4$ electrode prepared by co-precipitation method.

spot	1	2	3	average	Average and standard deviation*	Average and standard deviation	Relative error **%**
Copper	4.93	5.82	4.77	5.173	5.1$\underline{7}$3 ± 0.4$\underline{6}$2	5.2 ± 0.5	10
Cobalt	22.53	23.66	20.44	22.21	22.21 ± 1.3$\underline{3}$	22.2 ± 1.3	5
Cu/Co				0.233	0.23$\underline{3}$ ± 0.03$\underline{5}$	0.23 ± 0.04	17

*Averages and standard deviations used for calculations, i.e., before rounding up. The lines under the numbers refer to the position of the significant figure.

The error in the Cu/Co ratio was calculated using equation A2 as outlined below:

$\Delta Cu = \sqrt{[(4.930 - 5.173)^2 + (5.820 - 5.173)^2 + (4.770 - 5.173)^2]}$

$= \sqrt{(0.059 + 0.419 + 0.162)/3} = \sqrt{0.640/3} = \sqrt{0.2133} = 0.462$

$\Delta Co = \sqrt{[(22.53 - 22.21)^2 + (23.66 - 22.21)^2 + (20.44 - 22.21)^2}$

$= \sqrt{[(0.1024 + 2.1025 + 3.1329)/3]} = \sqrt{5.3378/3} = \sqrt{1.7793} = 1.3339 = 1.33$

$\Delta(Cu/Co) = (\Delta Cu/Cu + \Delta Co/Co) * Cu/Co$

$= (0.462/5.173 + 1.33/ 22.210) * 5.173/22.210$

$= (0.0893 + 0.0599) * 0.2329 = 0.035$

Relative error = (0.04/0.23) * 100= 17%

A.2. Error in the concentration of the solution used for the preparation of $Cu_xCo_{3-x}O_4$ films

It is very important to consider the error in the concentration of the solution used for the preparation of $Cu_xCo_{3-x}O_4$ films as it affects the final composition

A.2.1. Errors associated with the solution prepared for the co-precipitation method

Table A3: The error associated with stock solutions used for the co-precipitation method

solution	Mass (g)	Error (g)	Volume (mL)	Error (mL)	Molarity (M)	ΔM (M)	ΔM.W (g/mol)
$CuSO_4$	6.2421	±0.0001	25.00	±0.03	1.000	±0.001	±0.009
CoSO4	7.0275	±0.0001	25.00	±0.03	1.000	±0.001	±0.006

Error associated with 25.00 ml volumetric flask is ± 0.03ml.

Molarity of $CuSO_4$ (M_{Cu}) = (mass/M.W)/Volume

Molarity of $CuSO_4$ (M_{Cu}) = 6.2421 g/ 249.6850 g/mol *(1/0.02500 L) = 0.999<u>9</u>96

Molarity of $CoSO_4$ (M_{Co}) = 7.0275 g/ 281.1000 g/mol *(1/0.02500 L) = 1.00<u>0</u>0M

$$\Delta M = (\Delta m/m + \Delta M.W/M.W + \Delta V/V)*M \quad (A.4)$$

where Δm is the error in the mass, ΔM.W. is error in the molecular mass and ΔV the error in the volume of solution.

The error in the concentration of $CuSO_4$ stock solution (ΔM_{Cu})

ΔM_{Cu} = (0.0001g/6.2420g + 0.009g mol^{-1}/249.685 g mol^{-1} + 0.03 mL/25.00 mL) * 0.999<u>9</u>96M

ΔM_{Cu} = (0.00002 + 0.00004 + 0.00120)* 0.99<u>9</u>996M = 0.00<u>1</u>26M = 0.001M

The error in the concentration of $CuSO_4$ stock solution (ΔM_{Co})

ΔM_{Co} = (0.0001g/7.0275g + 0.006 g mol^{-1}/ 281.103 g mol^{-1} + 0.03 mL/25.00 mL) * 1.00<u>0</u>M

ΔM_{Co} = (0.00001 + 0.00002 + 0.00120) * 1.000M = 0.00<u>1</u>23M = 0.001M

If the uncertainties are independent of each other, the uncertainty in the sum or difference in each number is obtained by equation A6:

$\Delta z^2 = \Delta x^2 + \Delta y^2$ (A5)

$\Delta z = \sqrt{(\Delta x^2 + \Delta y^2)}$ (A6)

Error in the concentration of the final solution:

$\Delta M = \sqrt{[(\Delta M_{cu}/ M_{cu})^2 + (\Delta M_{Co}/M_{co})^2]} * M$ (A7)

Concentration of $CuSO_4$ stock solution = 1.000M

Error in concentration of $CuSO_4$ stock solution = 0.001M

Concentration of $CoSO_4$ stock solution = 1.000M

Error in concentration of $CoSO_4$ stock solution = 0.001M

The error in the concentration of stock solution (ΔM)

$= \sqrt{[(0.001/1.000)^2 + (0.001/1.000)^2]} * 1.000 = 0.001\underline{4} = 0.001$

Table A4: The error associated with the final solution used for co-precipitation method

Composition	Volume of $CuSO_4$ (mL)	Volume of $CoSO_4$ (mL)	Number of moles of Cu (mol)	Number moles of Co (mol)	Cu/Co ratio and it's standard deviation	Relative error (%)
Co_3O_4	0*	9.00 ± 0.02	0*	0.00900± 0.00002	-	-
$Cu_{0.25}Co_{2.75}O_4$	0.75 ± 0.01	8.25 ± 0.03	0.00075 ± 0.00001	0.00825 ± 0.00003	0.0909 ± 0.0015	1.7
$Cu_{0.5}Co_{2.5}O_4$	1.50 ± 0.01	7.50 ± 0.02	0.00150± 0.00001	0.00750 ± 0.00002	0.2000 ± 0.0019	0.9
$Cu_{0.75}Co_{2.25}O_4$	2.25 ± 0.02	6.75 ± 0.03	0.00225 ± 0.00002	0.00675 ± 0.00003	0.3333 ± 0.0044	1.3
$CuCo_2O_4$	3.00 ± 0.01	6.00 ± 0.02	0.00300 ± 0.00001	0.00600 ± 0.00002	0.5000 ± 0.0033	0.7

* Exact value since no copper was introduce in the solution.

The error calculation for $Cu_{0.25}Co_{2.75}O_4$, prepared by co-precipitation method is shown below.

0.75 ml of $CuSO_4$ was transferred using a 1ml syringe and the error associated with 1 ml syringe is ± 0.01 ml. 8.25 ml of $CoSO_4$ was transferred using a 10 ml pipette and 1 ml syringe. The error associated with 10ml pipette is ±0.02ml and that of 1 ml syringe is ± 0.01ml. Hence the total error is ± 0.03ml.

Number of moles = Molarity* Litre of solution

Number of moles of Cu (Cu_{mol}) = 1.00000M * 0.00075L = 0.00075 mol

Error in the number of moles of Cu (ΔCu_{mol}) = 1.00000M * 0.00001 L = 0.00001 mol

Number of moles of Co (Co_{mol}) = 1.00000M * 0.00825 L = 0.00825 mol

Error in the number of moles of Co (ΔCo_{mol}) = 1.00000M * 0.00003 = 0.00003 mol

The error in the copper-cobalt ratio, $\Delta(Cu/Co) = (\Delta Cu/Cu + \Delta Co/Co) * Cu/Co$

= (0.00001/0.00075 + 0.00003/ 0.00825) * 0.09091

= (0.01333+ 0.00364) * 0.09091 = 0.00154 = 0.0015

Relative error = (0.00154/0.09091)*100 = 1.69% = 1.7%

A.2.2 Errors associated with the solution prepared for the thermal decomposition method

Table A5: The error associated with stock solution, used for Thermal decomposition method

solution	Mass (g)	Error (g)	Volume (mL)	Error (mL)	Concentration (M)	ΔM (M)	ΔM.W (g/mol)
$Cu(NO_3)_2$	1.2080g	±0.0001	10.00	±0.03	0.500	0.001	0.005
$Co(NO_3)_2$	3.6379	±0.0001	25.00	±0.02	0.500	0.001	0.007

Error associated with 25.00 mL volumetric flask is ± 0.03 mL.

Error associated with 10.00 mL volumetric flask is ± 0.02 mL.

Molarity of $Cu(NO_3)_2$ solution (M_{Cu}) = (mass/M.W)/Volume

= 1.2080 g/ 241.6000 g/mol *(1/0.01000 L) = 0.5000M

Molarity of $Co(NO_3)_2$ (M_{Co}) = 3.6379 g/ 291.0341 g/mol *(1/0.02500 L) = 0.5000M

The error in the molarity of stock solution (ΔM):

$\Delta M = (\Delta m/m + \Delta M.W/M.W + \Delta V/V)*M$

The error in the molarity of $Co(NO_3)_2$ stock solution (ΔM_{Co})

= (0.0001g/3.6379g + 0.0051 g mol^{-1}/291.0341 g mol^{-1} + 0.03 mL/25.00 mL) * 0.5000M

= (0.00003 + 0.00001 + 0.00120) * 0.5000M = 0.00124M = 0.001M

The error in the molarity of $Cu(NO_3)_2$ stock solution (ΔM_{Cu})

= (0.0001g/1.2080g + 0.0069 g mol^{-1}/241.6000 g mol^{-1} + 0.02 mL/10.00 mL) * 0.5000M

= (0.00008 + 0.00003 + 0.00200) * 0.5000M = 0.00105M = 0.001M

If the uncertainties are independent of each other, the uncertainty in the sum or difference in each number is obtained by the equation:

$\Delta z = \sqrt{(\Delta x^2 + \Delta y^2)}$

The total error in the molarity of solution:

$\Delta M = \sqrt{[(\Delta M_{cu}/ M_{cu})^2 + (\Delta M_{Co}/M_{co})^2]} * M$

Molarity of stock solution of $Cu(NO_3)_2$ = 0.500M

Error in molarity of stock solution of $Cu(NO_3)_2$ = 0.001M

Molarity of stock solution of $Co(NO_3)_2$ = 0.500M

Error in concentration of stock solution of $Co(NO_3)_2$ = 0.001M

The total error in the concentration of stock solutions (ΔM)

$= \sqrt{[(0.001/0.500)^2 + (0.001/0.500)^2]} * 0.500 = 0.0015 \approx 0.002$

Table A6: The error associated with the final solution used for thermal decomposition method

composition	Volume of $CuSO_4$ (ml)	Volume of $CoSO_4$ (ml)	Number of moles of Cu	Number moles of Co	Cu/Co ratio and it's standard deviation	Relative error (%)
Co_3O_4	0*	3.00 ± 0.03	0*	0.001500 ±0.000015	-	-
$Cu_{0.25}Co_{2.75}O_4$	0.25 ± 0.01	2.75 ± 0.03	0.000125 ± 0.000005	0.001375 ± 0.000015	0.0909 ± 0.0046	5.1
$Cu_{0.5}Co_{2.5}O_4$	0.50 ± 0.01	2.50 ± 0.03	0.000250 ± 0.000005	0.001250 ± 0.000015	0.2000 ± 0.0064	3.2
$Cu_{0.75}Co_{2.25}O_4$	0.75 ± 0.01	2.25 ± 0.03	0.000375 ± 0.000005	0.001125 ± 0.000015	0.3333 ± 0.0089	2.7
$CuCo_2O_4$	1.00 ± 0.01	2.00 ± 0.02	0.000500 ± 0.000005	0.001000 ± 0.000015	0.5000 ± 0.0125	2.5

* Exact value since no copper was introduced in the solution.

The error calculation for $Cu_{0.25}Co_{2.75}O_4$, prepared by thermal decomposition method is shown below.

0.25 ml of $Cu(NO_3)_2$ and 2.75 ml of $Co(NO_3)_2$ were transferred using a 1ml syringe. The error associated with 1 ml syringe is ± 0.01 ml

Number of moles of Cu (Cu_{mol}) = 0.500000M * 0.000250L = 0.000125mol

Error in the number of moles of Cu (ΔCu_{mol}) = 0.500000M * 0.000010 L = 0.000005 mol

Number of moles of Co (Co_{mol}) = 0.500000M * 0.002250 L = 0.001375 mol

Error in the number of moles of Co (ΔCo_{mol}) = 0.500000M * 0.000030 = 0.000015 mol

The error associated with final solution of $Cu_{0.25}Co_{2.75}O_4$, Δ(Cu/Co)

= (0.000005/0.000125 + 0.000015/ 0.001375) * 0.090909

= (0.040000+ 0.010909) * 0.090909 = 0.004628 = 0.0046

Relative error = (0.004628/0.090909)*100 = 5.09% = 5.1%

A.3. X-ray diffraction error analysis

The profile fitting of the X-ray diffraction data of sample allowed us to measure the percentage of CuO and calculate the standard deviation, is shown in the Table A7.

Table A7: The error in the percentage of CuO present in the samples, prepared by co-precipitation method and thermal decomposition method.

Co-precipitation method($Cu_{0.5}Co_{2.5}O_4$)			Thermal decomposition method($CuCo_2O_4$)		
Profile fitting (x_i)	Amount of CuO (%)	$\Delta x = \lvert x_i - \mu \rvert$ (%)	Profile fitting (x_i)	Amount of CuO (%)	$\Delta x = \lvert x_i - \mu \rvert$ (%)
x_1	3.58	0.79	x_1	10.17	0.40
x_2	3.09	0.30	x_2	8.94	0.83
x_3	1.70	1.09	x_3	10.20	0.43
Average (μ)	2.79		Average	9.77	
Standard deviation ($\sigma = \sum \Delta x/3$)		0.73	Standard deviation ($\sigma = \sum \Delta x/3$)		0.55
Final value	2.8	0.7	Final value	9.8	0.6

A.4. Roughness factor - error calculation

The roughness factor of the sample was calculated as the ratio of double layer capacitance of the sample and double layer capacitance of a smooth electrode. For double layer capacitance measurements, the scan rate was plotted against current density at the middle of the narrow potential range. Both anodic and cathodic currents were plotted against scan rate and the average of cathodic and anodic slopes was calculated. From this value the roughness factor was then calculated. Error calculation for Co_3O_4 is shown below.

Anodic slope = 0.0097 ± 0.0011 F cm^{-2}

Cathodic slope = 0.0121 ± 0.0025 F cm^{-2}

Average of slope = $(0.0097 + 0.0121)/2 = 0.0109 \pm 0.0018$ F cm^{-2}

The standard deviation, $\sigma = \sum \Delta x/N$ (A8)

Where, $\Delta x = |x_i - \mu|$

x_i represents the individual measurements and μ the average of measurements. N is the number of measurements.

Standard deviation , $\sigma = (0.0097 - 0.0109) + (0.0121 - 0.0109)]/2 = 0.0012$

Roughness factor = $C_{dl} / C_{dl\ (smooth)}$ (A9)

Where C_{dl} represents the double layer capacitance of the sample and $C_{dl(smooth,)}$ the double layer capacitance of smooth surface. The double layer capacitance of a smooth surface is assumed to be 60 µF cm^{-2}.

Roughness factor = 0.010900 F cm^{-2}/ 0.000060 F cm^{-2} = 182

Error in the roughness factor (ΔR_f) = R_f (ΔSlope / slope + Δ C_{dl} smooth surface / C_{dl} smooth surface)

= 182 (0.0012/0.0191 + 3* 10^{-6}/ 60*10^{-6}) = 30

Relative error = Relative error = (Δx / x) * 100

= (30/182) * 100 = 17%

A.5. Calibration of potentiostat

In this work we have used an aqueous electrode (calomel electrode) as a reference for the electrochemical experiments and hence the calibration of the potentiostat using ferrocene would generate a liquid junction potential that makes this approach unsuitable. Hence the calibration of potentiostat was carried out using impedance measurements. In order to verify the accuracy of the potentiostat, the measurements were done using the reference circuit box obtained with the device (RCB200, Radiometer, Copenhagen), as shown in the Figure A1**.** Using the same program the impedance of two reference circuits was measured. In the first circuit the working electrode was connected to a one capacitor-circuit (circuit C) and in the second one, it was connected to a circuit containing two capacitors (circuit D) (see Fig. A1). The data showed clear and consistent Nyquist plots, displaying one and two semi-circles for circuits C and D, respectively. The impedance fitting program yielded excellent result as given in Table A8 confirming that the potentiostat is well calibrated.

Table A8**:** Resistance and capacitance values measured by the potentiostat compared to the theoretical values given for the electric circuit.

Circuit elements	Measured values	Theoretical values	Uncertainty
C-R1	1.187 kΩ	1.21 kΩ	1%
C-R2	4.972 kΩ	4.99 kΩ	1%
C-C1	4.697 nF	4.7 nF	10%
D-R1	1.186 kΩ	1.21 kΩ	1%
D-R2	4.974 kΩ	4.99 kΩ	1%
D-C1	4.691 nF	4.7 nF	10%
D-R3	9.947 kΩ	10 kΩ	1%
D-C2	0.959 µF	1 µF	10%

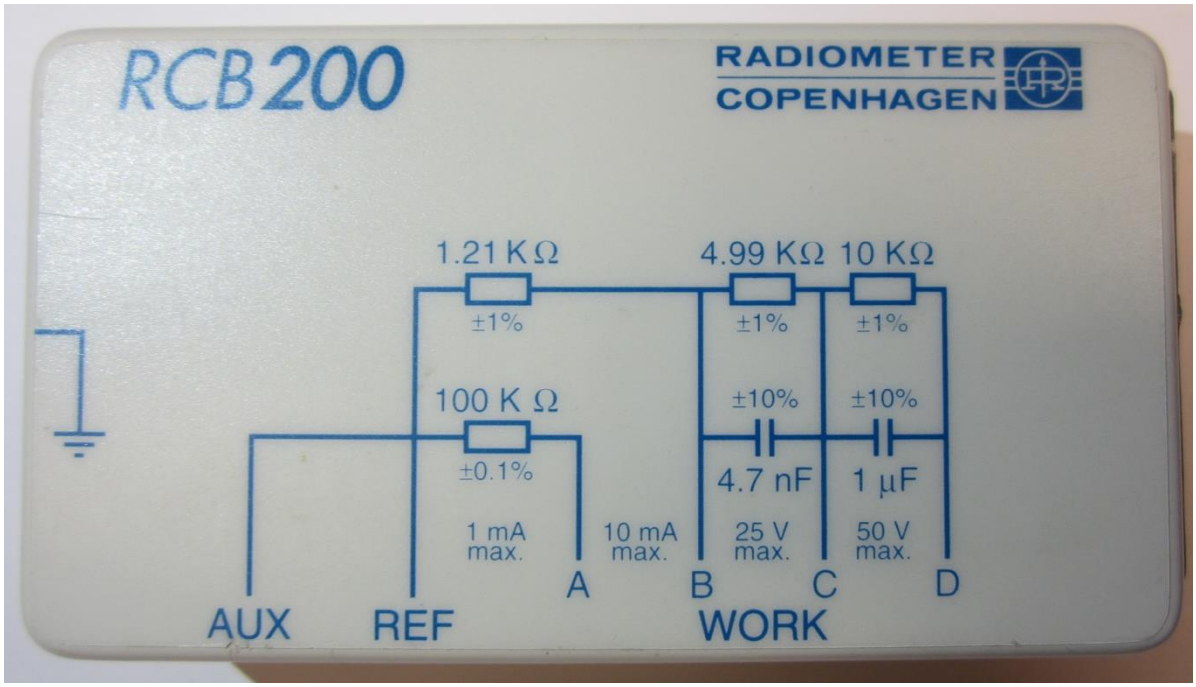

Figure A1: Reference circuit box used to calibrate the potentiostat. Auxiliary and reference electrodes were plugged at the AUX and REF ends and the work electrode was plugged at the C terminal (one capacitor-circuit) and then at the D terminal (2 capacitors-circuit)

a.

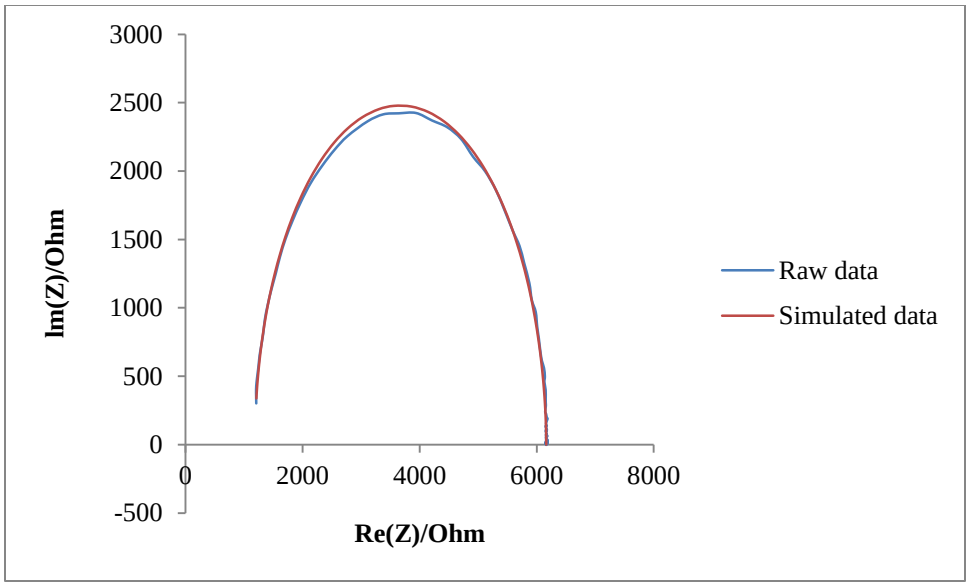

b.

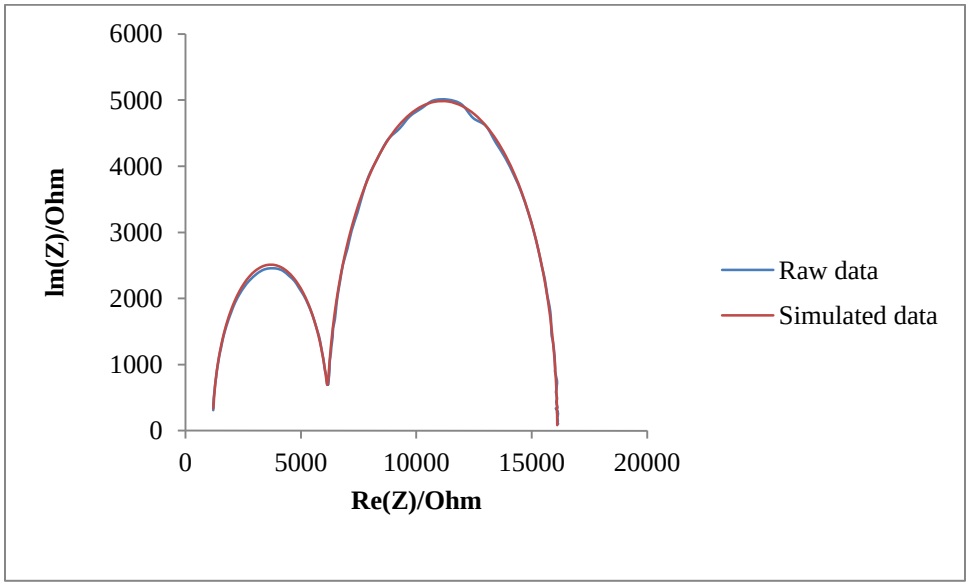

Figure A2: Nyquist plots of reference circuit with (a) one capacitor and (b) two capacitors.

References

A1. Goldstein, J. I; Newbury, D. E; Joy, D. C; Lyman, C. E; Echlin, P.; Lifshin, E.; Sawyer, L.; Michael, J. R; *Scanning electron microscopy and X-ray microanalysis, 3rd ed.*; Kluwer Academic/Plenum Publishers: New York, 2003.

A2. Leng, Y.; *Materials characterization: Introduction to microscopic and spectroscopic methods*; John Wiley & Sons: Asia, 2008

A3. Christian G. D.; *Analytical Chemistry, 5th ed.*; John Wiley & Sons: New York, 1994.

A4. Marsan, B.; Fradette, N.; Beaudoin, G., J. *Electrochem. Soc.* **1992**, 139, 1889.